CHALMERS
UNIVERSITY OF TECHNOLOGY

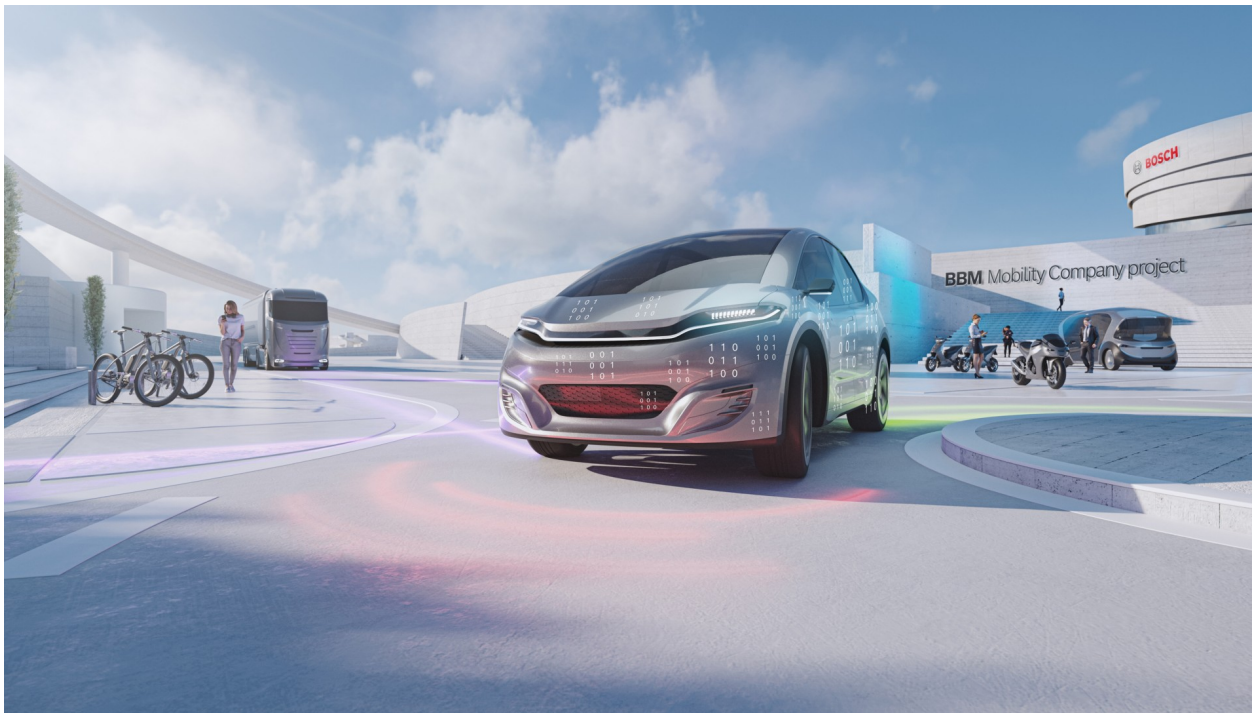

Identification of Uncertainties and Disturbances for Safe Autonomous Driving Control

Using Polynomial Chaos Expansion

Master's thesis in Systems, Control and Mechatronics

RANBIR SINGH

DEPARTMENT OF ELECTRICAL ENGINEERING

CHALMERS UNIVERSITY OF TECHNOLOGY
Gothenburg, Sweden 2023
www.chalmers.se

Master's thesis 2023

Identification of Uncertainties and Disturbances for Safe Autonomous Driving Control

Using Polynomial Chaos Expansion

RANBIR SINGH

CHALMERS
UNIVERSITY OF TECHNOLOGY

Department of Electrical Engineering
Division of Systems and Control
Chalmers University of Technology
Gothenburg, Sweden 2023

Identification of Uncertainties and Disturbances for Safe Autonmous Driving Control Using Polynomial Chaos Expansion
RANBIR SINGH

Supervisors:
Dr.-Ing. Kevin Schmidt, Robert Bosch GmbH (CR/ADI1.2)
Dr.-Ing. Felix Berkel, Robert Bosch GmbH (CR/ADX2.2)
Dr.-Ing. Steffen Joos, Robert Bosch GmbH (XC-DX/EYM1)
Max May, M.Sc., Institut für Systemdynamik, Universität Stuttgart

Examiner:
Nikolce Murgovski, Electrical Engineering, Chalmers University of Technology

Master's Thesis 2023
Department of Electrical Engineering
Division of Systems and Control
Chalmers University of Technology
SE-412 96 Gothenburg
Telephone +46 31 772 1000

Cover: Render of a futuristic car driving. ©Robert Bosch GmbH

Typeset in LaTeX
Printed by Chalmers Reproservice
Gothenburg, Sweden 2023

Identification of Uncertainties and Disturbances
for Safe Autonomous Driving Control
Using Polynomial Chaos Expansion
RANBIR SINGH
Department of Electical Engineering
Chalmers University of Technology

Abstract

Parameter values of mathematical models of systems are often considered as being constant. In reality, the modelled values are likely to vary depending on several factors such as environmental conditions and production variances being two examples. Within the scope of this project, a car was considered with four uncertainties, these being the frictional coefficient between tyre and road, the load carried by the vehicle, the position of its centre of gravity, and a time variant side wind force.

The focus of this project was to investigate the possibility of estimating the probability distributions of parametric uncertainties based on measured data. Additionally, given that mathematical models are often simplifications of reality, the propagation of modelling errors into the estimates was investigated. This was achieved by identifying a linear single track model based on data generated in simulation using either a linear single track model or a non-linear single track model.

Data sets were created with differing levels of noise in the measured signals. Each data set was generated by simulating 2000 random realisations of the vehicle and then computing the mean and variance of the output trajectories. System identification methods were used to identify a linear single track model expanded by polynomial chaos expansion such that its resulting mean and variance would match that of the data.

From the testing, it was shown that the method used delivered consistent estimates for initial guesses with deviations between 0% to 45%, above which the estimates lost accuracy. Using the simulation data from the linear model as a base for identification allowed the estimated probability distribution to be close to the correct distributions. When using the simulation data from the non-linear model as a base for identification, an error was introduced into the estimate. This error was however consistent across different estimation runs and can be interpreted as a linearisation error.

Keywords: stochastic control, polynomial chaos, automated driving, safe-by-design, inverse uncertainty quantification, parameteric uncertainty

Acknowledgements

Als erstes muss ich mich bei meinen Betreuern Dr. Kevin Schmidt, Dr. Felix Berkel, Dr. Steffen Joos, alle bei der Robert Bosch GmbH, und Max May beim Institut für Systemdynmaik an der Universität Stuttgart, bedanken. Die Unterstützung und Hilfsbereitschaft von allen habe ich sehr geschätzt. Der Austausch mit ihnen war immer sehr bereichernd und lehrreich.

I would also like to express my gratitude to all of my family and friends in both Sweden and Germany, as well as to the weights in the gym, for helping me keep my sanity even when (my own) MATLAB code tried its very best to rob me of it. A special mention here goes to the Coffee Breaks student group at Bosch. It has been a pleasure to get to know all of you! Thank you for the unforgettable memories and thank you to Annabelle for all of the cake! :D

Lastly, with the end of this thesis comes the end of my stint here in Germany where I have had some of the most enjoyable time of my life. Therefore, I must say danke Deutschland! Wir sehen uns auf jeden Fall wieder. Versprochen!

Ranbir Singh, Renningen, January 2023

List of Acronyms

Below is the list of acronyms that have been used throughout this thesis listed in alphabetical order:

ADAS	Advanced Driver Assistance System
ADS	Automated Driving System
CoG	Centre of Gravity
GLQ	Gauss-Legendre Quadrature
gPC	genralised Polynomial Chaos
KLD	Kullback-Leibler Divergence
KLE	Karhunen-Loéve Expansion
LST	Linear Single Track
LTI	Linear Time Invariant
LQR	Least Quadratic Regulator
NLST	Non Linear Single Track
ORC	Observability Rank Condition
PC	Polynomial Chaos
PCE	Polynomial Chaos Expansion

SGI	Structurally Globally Identifiable
SLI	Structurally Locally Identifiable
SLQR	Stochastic Least Quadratic Regulator
STM	Single Track Model
TPO	Total Polynomial Order

Nomenclature

Below is the nomenclature of indices, parameters, and variables that have been used throughout this thesis.

Indices

max	Maximum of variable
min	Minimum of variable
f	Pertaining to front tyre/axle
r	Pertaining to rear tyre/axle
PCE	Pertaining to polynomial chaos expansion or a system expanded by polynomial chaos expansion
KLE	Pertaining to Karhunen-Loève expansion
GLQ	Pertaining to Gauss-Legendre quadrature

Parameters

μ	Frictional coefficient between road and tyre
m_{load}	Mass of the load carried by the vehicle
l_{f}	Distance from centre of gravity to front axle
l_{r}	Distance from centre of gravity to rear axle
F_{w}	Side wind strength
$\bar{F}_{\text{w}}$	Mean of side wind strength
$F_{\text{w},\sigma}$	Standard deviation of wind strength
$F_{\text{w},\alpha}$	Time variant component of wind strength
M_{w}	Yaw moment induced by side wind
v_c	Constant speed of the vehicle
m	Total mass of the vehicle

g	Acceleration due to gravity
L	Distance between front and rear axles
J_0	Specific moment of intertia of the vehicle
I_z	Moment of inertia of vehicle
$\underline{A}$	System Matrix
$\underline{B}$	Input Matrix
$\underline{W}$	Disturbance Matrix
$\boldsymbol{x}_0$	Initial state
A	Noise intensity
w	Single weighting parameter
$\boldsymbol{w}$	Vector of weighting parameters
N_{GLQ}	Quadrature order of Gauss Legendre quadrature
N_{PCE}	Highest polynomial order in a polynomial chaos expansion approximation
p_c	Truncation parameter for approximating a Karhunen-Loève expansion
$\underline{Q}$	State weighting matrix
$\underline{R}$	Input weighting matrix
$\underline{K}$	Gain matrix
T	Final time
T_c	Time constant of covariance function
M_c	Yaw moment factor

Variables

t	Time
β	Vehicle slip angle
$\dot{\beta}$	Vehicle slip rate
α_i	Slip angle of tyre i
$F_{i,z}$	Normal force on the front tyre
$F_{i,z}$	Normal force on tyre i
$F_{i,y}$	Lateral force on tyre i
$F_{i,x}$	Longitudinal force on tyre i
c_i	Cornering stiffness of tyre i
c_{Si}	Nominal cornering stiffness of tyre i

ψ	Yaw angle
$\dot{\psi}$	Yaw rate
$\ddot{\psi}$	Yaw acceleration
δ	Steering angle
ξ	Single random variable
$\boldsymbol{\xi}$	Vector of random variables
$\boldsymbol{x}$	State vector
$\boldsymbol{u}$	Input signal
$\boldsymbol{X}$	PC expanded state vector
$\boldsymbol{U}$	PC expanded input signal
θ	Single unknown parameter
$\boldsymbol{\theta}$	Vector of unknown parameters

Contents

List of Figures

List of Tables

1

Introduction

When designing automated systems, engineers face the challenge of modelling reality in order to design control algorithms according to the input-output relationships of the dynamic systems in question. For this purpose, mathematical models of reality are usually created, but in order for these to remain manageable in complexity, they often have to be simplified to some degree. Often, the dynamics of a system will be simplified and parameter values will be modelled as constant and unchanging in the model, which is rarely reflected in the real world. This poses a challenge when developing control systems, particularly those which are safety critical. The nominal system models, upon which a control law will be based, rarely share the same parameter values as the real systems in which the controller is eventually implemented, yet safe and reliable operation must be ensured.

This problem is no less prevalent in the automotive field, where advanced driver assistance systems (ADASs) and automated driving systems (ADSs) are becoming more and more complex in the hunt for a competitive advantage. When developing such features, engineers must satisfy a range of safety criteria imposed both by legislative and regulatory bodies such as [1]–[3], but also by the public, who must be convinced that autonomous cars and automated driving features are safe and reliable enough. Liability in the case of an accident is another incentive to avoid as many accidents as possible in the first case [4].

In order for companies to be able to guarantee "safety of the intended functionality" [2], the need for accurate models increases. Even if engineers have to make certain assumptions and estimations about the road conditions and vehicle parameters, it is important that their systems work well in the real world where the tarmac could be both dry and clean or wet and covered in gravel. In real life, the exact friction between the road and tyre may differ from the assumed value due to varying surfaces or the presence of debris or fluid on the road. Similarly, the mass of the vehicle could differ significantly as one single occupant travelling without luggage may add about 70 kg of mass, where as a couple bringing all their belongings with them as they move to a new city or a family of four going on vacation could change the vehicle's total mass more dramatically.

Although the values of certain parameters may be uncertain, these uncertainties themselves may be describable in terms of the likelihood of certain values occurring. This knowledge allows systems to be designed and tested with the most probable

operating conditions in mind. At Bosch, as a part of a project called SAFER, the aim is to develop a concept referred to as *Safe-by-Design*. The idea behind this concept is to account for stochastic effects in the design stage, allowing controllers to be synthesised with inherent guarantees of safety margins. This is different to the so called *Safe-by-Testing* approach, where the safety margins of controllers are only guaranteed through testing. The ultimate goal of the SAFER project is thus to create a system development model which enables faster concept-to-market times than currently used development models.

In order to use the probability distributions associated with parametric uncertainties and disturbances, it is first necessary to gather information about them. One way to go about this is to make an educated guess based on experience and reasoning about physical plausibility. Or one may try measuring them directly, by for example testing the friction between different road surfaces and tyres with some testing rig. In this thesis project, the approach of trying to extract this information from simulation data is investigated, with the target of using recorded testing data from vehicles in the future. The potential of such an approach is to continuously improve models based on large amounts of driving data gathered from vehicles operated by end-users in real world usage scenarios.

1.1 State of the Art

As mentioned at the start of this chapter, the real world is rarely entirely constant, and parameter values may change from case to case causing uncertainty regarding the exact parameter values of the real system. Potential sources of uncertainty may be production variance, environmental conditions, or other external factors. Assuming that one has some knowledge about the likelihood of different values occurring, it becomes possible to consider these parametric uncertainties in simulation and in the system model itself. There are different methods of using this information to compute the output statistics of the system. Some of the approaches are covered in this section.

A common method to get a representative image of the statistics of the output of a stochastic system is to simulate a finite number of realisations of the system. There exist different methods to picking these samples, such as the sequential Monte Carlo approach, by which these samples are picked at random [5], [6]. Other methods to pick the sampling points in a more methodical manner, for example lattice sampling, also exist [7]. In general, the more samples one is able to use, the higher the accuracy will be. The number of individual simulations needed to achieve good accuracy depends on the number of uncertainties and their character. Running such a vast number of simulations can be computationally intensive.

Another novel approach in the context of dynamic systems and control is the spectral decomposition of the random process using polynomial chaos. This approach can deliver the first and second order statistics of the output trajectories of a system, but as opposed to both sampling based methods and fuzzy models, it is not possible to get insight into individual output trajectories. The polynomial chaos expansion

(PCE) is merely an alternative representation of a stochastic system [8], [9]. The modelling effort required to use PCE is no greater than what is required to use sampling based methods, although an understanding of the mathematical background of the PCE is required in order to compute the expansion of the systems.

Fuzzy modelling is also a common approach to handling models with uncertainties in parameter values [10], [11]. There are examples in the literature of the fuzzy approach being combined with both sampling based simulation approaches and PCE [12], [13]. Similar to sampling based methods, fuzzy modelling can be used to gain insight into different output trajectories of a system with uncertainties, as well as the intervals within which the output trajectories can be expected. In a review of the usage of fuzzy models in automotive engineering, Ivanov [14] points to its usage for vehicle dynamics control systems, among other applications.

During control design, which is the ultimate goal of the SAFER project within which this project takes place, the first and second order moments of the output are of primary interest. Considering this, using PCE for modelling is an appropriate choice, as there is little interest in individual output trajectories, reducing the interest in both the sampling-based and fuzzy approaches. In addition, using PCE allows the first and second order moments to be computed orders of magnitudes faster than sampling-based methods. In [15]–[17] the PCE is compared to Monte Carlo methods, showing that the greater the desired accuracy, the greater the advantage of using the PCE. Another advantage is the relative ease with which models can be prepared for PCE.

1.2 Aim

The objective of this project was to learn how well uncertainties and time-varying disturbances of a car could be identified from simulated data by identifying a linear single track (LST) model of the car augmented through PCE. The main aspect of the identification sought to be investigated was the propagation of model errors caused by simplifications of the vehicle dynamics into the eventual probability distribution estimates.

A necessary step on the way to this objective was to conceptualise the identification work flow and to prototype it. In addition to this, it was necessary to expand Bosch' existing internal PCE-framework in order to use it to model time varying disturbances, as it was only able to model time invariant systems at the beginning of the project.

As the measured data in this project was synthesised in simulation, the modelling and implementation of vehicle models with uncertainties and disturbances was necessary.

1.3 Scope

The main constraints upon this thesis project was the number of person-hours available, as a total of 900 hours were to be spent on this project between July of 2022 and February of 2023. For the execution of the project, the tools and knowhow at Bosch' research Campus in Renningen, Baden-Württemberg, Germany were available. Among these tools was the existing SAFER-internal PCE-framework. A limitation of this was that only linear time invariant (LTI) systems could be augmented numerically, meaning it was only possible to identify linear models within this project, and also requiring an expansion to allow it to manage time varying disturbances in the model.

In this initial investigation on estimating probability distributions from measured data, measurement data was synthetically generated in a simulation environment, as opposed to real-world tests. This approach enabled perfect knowledge about- and perfect control over the conditions of the simulation, meaning no unexpected external effects or influences would affect the data. In turn, this would allow a more comprehensive analysis of the identification results and it also meant that the size of the problem could be limited to be more manageable.

In this simulation environment, the car was modelled with three uncertainties and one time-varying disturbance. The parametric uncertainties regarded the frictional coefficient μ, the mass of the vehicle load m_{load} and the position of the vehicle's centre of gravity (CoG). As a disturbance, a side wind was assumed to be present, which induced a lateral force and a yaw moment on the vehicle.

For the time invariant uncertainties and disturbances, only uniform- and normal distributions were considered, as the limitations of the PCE-framework only allowed for uniform- and normal distributed uncertainties to be described by the numeric PCE methods available at the time of the project. Time variant disturbances were considered to be coloured Gaussian processes. Gaussian processes were chosen to limit the complexity, and white noise processes where eliminated as these would require too many stochastic variables for accurate modelling using the Karhunen-Loève expansion. When looking at the system output, only the first and second order moments were calculated. As mentioned, these are the major effects considered in control design.

The vehicle model used in this project was a so-called *single track model* (STM). For identification, a linear single track (LST) model was used, whereas measured data was produced in simulation using both linear and non-linear single track (NLST) models, the specifics of which are detailed further in Chapter 2. Although the single track model is a significant simplification of a real car, it is generally sufficiently accurate as long as the vehicle is being driven well within its physical limits [18]–[20]. The usage of a single track model in turn made implementation of simulation and estimation routines easier which went towards adhering to the time constraints in place.

1.4 Report Overview

The fundamental ideas upon which the work of this thesis is built are presented in Chapter 2, which covers the basics of vehicle dynamics, Chapter 3, in which system identification is presented, and Chapter 4 where the theory behind the PCE is covered. Following these chapters, the practical usage of these ideas is covered in Chapter 5. The results of the experiments are presented and discussed in Chapter 6, which is followed by a discussion of this project's relevance in regards to future work in Chapter 7. A final conclusion is then stated in Chapter 8.

In equations and mathematical formulations, scalar values are represented by characters, either lower or upper case, for example a or A. Vectors are denoted by bold characters such as $\boldsymbol{a}$ or $\boldsymbol{A}$. Matrices are denoted by underlined capital characters such as $\underline{A}$. Note that values which would *generally* be matrices or vectors are also denoted as such, although their values in a particular application may be scalar.

2

Vehicle Dynamics

Road vehicles typically rely solely on the frictional forces between their tyres and the road surface in order to generate their motion. A driver will normally be able to provide the car with commands to change the orientation of the wheels though the steering wheel and the angular velocities of the wheels by applying a torque to them through either the brake- or throttle pedal.

The aim of this chapter is to highlight how these inputs translate into motion of the vehicle. An initial overview of tyre modelling is presented in Section 2.1, followed by an extension to show how a four-wheeled car can be modelled using a single track model in Section 2.2. The models covered in this chapter and this thesis are planar models, meaning that vertical dynamics such as roll and pitch as well the effects of undulations in the road are not considered.

2.1 The Tyre

The rubber surface of the tyre acts as the only interface between a car and the road surface under normal circumstances, and the interaction between these two surfaces creates the forces which dictate the car's motion. This road-tyre interaction is a complex phenomenon, difficult to characterise exactly. The inherent complexity becomes particularly apparent close to the tyre's traction limits [21].

To begin with, a typical tyre travelling straight with a velocity v is illustrated from the top and from the side in Figure 2.1. This tyre is rolling freely, meaning that the speed of the tyre's surface is the same as its forward speed, its angular velocity given by $\omega = \frac{v}{r}$, where r is the radius of the tyre.

If the driver applies a steering angle, the tyre will no longer be aligned with its direction of travel. The angle α between the tyre's heading and direction of travel is called the tyre's *slip angle*. If the driver applies either brakes or throttle, the tyre's angular velocity will change and thus deviate from $\frac{v}{r}$. The mismatch in the tyre's translational and rotational velocities is referred to as a *slip ratio* κ [18]. There are different definitions for the slip ratio in the literature, one such definition is

$$\kappa = \frac{\omega r - v}{v} \tag{2.1}$$

while some use the wheel speed ωr in the denominator [19], [21], [22]. A limitation

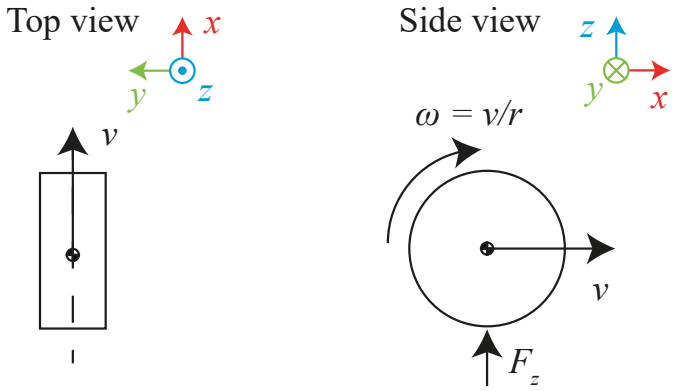

Figure 2.1: Illustration of a tyre travelling at a velocity v without steering or acceleration.

of this quantity is that is is undefined when the vehicle or tyre surface have velocity zero, depending on which definition is used, and is only valid when the vehicle or tyre is moving.

Non-zero slip angles and/or slip ratios cause forces to be developed between the tyre- and road surfaces, which is illustrated in Figure 2.2, where *pure steering* refers to the case $\alpha \neq 0$ and $\kappa = 0$ and *pure acceleration* refers to the case $\alpha = 0$ and $\kappa \neq 0$. How the magnitude of these forces relate to the magnitude of the slip angle and slip ratio is a tyre- and condition-specific characteristic. It depends on several factors such as the mechanical construction of tyre as well as the chemical compounds in the rubber, but also the road surface and normal load on the tyre [19], [21]. The so called *Magic Formula* [22] is a commonly used heuristic tyre model of the form

$$y(x, F_z) = F_z D \sin(C \arctan(Bx - E(Bx - \arctan(Bx)))), \tag{2.2a}$$
$$Y(x) = y(x) + S_V, \tag{2.2b}$$
$$x = X + S_H, \tag{2.2c}$$

where Y is either the longitudinal tyre force F_x or the lateral tyre force F_y depending on whether κ or α is used as the input X. Pacejka [22] refers to B as the stiffness factor, C as the shape factor, D as the peak value and E as the curvature factor. The parameters S_H and S_V are horizontal and vertical shifts respectively, these can be used to account for effects such as rolling resistance or ply-steer as two examples. It may be desirable to model the longitudinal and lateral forces with different parameter values for B, C, D, E S_H and S_V in the magic formula, but for the sake of simplicity, they are not differentiated here.

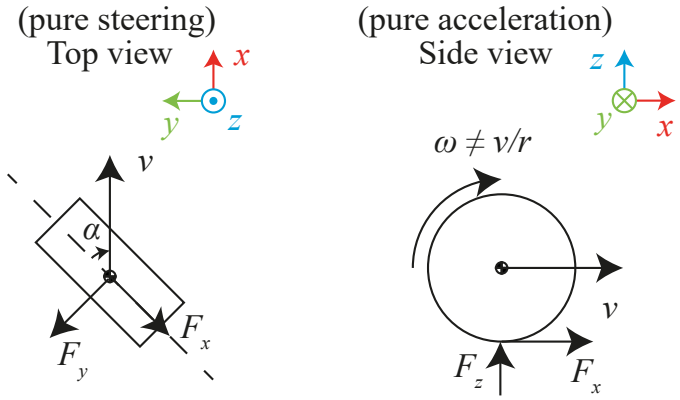

Figure 2.2: Illustration of a tyre travelling at a velocity v. Once with pure steering. Once with pure acceleration.

Example tyre curves for various road conditions are presented in Figure 2.3. The lateral and longitudinal forces are both plotted assuming pure steering and pure acceleration respectively and are based on typical tyre parameters from [23], presented in Table 2.1. The offsets $S_H = S_V = 0$. As is evident from Figure 2.3, both the longitudinal and lateral tyre forces have a linear area for small slip angles or slip ratios respectively [24] and the slope at the origin is $k = F_z BCD$ [25]. After this initial linear area, the tyre eventually reaches a peak. Increasing the slip angle or slip ratio beyond the point of this peak has no additional benefit. On the contrary, it is detrimental as the force decreases.

Table 2.1: Example tyre parameters from [23].

Surface	B	C	D	E
Dry Tarmac	10	1.9	1.00	0.97
Wet Tarmac	12	2.3	0.82	1
Snow	5	2.0	0.30	1.00
Ice	4	2.0	0.10	1.00

If the tyre is in a combined slip state, i.e. if $\alpha \neq 0$ and $\kappa \neq 0$ simultaneously, the peak tyre force in each direction will be reduced compared to the respective pure slip cases [21]. In this case, Pacejka [22] introduces scaling quantities $G_{x\alpha}$ and $G_{y\kappa}$ to account for the influence of the slip angle on the longitudinal force and the effect of the slip ratio on the lateral force respectively. Assuming $S_H = S_V = 0$, the longitudinal force is given by

$$F_x = G_{x\alpha} F_{x0}, \tag{2.3a}$$
$$G_{x\alpha} = \cos(C \arctan(B\alpha - E(B\alpha - \arctan(B\alpha)))), \tag{2.3b}$$
$$F_{x0} = F_z D \sin(C \arctan(B\kappa - E(B\kappa - \arctan(B\kappa)))), \tag{2.3c}$$

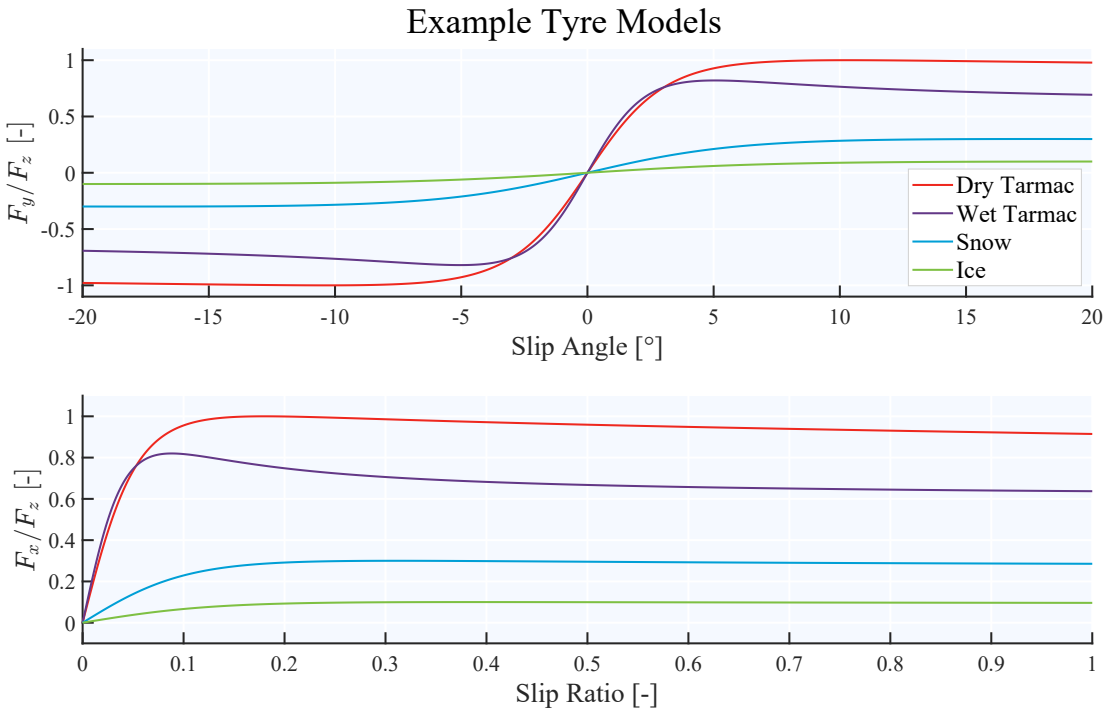

Figure 2.3: Tyre curves plotted using the tyre parameters from [23] for differing road conditions.

and the lateral force by

$$F_y = G_{y\kappa} F_{y0}, \tag{2.4a}$$
$$G_{y\kappa} = \cos(C \arctan(B\kappa - E(B\kappa - \arctan(B\kappa)))), \tag{2.4b}$$
$$F_{y0} = F_z D \sin(C \arctan(B\alpha - E(B\alpha - \arctan(B\alpha)))). \tag{2.4c}$$

Again, it may be desirable to use different values for the parameters when calculating $G_{x\alpha}$ and $G_{y\kappa}$.

The model presented here is a heuristic model and does not consider the real physical effects behind the tyre forces, and the description of the heuristic model presented here is also simplified. It is sufficient for the scope of this project, but there are many properties of the tyre and road which influence behaviour of the system. Richardson [21] investigates tyre evolution, i.e. how tyre characteristics change as they're being used in a motorsport application. Pacejka [22] dives much deeper into tyre modelling in general and presents more detailed models.

2.2 Single Track Model

A planar model of a four-wheeled car is illustrated in Figure 2.4 [18]. Here v is the speed of the vehicle, i.e. the magnitude of its velocity vector, β is the vehicle's slip angle, i.e. the angle between its heading and direction of travel. The yaw angle ψ is the angle of the vehicle relative to the x-axis in the global coordinate system and $\dot{\psi}$ is the yaw rate of the vehicle. The indices fl, fr, rl and rr correspond to the front left,

front right, rear left and rear right tyres respectively. As input, the steering angle δ is the angle between the front wheels and the vehicle's heading. Note that in real applications, cars will usually have steering geometries causing the outside and inside wheels to turn different amounts for a given angle of the steering wheel, *Ackermann steering* being an example of such a geometry [19], [26]. In favour of simplicity, the car modelled here uses a *parallel steering geometry*. Another assumption made in this modelling effort is that only the front wheels can be steered, which is the case for most road cars. However rear-wheel steering is a feature becoming increasingly common.

When the vehicle is taking a turn with a large radius, the front and rear track widths $d_{\mathrm{f,tw}}$ and $d_{\mathrm{r,tw}}$ become comparatively small and can be neglected. In automotive engineering, four-wheeled vehicles are often modelled with zero track width as a simplification [18], [19], [24]. This type of model is referred to as a *single track model*, which is illustrated in Figure 2.5, where the wheel indices have been reduced to f for front and r for rear.

If v, $\dot{v}_x$, β, $\dot{\psi}$ and δ are known, the remaining angles and vectors in Figure 2.5 can be computed. Given these values, the slip angles for each tyre can be computed as

$$\alpha_f = \delta - \tan^{-1}\left(\frac{v\sin(\beta) + l_{\mathrm{f}}\dot{\psi}}{v\cos(\beta)}\right), \tag{2.5}$$

$$\alpha_r = -\tan^{-1}\left(\frac{v\sin(\beta) - l_{\mathrm{r}}\dot{\psi}}{v\cos(\beta)}\right). \tag{2.6}$$

The weight of the vehicle is split between the front and the rear wheels such that the normal forces are

$$F_{\mathrm{f},z} = mg\frac{l_{\mathrm{r}}}{L} \underbrace{-\dot{v}_x h_{\mathrm{CoG}}}_{\text{Weight transfer}}, \tag{2.7}$$

$$F_{\mathrm{r},z} = mg\frac{l_{\mathrm{f}}}{L} \underbrace{+\dot{v}_x h_{\mathrm{CoG}}}_{\text{Weight transfer}}. \tag{2.8}$$

The latter term in both (2.7) and (2.8) concerns the weight transfer that occurs due to the longitudinal acceleration $\dot{v}_x$ and the height of the CoG h_{CoG}. The effects of lateral weight transfer are neglected with the zero track width simplification. The tyre forces can be calculated as per the description in Section 2.1.

Once the forces have been computed, it becomes possible to form the differential equations describing the motion of the vehicle [24]. The yaw acceleration can be described by

$$I_z\ddot{\psi} = l_{\mathrm{f}}(F_{\mathrm{f},x}\sin(\delta) + F_{\mathrm{f},y}\cos(\delta)) - F_{\mathrm{r},y}l_{\mathrm{r}}, \tag{2.9}$$

where I_z is the rotational inertia of the vehicle about the vertical axis passing through its CoG. By considering the vehicle's motion as per Newton's second law in its local frame (which happens to be aligned with the global frame in Figure 2.5), one arrives

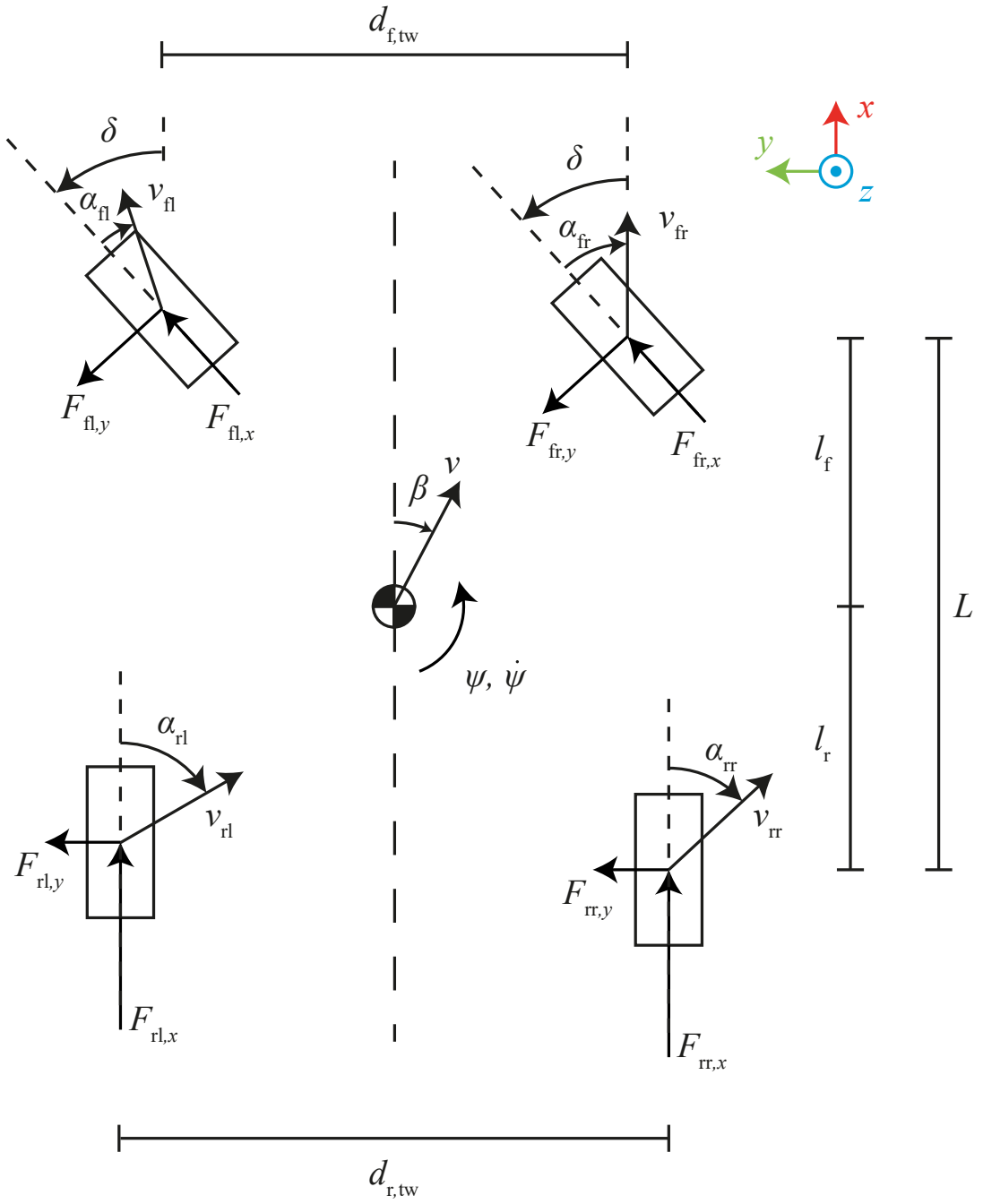

Figure 2.4: An illustration of a planar model of a four-wheeled car.

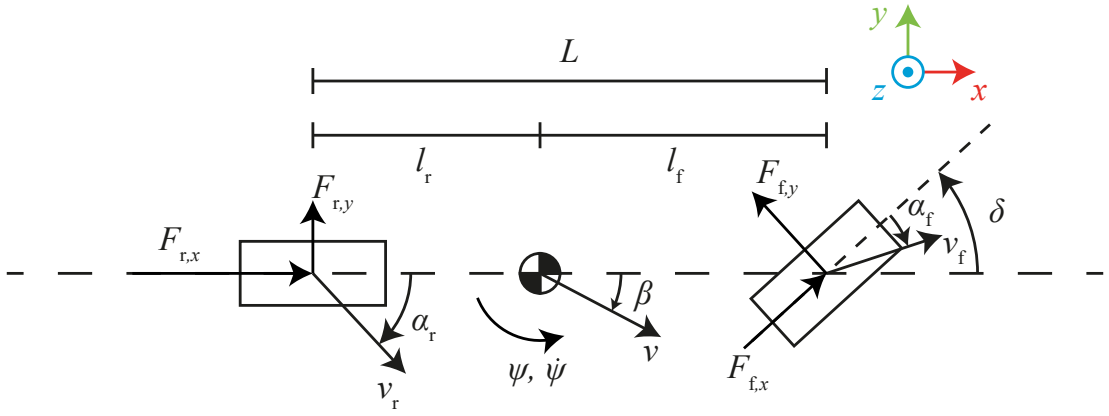

Figure 2.5: An illustration of the single track model.

at the equations

$$m(\dot{v}_x \cos(\beta) - v(\dot{\beta} + \dot{\psi}) \sin(\beta)) = F_{\mathrm{f},x} \cos(\delta) - F_{\mathrm{f},y} \sin(\delta) + F_{\mathrm{r},x}, \tag{2.10}$$

$$m(\dot{v}_x \sin(\beta) + v(\dot{\beta} + \dot{\psi}) \cos(\beta)) = F_{\mathrm{f},x} \sin(\delta) + F_{\mathrm{f},y} \cos(\delta) + F_{\mathrm{r},y}, \tag{2.11}$$

where m is the sum of the vehicle's mass m_{base} and the mass of the load m_{load}. From (2.10), it follows that

$$\dot{v} = \frac{1}{\cos(\beta)} \left(\frac{1}{m} \left(F_{\mathrm{f},x} \cos(\delta) - F_{\mathrm{f},y} \sin(\delta) + F_{\mathrm{r},x} \right) + v(\dot{\beta} + \dot{\psi}) \sin(\beta) \right), \tag{2.12}$$

which can be substituted into (2.11) to give

$$\begin{aligned} \dot{\beta} = &\frac{1}{mv} \left(F_{\mathrm{f},x} \sin(\delta) + F_{\mathrm{f},y} \cos(\delta) + F_{\mathrm{r},y} \right) \cos(\beta) \\ &- \frac{1}{mv} \left(F_{\mathrm{f},x} \cos(\delta) - F_{\mathrm{f},y} \sin(\delta) + F_{\mathrm{r},x} \right) \sin(\beta) - \dot{\psi}. \end{aligned} \tag{2.13}$$

This result together with (2.10) then gives [24]

$$\begin{aligned} \dot{v} = &\frac{1}{m} \left(F_{\mathrm{f},x} \cos(\delta) - F_{\mathrm{f},y} \sin(\delta) + F_{\mathrm{r},x} \right) \cos(\beta) \\ &+ \frac{1}{m} \left(F_{\mathrm{f},x} \sin(\delta) + F_{\mathrm{f},y} \cos(\delta) + F_{\mathrm{r},y} \right) \sin(\beta). \end{aligned} \tag{2.14}$$

With equations (2.9), (2.13), and (2.14) the dynamics can be modelled using a non-linear state space model with the state vector $\boldsymbol{x} = \begin{bmatrix} \psi & \dot{\psi} & \beta & v \end{bmatrix}^\mathsf{T}$ and the input $\boldsymbol{u} = \begin{bmatrix} \delta & \dot{v}_x \end{bmatrix}^\mathsf{T}$. The derived model contains several non-linearities however. The tyre model can be linearised by $Y(x) \approx F_z BCDx$ for small x. similarly, the small angle approximation $\cos(x) \approx 1$, $\sin(x) \approx x$ and $\tan(x) \approx x$ can be used for (2.5), (2.6), (2.9), and (2.13). Further, the model can be linearised around a certain constant operating speed $v = v_c \Rightarrow \dot{v}_x = 0$ making $v = v_c$ a system parameter rather than a

state variable. As a consequence of this, the longitudinal dynamics are neglected, meaning $F_{\mathrm{f},x} = F_{\mathrm{r},x} = 0$. These simplifications yield the slip angles

$$\alpha_{\mathrm{f}} \approx \delta - \frac{v_c\beta + l_{\mathrm{f}}\dot{\psi}}{v_c} = \delta - \left(\beta + \frac{l_{\mathrm{f}}\dot{\psi}}{v_c}\right), \tag{2.15}$$

$$\alpha_{\mathrm{r}} \approx -\frac{v_c\beta - l_{\mathrm{r}}\dot{\psi}}{v_c} = -\left(\beta - \frac{l_{\mathrm{r}}\dot{\psi}}{v_c}\right). \tag{2.16}$$

Given that the longitudinal dynamics have been neglected we have pure slip conditions, thus the vertical and lateral tyre forces are

$$F_{\mathrm{f},z} = mg\frac{l_{\mathrm{r}}}{L}, \quad F_{\mathrm{f},y} \approx \underbrace{F_{\mathrm{f},z}B_{\mathrm{f}}C_{\mathrm{f}}D_{\mathrm{f}}}_{c_{\mathrm{f}}}\alpha_{\mathrm{f}} = c_{\mathrm{f}}\alpha_{\mathrm{f}} \approx c_{\mathrm{f}}\left(\delta - \left(\beta + \frac{l_{\mathrm{f}}\dot{\psi}}{v_c}\right)\right), \tag{2.17}$$

$$F_{\mathrm{r},z} = mg\frac{l_{\mathrm{f}}}{L}, \quad F_{\mathrm{r},y} \approx \underbrace{F_{\mathrm{r},z}B_{\mathrm{r}}C_{\mathrm{r}}D_{\mathrm{r}}}_{c_{\mathrm{r}}}\alpha_{\mathrm{r}} = c_{\mathrm{r}}\alpha_{\mathrm{r}} \approx c_{\mathrm{r}}\left(- \left(\beta - \frac{l_{\mathrm{r}}\dot{\psi}}{v_c}\right)\right), \tag{2.18}$$

where the distinction between tyre parameters for the front and rear is made in case the different axles have different tyres. As a result of the constant speed assumption, the longitudinal component of $F_{\mathrm{f},y}$ is also neglected ($F_{\mathrm{f},y}\sin(\delta) \approx 0$), finally giving the equations of motion as

$$\begin{aligned}\ddot{\psi} &\approx \frac{1}{I_z}\left(l_f F_{\mathrm{f},y} - l_r F_{\mathrm{r},y}\right) \\ &\approx \frac{1}{I_z}\left(l_{\mathrm{f}}c_{\mathrm{f}}\left(\delta - \left(\beta + \frac{l_{\mathrm{f}}\dot{\psi}}{v_c}\right)\right) - l_{\mathrm{r}}c_{\mathrm{r}}\left(- \left(\beta - \frac{l_{\mathrm{r}}\dot{\psi}}{v_c}\right)\right)\right),\end{aligned} \tag{2.19}$$

$$\begin{aligned}\dot{\beta} &\approx \frac{1}{mv_c}\left(F_{\mathrm{f},y} + F_{\mathrm{r},y}\right) - \dot{\psi} \\ &\approx \frac{1}{mv_c}\left(c_{\mathrm{f}}\left(\delta - \left(\beta + \frac{l_{\mathrm{f}}\dot{\psi}}{v_c}\right)\right) + c_{\mathrm{r}}\left(- \left(\beta - \frac{l_{\mathrm{r}}\dot{\psi}}{v_c}\right)\right)\right),\end{aligned} \tag{2.20}$$

which can be written as a linear state space system

$$\begin{bmatrix}\ddot{\psi} \\ \dot{\beta}\end{bmatrix} = \begin{bmatrix} -\frac{c_{\mathrm{f}}l_{\mathrm{f}}^2 + c_{\mathrm{r}}l_{\mathrm{r}}^2}{I_z v_c} & \frac{c_{\mathrm{r}}l_{\mathrm{r}} - c_{\mathrm{f}}l_{\mathrm{f}}}{I_z} \\ \frac{c_{\mathrm{r}}l_{\mathrm{r}} - c_{\mathrm{f}}l_{\mathrm{f}}}{mv_c^2} - 1 & -\frac{c_{\mathrm{f}} + c_{\mathrm{f}}}{mv_c}\end{bmatrix}\begin{bmatrix}\dot{\psi} \\ \beta\end{bmatrix} + \begin{bmatrix}\frac{l_{\mathrm{f}}c_{\mathrm{f}}}{I_z} \\ \frac{c_{\mathrm{f}}}{mv_c}\end{bmatrix}\delta. \tag{2.21}$$

In order to make the non-linear model more comparable to the linear model, it can be modified with constant speed $v = v_c$, $\dot{v}_x = 0$ and its longitudinal dynamics can be neglected ($F_{\mathrm{f},x} = F_{\mathrm{r},x} = F_{\mathrm{f},y}\sin(\delta) = 0$). This changes the equations of the

non-linear system to

$$\alpha_{\mathrm{f}} = \delta - \tan^{-1}\left(\frac{v_c \sin(\beta) + l_{\mathrm{f}}\dot{\psi}}{v_c \cos(\beta)}\right), \tag{2.22a}$$

$$\alpha_{\mathrm{r}} = -\tan^{-1}\left(\frac{v_c \sin(\beta) - l_{\mathrm{r}}\dot{\psi}}{v_c \cos(\beta)}\right), \tag{2.22b}$$

$$F_{\mathrm{f},z} = mg\frac{l_{\mathrm{r}}}{L}, \tag{2.22c}$$

$$F_{\mathrm{r},z} = mg\frac{l_{\mathrm{f}}}{L}, \tag{2.22d}$$

$$I_z\ddot{\psi} = l_{\mathrm{f}}F_{\mathrm{f},y}\cos(\delta) - F_{\mathrm{r},y}l_{\mathrm{r}}, \tag{2.22e}$$

$$\dot{\beta} = \frac{1}{mv_c}\Big(F_{\mathrm{f},y}\cos(\delta) + F_{\mathrm{r},y}\Big)\cos(\beta) - \dot{\psi}, \tag{2.22f}$$

where again, the lateral tyre forces can be computed under the assumption of pure slip as the longitudinal dynamics have been neglected. Further, it removes the need for $\dot{v}_x$ to be known.

3

System Identification

A mathematical model of a system will be dependent on some system-specific parameters $\boldsymbol{\theta}$ belonging to a parameter space $\Theta \subset \mathbb{R}^{N_\theta}$, where N_θ is the number of parameters. The mathematical model is here expressed as

$$\mathcal{M}(\boldsymbol{\theta}) : \begin{cases} \dot{\boldsymbol{x}}(t) = f(\boldsymbol{x}(t), \boldsymbol{u}, t, \boldsymbol{\theta}),\ \boldsymbol{x}(0) = \boldsymbol{x}_0(\boldsymbol{\theta}) \\ \hat{\boldsymbol{y}}(t) = g(\boldsymbol{x}(t), \boldsymbol{u}, t, \boldsymbol{\theta}) \end{cases}, \tag{3.1}$$

where $\boldsymbol{x}$ is the state of the system, the dynamics of which are described by the differential equation $\dot{\boldsymbol{x}}(t) = f(\boldsymbol{x}(t), \boldsymbol{u}, t, \boldsymbol{\theta})$ with the initial condition $\boldsymbol{x}(0) = \boldsymbol{x}_0(\boldsymbol{\theta})$. The input signal is $\boldsymbol{u}$, t is the time and $\hat{\boldsymbol{y}}$ is the predicted output, described by some measurement function $\hat{\boldsymbol{y}}(t) = g(\boldsymbol{x}(t), \boldsymbol{u}, t, \boldsymbol{\theta})$. The structure of this model may be derived entirely from first principles, then referred to as a white-box model. In some cases, a model based on first principles may however become too complex or otherwise impractical, in which case a completely arbitrary model structure may be used, referred to as a black-box model. A model can also be based on a mix of first principles and more arbitrary structures, existing on a spectrum of grey-box models [27].

In generalised terms, system identification is the process of estimating the values of system parameters $\boldsymbol{\theta}$ of a model $\mathcal{M}(\boldsymbol{\theta})$ from measured data $\boldsymbol{y}^*(t)$. This type of approach is usually employed when the parameter values are difficult to measure directly [28], [29]. System identification can also be a useful approach when using so called grey- or black-box models, where the parameters in the mathematical model are not derived from first principles, whereby the physical meaning of the parameters may be difficult to interpret and measure [29], [30].

When using system identification methods, two common issues to look out for are over- and underfitting. Overfitting occurs when the model is capable of describing the system dynamics very precisely for certain scenarios, but fails in general. This is often a product of the model structure being too complex. The opposite issue can occur if the model structure is not sufficiently complex. This issue is called underfitting and results in the model being unable to accurately describe the dynamics of the real system for any scenario [30]. Both over-and underfitting are primarily of concern when the mathematical model is closer to the black-box end of the spectrum.

Identifying probability distributions is effectively a system identification problem. The probability distribution of a stochastic parameter can be parameterised, and these distribution parameters can then be viewed as system parameters of the mathematical model, the identification of which could then be approached in the same manner as the identification of any typical parameter. A mathematical formulation of the system identification problem is presented in Section 3.1. After this, the concept of *identifiability* is looked at in Section 3.2, which concerns the fundamental possibility of estimating the parameter values of a model based on measured data.

3.1 The Optimisation Problem

Fundamentally, system identification is an optimisation problem. The desire is to create a model of a system which as closely as possible matches the input-output behaviour of the real system. This amounts to minimising the error between the real system's output $\boldsymbol{y}(t)$ and the model predicted values $\hat{\boldsymbol{y}}(t, \boldsymbol{\theta})$ over time. This problem can be formulated as

$$\hat{\boldsymbol{\theta}} = \arg\min_{\boldsymbol{\theta}} \int |\boldsymbol{y}(t) - \hat{\boldsymbol{y}}(t, \boldsymbol{\theta})| \, \mathrm{d}t, \tag{3.2}$$

where $\hat{\boldsymbol{\theta}}$ is a vector containing the estimated parameter values.

In practice, one rarely has access to the exact system output $\boldsymbol{y}(t)$. Instead, one must rely on discrete measurements $\boldsymbol{y}^*(t_k)$, which means that 3.2 becomes

$$\hat{\boldsymbol{\theta}} = \arg\min_{\boldsymbol{\theta}} \sum_{k=0}^{N} |\boldsymbol{y}^*(t_k) - \hat{\boldsymbol{y}}(t_k, \boldsymbol{\theta})| \tag{3.3}$$

where N is the number of discrete samples. Although generally, the squared euclidean norm is more practical to implement, giving

$$\hat{\boldsymbol{\theta}} = \arg\min_{\boldsymbol{\theta}} \underbrace{\sum_{k=0}^{N} ||\boldsymbol{y}^*(t_k) - \hat{\boldsymbol{y}}(t_k, \boldsymbol{\theta})||_2^2}_{\text{Cost function } J(\boldsymbol{\theta})}. \tag{3.4}$$

Measurements are never perfect however, so a value $\boldsymbol{y}^*(t_k)$ is not necessarily a perfect representation of the actual output $\boldsymbol{y}(t_k)$. This issue can be tackled by using more complex cost functions than the one presented in (3.4). Weighted cost functions of the form $J(\boldsymbol{\theta}) = \sum_{k=0}^{N} w_k (\boldsymbol{y}^*(t_k) - \hat{\boldsymbol{y}}(t_k, \boldsymbol{\theta}))^n$ can be used, where the weights w_k can be chosen to give more or less importance to samples deemed to be more or less accurate. Further, the value n can be adjusted to change the relative importance of large deviations between measurement and prediction and smaller differences [27].

3.2 Identifiability

Depending on the structure of the model $\mathcal{M}(\boldsymbol{\theta})$, it may or may not be possible to get the values of all parameters $\boldsymbol{\theta}$ from the measured output $\boldsymbol{y}^*$. If a mathematical

model produces the same output given the same input but with different parameter values, then one cannot definitely conclude what the exact parameter values were, based solely on the output.

To elaborate on this, in [31], a distinction is made between *structural identifiability* and *practical identifiability*. Structural identifiability concerns the ability to identify a parameter value given an infinitely large data set with zero noise. In other words, for a model to be structurally identifiable, its mathematical structure must permit all parameter values to be identified given absolutely ideal data and is thus a model-specific property. Practical identifiability concerns whether or not a parameter value can be estimated from a finite and noise corrupted data set, as one would expect to see in practice. This is not an inherent property of the model structure alone, but also depends on the input signal and quality of the data set. The same model may be practically identifiable for one case but practically unidentifiable for another. Browning *et al.* [31] further suggest that parameter values which can be practically estimated with higher accuracy through other means than system identification may be regarded as being practically unidentifiable.

Several definitions for structural identifiability have been proposed [32]–[35].
Lecourtier *et al.* [33] present a definition for identifiability given a model $\mathcal{M}(\boldsymbol{\theta})$ and $\mathcal{M}(\hat{\boldsymbol{\theta}})$. Assuming these models have the same output for any input $\boldsymbol{u}$ in the full space of admissible inputs $\mathcal{U}$. A parameter θ_i is structurally locally identifiable (SLI) if, and only if,

$$\left.\begin{array}{c} \hat{\boldsymbol{\theta}} \in \mathcal{V}(\boldsymbol{\theta}) \subset \Theta \\ \hat{\boldsymbol{y}}(\hat{\boldsymbol{\theta}}, t) = \hat{\boldsymbol{y}}(\boldsymbol{\theta}, t)\ \forall t \in \mathbb{R}^+,\ \forall \boldsymbol{u} \in \mathcal{U} \end{array}\right\} \Rightarrow \hat{\theta}_i = \theta_i. \tag{3.5}$$

Here, $\mathcal{V}(\boldsymbol{\theta})$ denotes a vicinity of $\boldsymbol{\theta}$. Formulating this definition in words is similar to the explanation presented in the opening paragraph of this section. This condition states that if there are two parameter sets from within a certain area within the full parameter space and the system output with both parameter sets is the same for all time and all possible input signals, then a given parameter within the vector of parameters is SLI if, and only if, it is implied that the same parameter in the other parameter vector has the same value. Further θ_i is structurally globally identifiable (SGI) if, and only if, $\mathcal{V}(\boldsymbol{\theta})$ can be extended to all of Θ without breaking condition 3.5. Lastly, a model $\mathcal{M}$ is only SLI or SGI, if, and only if, all its parameters θ_i are SLI or SGI respectively.

There are multiple ways of testing the identifiability of models [32], [34]. One method, based on observability analysis is presented by [36]. For a linear time invariant (LTI) system of the form

$$\begin{aligned} \dot{\boldsymbol{x}}(t) &= \underline{A}\boldsymbol{x}(t) + \underline{B}\boldsymbol{u}(t) \\ \boldsymbol{y}(t) &= \underline{C}\boldsymbol{x}(t) + \underline{D}\boldsymbol{u}(t), \end{aligned} \tag{3.6}$$

the observability for matrix for that LTI system can be formulated as

$$\underline{\mathcal{O}}_{\mathrm{L}} = \begin{bmatrix} \underline{C} \\ \underline{C}\underline{A} \\ \underline{C}\underline{A}^2 \\ \vdots \\ \underline{C}\underline{A}^{N-1} \end{bmatrix}, \tag{3.7}$$

where N is the number of states in $\boldsymbol{x}$. If this matrix is full rank, then the system's state is observable from the perfect system output $\boldsymbol{y}$. This condition will be referred to as an observability rank condition (ORC) [36], [37].

If the system model is non-linear however, the above suggested method can no longer be used. For a non-linear model of the form

$$\begin{aligned} \dot{\boldsymbol{x}}(t) &= \boldsymbol{f}(\boldsymbol{x}(t), \boldsymbol{u}(t)) \\ \boldsymbol{y} &= \boldsymbol{g}(\boldsymbol{x}(t)), \end{aligned} \tag{3.8}$$

one can turn to the non-linear observability matrix

$$\underline{\mathcal{O}}_{\mathrm{NL}}(\boldsymbol{x}) = \begin{bmatrix} \frac{\partial}{\partial \boldsymbol{x}} \boldsymbol{y}(t) \\ \frac{\partial}{\partial \boldsymbol{x}} \dot{\boldsymbol{y}}(t) \\ \frac{\partial}{\partial \boldsymbol{x}} \ddot{\boldsymbol{y}}(t) \\ \vdots \\ \frac{\partial}{\partial \boldsymbol{x}} \boldsymbol{y}^{N-1}(t) \end{bmatrix} = \begin{bmatrix} \frac{\partial}{\partial \boldsymbol{x}} \boldsymbol{g}(\boldsymbol{x}) \\ \frac{\partial}{\partial \boldsymbol{x}} (L_{\boldsymbol{f}} \boldsymbol{g}(\boldsymbol{x})) \\ \frac{\partial}{\partial \boldsymbol{x}} (L_{\boldsymbol{f}}^2 \boldsymbol{g}(\boldsymbol{x})) \\ \vdots \\ \frac{\partial}{\partial \boldsymbol{x}} (L_{\boldsymbol{f}}^{N-1} \boldsymbol{g}(\boldsymbol{x})) \end{bmatrix}, \tag{3.9}$$

where the Lie derivative of $g(\boldsymbol{x}(t))$ with respect to $f(\boldsymbol{x}(t))$ is

$$L_{\boldsymbol{f}} \boldsymbol{g}(\boldsymbol{x}(t)) = \frac{\partial \boldsymbol{g}(\boldsymbol{x}(t))}{\partial \boldsymbol{x}(t)} \boldsymbol{f}(\boldsymbol{x}(t)). \tag{3.10}$$

In order to compute higher order Lie derivatives, the recursion

$$\begin{aligned} L_{\boldsymbol{f}}^2 \boldsymbol{g}(\boldsymbol{x}(t)) &= \frac{\partial L_{\boldsymbol{f}} \boldsymbol{g}(\boldsymbol{x}(t))}{\partial \boldsymbol{x}(t)} \boldsymbol{f}(\boldsymbol{x}(t)), \\ &\vdots \\ L_{\boldsymbol{f}}^k \boldsymbol{g}(\boldsymbol{x}(t)) &= \frac{\partial L_{\boldsymbol{f}}^{k-1} \boldsymbol{g}(\boldsymbol{x}(t))}{\partial \boldsymbol{x}(t)} \boldsymbol{f}(\boldsymbol{x}(t)), \end{aligned} \tag{3.11}$$

may be used. If the matrix $\mathcal{O}_{NL}(\boldsymbol{x}_0)$ is full rank for a given constant input $\boldsymbol{u}(t)$, then the model is said to be locally observable around $\boldsymbol{x}_0$. This is merely a sufficient- and not a necessary condition however. If a system fails to meet this condition, it is not necessarily unobservable. Villaverde [36] states that in practice however, this ORC can be considered as a *strong indication* towards the observability of the system. They go on to state that although the condition is insufficient to prove global observability, locally observable systems are often also globally observable in many practical applications.

Each column of both $\underline{\mathcal{O}}_{\mathrm{L}}$ and $\underline{\mathcal{O}}_{\mathrm{NL}}$ is the partial derivative with respect to a certain state variable. In the case the ORC is not fulfilled, one can test the observability of individual state variables by removing the corresponding column from the observability matrix. If the rank of the matrix remains unchanged, the corresponding variable is unobservable in the case of the linear observability matrix. In the case of the non-linear observability matrix, this would merely mean that observability for that state variable cannot be guaranteed [36].

Identifiability can be considered as a special case of observability. To check whether a set of parameters $\boldsymbol{\theta}$ is identifiable, one can build an augmented system with state vector

$$\tilde{\boldsymbol{x}}(t) = \begin{bmatrix} \boldsymbol{x}(t) \\ \boldsymbol{\theta} \end{bmatrix}, \quad \begin{bmatrix} \dot{\boldsymbol{x}}(t) \\ \dot{\boldsymbol{\theta}} \end{bmatrix} = \begin{bmatrix} \underline{A}(\boldsymbol{\theta}) & \underline{0} \\ \underline{0} & \underline{0} \end{bmatrix} \begin{bmatrix} \boldsymbol{x}(t) \\ \boldsymbol{\theta} \end{bmatrix} + \begin{bmatrix} \underline{B}(\boldsymbol{\theta}) \\ \underline{0} \end{bmatrix}, \tag{3.12}$$

where the states $\boldsymbol{\theta}$ are modelled as being constant with no dynamics [36]. If the augmented system is an LTI system, then structural global identifiability can be tested by computing (3.7) for the augmented system and checking if this meets the ORC. The ORC in the LTI case is a sufficient and necessary condition. In many cases a system will be non-linear with respect to its parameters however, and one will have to turn to (3.9). If the augmented system fulfils the ORC however, only local identifiability is guaranteed. Since the condition is only sufficient but not necessary, even if the ORC is not met, the system may still be identifiable.

4

Polynomial Chaos Expansion

This chapter covers the theoretical background of the PCE, whereas the practical implementation is described in Chapter 5. In essence, the intrusive polynomial chaos expansion provides a means to describing the statistics of a given stochastic system by transforming it into a function-point in an infinite-dimensional function space. Generalised polynomial chaos (gPC) is introduced in Section 4.2, with the concept of a function space explained in Section 4.1. To address some of the limitations posed by this polynomial chaos (PC), the Karhunen-Loève expansion (KLE) is introduced in Section 4.3.

Wiener [38], Xiu and Karniadakis [39], Fisher [9] and Gahnem and Spanos [8] all provide more mathematical background and go into more mathematical detail. The level of detail in this coverage has been adapted to the scope of this project.

4.1 Function Spaces

The polynomial chaos expansion introduced in Section 4.2 is an exact representation of a random variable in an ideally infinite-dimensional function space. Therefore, in this section, the idea of a *function space* is first presented. Most readers will likely be familiar with the concept of number valued basis vectors spanning some possibly multi-dimensional space, such as the vectors

$$\hat{\boldsymbol{e}}_1 = \begin{bmatrix} 1 & 0 \end{bmatrix}^\intercal, \tag{4.1a}$$

$$\hat{\boldsymbol{e}}_2 = \begin{bmatrix} 0 & 1 \end{bmatrix}^\intercal, \tag{4.1b}$$

which span a 2D space. We can also consider a different type of space, for example the space spanned by functions $\phi_1(x)$ and $\phi_2(x)$. We may proceed to define a point (a_1, a_2) in this space, such that the point represents the function

$$f(x) = a_1\phi_1(x) + a_2\phi_2(x). \tag{4.2}$$

This definition carries similarities to the definition of a point (b_1, b_2) in physical 2D space,

$$\boldsymbol{b} = b_1\hat{\boldsymbol{e}}_1 + b_2\hat{\boldsymbol{e}}_2, \tag{4.3}$$

where $\hat{\boldsymbol{e}}_1$ and $\hat{\boldsymbol{e}}_2$ are the basis vectors of that space [40].

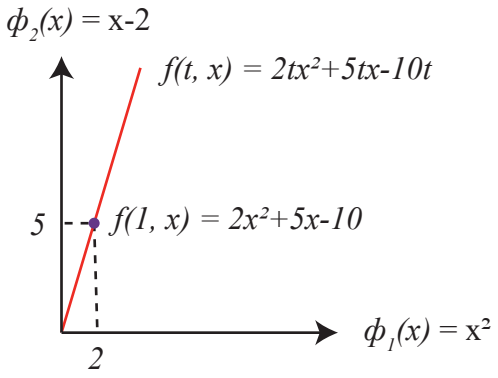

Figure 4.1: An illustration of a two dimensional function space with all functions $f(t,x) = 2tx^2 + 5tx - 10t$ for $t \in \mathbb{R}$ marked.

As an example, the function $f(x) = 2x^2 + 5x - 10$ can be represented by the coordinates $(2, 5)$ in the function space spanned by $\phi_1(x) = x^2$ and $\phi_2(x) = x - 2$. We can also describe all functions $f(t,x) = 2tx^2 + 5tx - 10t$ where $t \in \mathbb{R}$ as a line through the same function space defined by the coordinates $(2t, 5t)$, which has been illustrated in Figure 4.1.

Continuing the analogy between a vector space and a function space, we can define a scalar- or inner product between two functions over the domain of x, $\mathcal{D}_x$ as

$$\langle f(x)g(x)\rangle_w = \int_{\mathcal{D}_x} f(x)g(x)w(x)\,\mathrm{d}x, \tag{4.4}$$

where $w(x)$ is a weighting function chosen to decide the character of the scalar product. This scalar product between two function has the same property as the scalar product between two vectors. As such, the scalar product of a function and itself $\langle f(x)f(x)\rangle_w$ evaluates to a non negative numerical value f^2, and can be interpreted as its magnitude. The function $f(x)$ can also said to be normal if its scalar product with itself $\langle f(x)f(x)\rangle_w = f^2 = 1$. With this scalar product, orthogonality of functions is defined analogously to the vector case. Two functions $f(x)$ and $g(x)$ are orthogonal if their scalar product $\langle f(x)g(x)\rangle_w$ is zero [40]. They are then said to be orthogonal with respect to the weighting function $w(x)$.

A set of polynomials $\{\phi_n(x), n \in \mathcal{Q}\}$ where

$$\mathcal{Q} = \mathbb{N} \tag{4.5}$$

for an infinite series or

$$\mathcal{Q} = \{0,\, 1,\, 2\, \ldots,\, n_{\max}\},\ n_{\max} \in \mathbb{N} \tag{4.6}$$

for a finite series, is orthogonal with respect to some weighting function $w(x)$ if

$$\langle \phi_n(x),\, \phi_m(x)\rangle_w = \phi_n^2 \delta_{nm},\ \forall n,\, m \in \mathcal{Q} \tag{4.7}$$

where

$$\delta_{ij} = \begin{cases} 1, & \text{if } i = j \\ 0, & \text{if } i \neq j \end{cases} \tag{4.8}$$

Table 4.1: The first five Hermite polynomials.

n	$H_n(\zeta)$	H_n^2
0	1	$\sqrt{\pi}$
1	2ζ	$2\sqrt{\pi}$
2	$4\zeta^2 - 2$	$8\sqrt{\pi}$
3	$8\zeta^3 - 12\zeta$	$48\sqrt{\pi}$
4	$16\zeta^4 - 48\zeta^2 + 12$	$384\sqrt{\pi}$

is the Kronecker Delta function [9], [41]. If all polynomials in the set are also normal, then the set is referred to as *orthonormal*.

4.2 Wiener-Askey Polynomial Chaos

In effort to describe the statistics of dynamic systems pertaining mainly to fluids and gasses. Wiener [38] first defines *homogeneous chaos* in their 1938 work as a the span of Hermite polynomials which are orthogonal with respect to the standard Gaussian distribution $\mathcal{N}(0,1)$. The n^{th} degree Hermite polynomial is defined as

$$H_n(\zeta) = (-1)^n e^{\zeta^2} \frac{\mathrm{d}^n}{\mathrm{d}\zeta^n} e^{-\zeta^2}, \tag{4.9}$$

where $e^{-\zeta^2}$ is the weighting function $w(\zeta)$ with respect to which the Hermite polynomials are orthogonal. This function is similar to the probability density function $p_{\mathcal{N}}(\zeta)$ of the standard normal distribution $\mathcal{N}(0,1)$

$$p_{\mathcal{N}}(\zeta) = \frac{1}{\sqrt{2\pi}} e^{-\frac{\zeta^2}{2}}, \tag{4.10}$$

except for some constants. The Hermite polynomials can be scaled such that

$$He_n(\zeta) = H_n\left(\frac{\zeta}{\sqrt{2}}\right), \tag{4.11}$$

which are then orthogonal with respect to

$$w(\zeta) = e^{-\frac{\zeta^2}{2}}. \tag{4.12}$$

For further clarity, the first five Hermite polynomials have been listed in Table 4.1 along with their magnitudes $\langle H_n(\zeta), H_n(\zeta)\rangle_w = H_n^2$, which take the general form $2^n n!\sqrt{\pi}$ [42]. The same polynomials have also been normalised and plotted on the interval $[-1, 1]$ in Figure 4.2.

With a set of independent Gaussian random variables $\boldsymbol{\xi} = \{\xi_i(\Delta)\}_{i=1}^{\infty}$, Wiener's [38] homogeneous chaos expansion then allows a random process $x(\Delta)$ with finite second

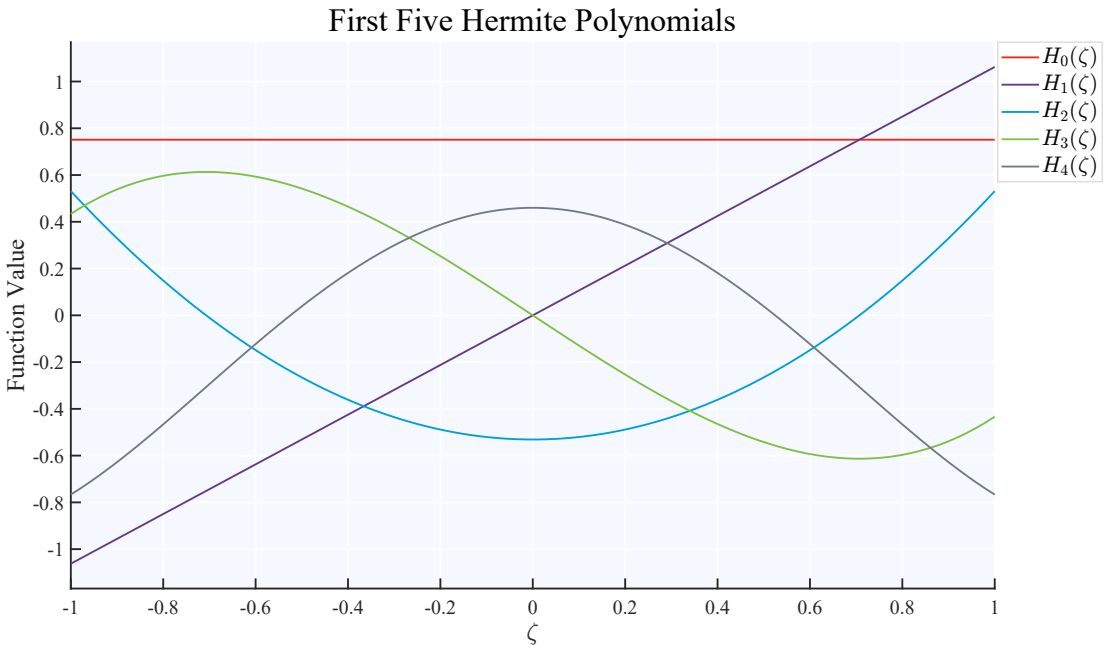

Figure 4.2: The first five Hermite polynomials plotted on the span $[-1, 1]$, each normalised.

order moment to be expressed as

$$\begin{aligned} x(\Delta) = \hat{X}_0 He_0 \\ + \sum_{i_1=1}^{\infty} \hat{X}_{i_1} He_1(\xi_{i_1}(\Delta)) \\ + \sum_{i_1=1}^{\infty} \sum_{i_2=1}^{i_1} \hat{X}_{i_1 i_2} He_2(\xi_{i_1}(\Delta), \xi_{i_2}(\Delta)) \\ + \sum_{i_1=1}^{\infty} \sum_{i_2=1}^{i_1} \sum_{i_3=1}^{i_2} \hat{X}_{i_1 i_2 i_3} He_3(\xi_{i_1}(\Delta), \xi_{i_2}(\Delta), \xi_{i_3}(\Delta)) + \dots, \end{aligned} \tag{4.13}$$

where

$$He_n(\xi_{i_1}(\Delta), \xi_{i_2}(\Delta), \dots, \xi_{i_n}(\Delta)) \tag{4.14}$$

is the multivariate Hermite chaos of order n in the variables

$$\xi_{i_1}(\Delta)\xi_{i_2}(\Delta)\dots\xi_{i_n}(\Delta). \tag{4.15}$$

The multivariate Hermite chaos is the product of several univariate Hermite polynomials of each ξ_i. The degree of each Hermite polynomial is decided by the number of occurrences of ξ_i in the arguments. So

$$He_3(\xi_1(\Delta), \xi_1(\Delta), \xi_2(\Delta)) = He_2(\xi_1(\Delta)) He_1(\xi_2(\Delta)). \tag{4.16}$$

Note in this example that the first Hermite polynomial has degree two since $\xi_1(\Delta)$ occurs twice in the arguments of $He_3(\xi_1(\Delta), \xi_1(\Delta), \xi_2(\Delta))$. As $\xi_2(\Delta)$ only occurs once, the second Hermite polynomial is of degree one. Here, each random variable

$\xi_i(\Delta) \sim \mathcal{N}(0,1)$ is a standard Gaussian variable, i.e. they each have zero mean and unit variance (a variance of one) [39] and $\hat{X}_i$ are the expansion coefficients specific to $x(\Delta)$, which have to be computed. The variable Δ is a random event, i.e. one particular random outcome or realisation. In [9], [39], details of the formal definition of this underlying random event can be found. These details are however omitted in this thesis, as the mathematical definition is not necessary for the rest of this explanation. Further, for notational convenience, the random variable $x(\Delta)$ will instead be referred to as $x(\boldsymbol{\xi})$.

The Hermite chaos is ideal for Gaussian random variables. For the more general case, the *Askey scheme* can be used as the basis for expansion. This scheme contains families of orthogonal polynomials with other probability distribution functions as weighting functions in their respective orthogonality conditions, creating a more generalised version of the Wiener polynomial chaos. The relationships between the polynomial families and probability distributions are presented in Table 4.2 [9], [39]. As an example, the first five Legendre polynomials have been listed in Table 4.3 along with the general definition. The normalised versions of the same five polynomials have also been plotted in Figure 4.3 [43]. These polynomials are orthogonal with respect to

$$w(\zeta) = 1, \tag{4.17}$$

which is the same as the PDF $p_{\mathcal{U}}(\zeta)$ of the uniform distribution $\mathcal{U}(-1,1)$,

$$p_{\mathcal{U}}(\zeta) = \frac{1}{2},\ \zeta \in [-1,\ 1], \tag{4.18}$$

except for some constant.

Table 4.2: Different types of stochastic distributions and their corresponding polynomial chaoses.

Type of Distribution	Polynomial chaos
Gaussian	Hermite chaos
Uniform	Legendre chaos
Gamma	Laguerre chaos
Beta	Jacobi chaos
Poisson	Charlier chaos
Negative binomial	Meixner chaos
Binomial	Krawtchouk chaos
Hypergeometric	Hahn chaos

With this generalised scheme, a more general expansion of a random variable with

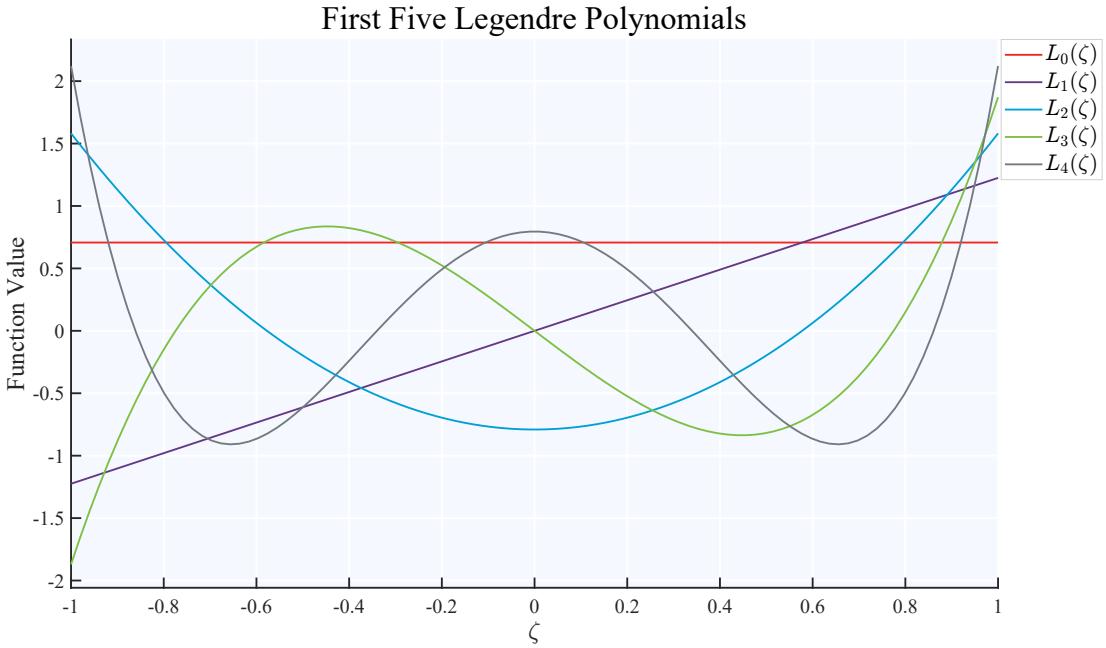

Figure 4.3: The first five Legendre polynomials plotted on the span $[-1, 1]$, each normalised.

Table 4.3: The first five Legendre polynomials.

n	$L_n(\zeta)$	L_n^2
0	1	2
1	ζ	$\frac{2}{3}$
2	$\frac{1}{2}\left(3\zeta^2 - 1\right)$	$\frac{2}{5}$
3	$\frac{1}{2}\left(5\zeta^3 - 3\zeta\right)$	$\frac{2}{7}$
4	$\frac{1}{2}\left(35\zeta^4 - 30\zeta^2 + 3\right)$	$\frac{2}{9}$
$\vdots$	$\vdots$	$\vdots$
n	$\frac{1}{2^n n!}\frac{\mathrm{d}^n}{\mathrm{d}\zeta^n}(\zeta^2 - 1)^n$	$\frac{2}{2n+1}$

finite second order moment $x(\boldsymbol{\xi})$ can be written as

$$\begin{aligned} x(\boldsymbol{\xi}) = \hat{X}_0 I_0 \\ + \sum_{i_1=1}^{\infty} \hat{X}_{i_1} I_1(\xi_{i_1}) \\ + \sum_{i_1=1}^{\infty} \sum_{i_2=1}^{i_1} \hat{X}_{i_1 i_2} I_2(\xi_{i_1}, \xi_{i_2}) \\ + \sum_{i_1=1}^{\infty} \sum_{i_2=1}^{i_1} \sum_{i_3=1}^{i_2} \hat{X}_{i_1 i_2 i_3} I_3(\xi_{i_1}, \xi_{i_2}, \xi_{i_3}) + \dots, \end{aligned} \tag{4.19}$$

where $I_n(\xi_{i_1}, \xi_{i_2}, \dots, \xi_{i_n})$ is the the appropriate multivariate Wiener-Askey polynomial chaos of order n. The polynomial chaoses I_n are structured in a similar manner to the multivariate Hermite chaos in (4.16).

The PCE can be presented on a more compact form using a multi-index vector $\boldsymbol{\alpha}_{i_1 i_2 \dots i_n}$. Each $\boldsymbol{\alpha}_{i_1 i_2 \dots i_n}$ corresponds to a given function $I_n(\xi_{i_1}, \xi_{i_2}, \dots, \xi_{i_n})$ such that the value of each element i of $\boldsymbol{\alpha}_{i_1 i_2 \dots i_n}$ is the number of occurrences of ξ_i in the arguments to the function $I_n(\xi_{i_1}, \xi_{i_2}, \dots, \xi_{i_n})$. With this multi-index-scheme, the corresponding polynomial chaos can be written as

$$I_n(i_1, i_2, \dots, i_n) = \prod_{i=0}^{\infty} P_{\alpha_{ki}}(\xi_i), \tag{4.20}$$

where $P_{\alpha_{ki}}(\xi_i)$ is the α_{ki}^{th} order polynomial of the type corresponding to the probability distribution of ξ_i, with $k = i_1 i_2 \dots i_n$ [44]. The total polynomial order (TPO) n is the sum of all α_{ki} for a fixed k and $i = 1, 2, \dots, \infty$.

As an example, consider a system described by N_p random variables, such that $\boldsymbol{\xi} = \{\xi_i\}_{i=1}^{N_p}$. Also consider the *PCE order*, N_{PCE}. Let the PCE order be a truncation of the expansion, whereby only polynomials up to degree N_{PCE} are considered. The finite N_p and truncation N_{PCE} restrict the expansion from (4.19) to

$$\begin{aligned} x(\boldsymbol{\xi}) \approx \hat{X}_0 \phi_0 \\ + \sum_{i_1=1}^{N_p} \hat{X}_{i_1} I_1(\xi_{i_1}) \\ + \sum_{i_1=1}^{N_p} \sum_{i_2=1}^{i_1} \hat{X}_{i_1 i_2} I_2(\xi_{i_1}, \xi_{i_2}) \\ + \sum_{i_1=1}^{N_p} \sum_{i_2=1}^{i_1} \sum_{i_3=1}^{i_2} \hat{X}_{i_1 i_2 i_3} I_3(\xi_{i_1}, \xi_{i_2}, \xi_{i_3}) + \dots \\ + \sum_{i_1=1}^{N_p} \sum_{i_2=1}^{i_1} \dots \sum_{i_{N_{\text{PCE}}}=1}^{i_{N_{\text{PCE}}-1}} \hat{X}_{i_1 i_2 \dots i_{N_{\text{PCE}}}} I_{N_{\text{PCE}}}(\xi_{i_1}, \xi_{i_2}, \dots, \xi_{i_{N_{\text{PCE}}}}). \end{aligned} \tag{4.21}$$

This sums the polynomial chaoses of all possible combinations of $\{\xi_i\}_{i=0}^{N_p}$ up to the total polynomial order (TPO) N_{PCE} [45], meaning that the total number of terms

ends up being

$$N_\phi = \frac{(N_p + N_{\text{PCE}})!}{N_p! N_{\text{PCE}}!}. \tag{4.22}$$

If we use $N_p = 2$, where $\xi_1 \sim \mathcal{N}(0,1)$ and $\xi_2 \sim \mathcal{U}(-1,1)$, then we get the expansion coefficients and polynomials which are presented in Table 4.4. In these polynomials, $He_n(\xi_i)$ is the Hermite polynomial of degree n, corresponding to the Gaussian random variable ξ_1 and $L_n(\xi_i)$ is the n^{th} degree Legendre polynomial corresponding to the uniformly distributed ξ_2.

A more convenient notation can be formulated by rewriting the polynomial chaoses such that the polynomial from term i is referred to as $\phi_i(\boldsymbol{\xi})$ and the coefficient from each term i is denoted as X_i. The expansion can then be written as

$$x(\boldsymbol{\xi}) = \sum_{i=0}^{\infty} X_i \phi_i(\boldsymbol{\xi}),\ \boldsymbol{\xi} = \begin{bmatrix} \xi_1 & \xi_2 & \dots \end{bmatrix}. \tag{4.23}$$

The correspondence between the coefficients and polynomials of the two notation schemes (4.19) and (4.23) is also exemplified in Table 4.4. In addition, a visual representation of the polynomial $\phi_8(\boldsymbol{\xi})$ from Table 4.4 has been normalised and plotted in Figure 4.4 along with the underlying normalised Hermite and Legendre polynomials. As was mentioned earlier, the PCE of $x(\boldsymbol{\xi})$ is its representation in a function space. With the representation in (4.23), it becomes apparent that this function space is spanned by the polynomials $\phi_k(\boldsymbol{\xi})$, and in this function space $x(\boldsymbol{\xi})$ is represented by the coordinates $(X_1,\ X_2,\ X_3,\ \dots)$ as illustrated in Figure 4.5. In the figure, the stochastic variable $x(\boldsymbol{\xi})$ has an uncertain position along the basis vector $\hat{\boldsymbol{e}}_1$, but it can be approximated by expansion into the function space spanned by $\phi_1(\boldsymbol{\xi})$, $\phi_2(\boldsymbol{\xi})$ and $\phi_3(\boldsymbol{\xi})$. When the dimensions of the function space are truncated, the second order moments of the random variable are no longer exact.

4.2.1 Statistics with the Polynomial Chaos Expansion

The motivation behind the expansion was to compute the statistics of the original variable $x(\boldsymbol{\xi})$. So far, it has not become apparent how that can be done. This will be clarified further in this section.

The expectation or mean of a variable $x(\boldsymbol{\xi})$, where $\boldsymbol{\xi}$ is some random variable with probability distribution $P(\boldsymbol{\xi})$ associated with probability density function $p(\boldsymbol{\xi})$, can be expressed as

$$\begin{aligned} \mathbb{E}[x(\boldsymbol{\xi})] &= \int_{\mathcal{D}_{\boldsymbol{\xi}}} x(\boldsymbol{\xi})\, \mathrm{d}P(\boldsymbol{\xi}) \\ &= \int_{\mathcal{D}_{\boldsymbol{\xi}}} x(\boldsymbol{\xi}) p(\boldsymbol{\xi})\, \mathrm{d}\boldsymbol{\xi} = \langle x(\boldsymbol{\xi}),\ 1 \rangle_p \end{aligned} \tag{4.24}$$

where $\mathcal{D}_{\boldsymbol{\xi}}$ is the domain of $\boldsymbol{\xi}$. Given the PCE $x(\boldsymbol{\xi}) = \sum_{i=0}^{\infty} X_i \phi_i(\boldsymbol{\xi})$, (4.24) becomes

$$\mathbb{E}[x(\boldsymbol{\xi})] = \left\langle \sum_{i=0}^{\infty} X_i \phi_i(\boldsymbol{\xi}),\ 1 \right\rangle_p, \tag{4.25}$$

Table 4.4: Coefficients and polynomials relating to an example expansion using $N_p = 2$ and $N_{\text{PCE}} = 3$. The total polynomial order is also listed.

Term i	$\boldsymbol{\alpha}_i$	$X_i = \hat{X}_k$	$\phi_i(\boldsymbol{\xi}) = I_n(\hat{\boldsymbol{\xi}}_i)$	TPO
0	$\begin{bmatrix}0 & 0\end{bmatrix}$	$X_0 = \hat{X}_0$	$\phi_0(\boldsymbol{\xi}) = I_0 = He_0(\xi_1)L_0(\xi_2)$	0
1	$\begin{bmatrix}1 & 0\end{bmatrix}$	$X_1 = \hat{X}_1$	$\phi_1(\boldsymbol{\xi}) = I_1(\xi_1) = He_1(\xi_1)L_0(\xi_2)$	1
2	$\begin{bmatrix}0 & 1\end{bmatrix}$	$X_2 = \hat{X}_2$	$\phi_2(\boldsymbol{\xi}) = I_1(\xi_2) = He_0(\xi_1)L_1(\xi_2)$	1
3	$\begin{bmatrix}2 & 0\end{bmatrix}$	$X_3 = \hat{X}_{11}$	$\phi_3(\boldsymbol{\xi}) = I_2(\xi_1, \xi_1) = He_2(\xi_1)L_0(\xi_2)$	2
4	$\begin{bmatrix}1 & 1\end{bmatrix}$	$X_4 = \hat{X}_{21}$	$\phi_4(\boldsymbol{\xi}) = I_2(\xi_2, \xi_1) = He_1(\xi_1)L_1(\xi_2)$	2
5	$\begin{bmatrix}0 & 2\end{bmatrix}$	$X_5 = \hat{X}_{22}$	$\phi_5(\boldsymbol{\xi}) = I_2(\xi_2, \xi_2) = He_0(\xi_1)L_2(\xi_2)$	2
6	$\begin{bmatrix}3 & 0\end{bmatrix}$	$X_6 = \hat{X}_{111}$	$\phi_6(\boldsymbol{\xi}) = I_3(\xi_1, \xi_1, \xi_1) = He_3(\xi_1)L_0(\xi_2)$	3
7	$\begin{bmatrix}2 & 1\end{bmatrix}$	$X_7 = \hat{X}_{211}$	$\phi_7(\boldsymbol{\xi}) = I_3(\xi_2, \xi_1, \xi_1) = He_2(\xi_1)L_1(\xi_2)$	3
8	$\begin{bmatrix}1 & 2\end{bmatrix}$	$X_8 = \hat{X}_{221}$	$\phi_8(\boldsymbol{\xi}) = I_3(\xi_2, \xi_2, \xi_1) = He_1(\xi_1)L_2(\xi_2)$	3
9	$\begin{bmatrix}0 & 3\end{bmatrix}$	$X_9 = \hat{X}_{222}$	$\phi_9(\boldsymbol{\xi}) = I_3(\xi_2, \xi_2, \xi_2) = He_0(\xi_1)L_3(\xi_2)$	3

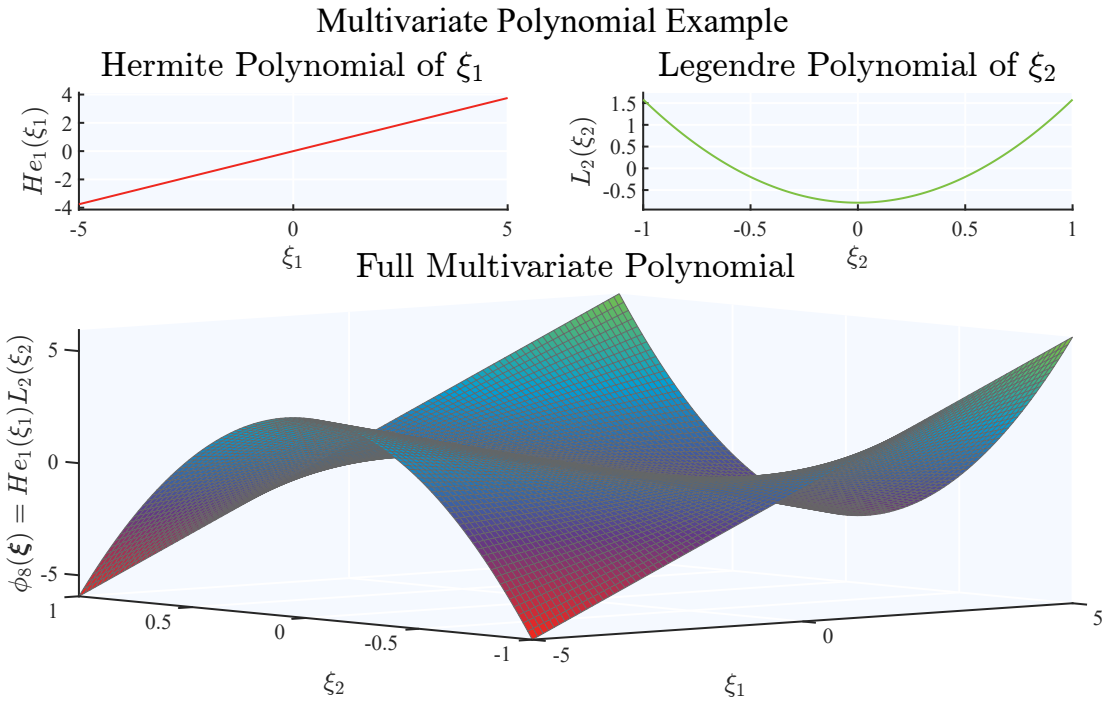

Figure 4.4: The basis polynomial $\phi_8(\boldsymbol{\xi})$ normalised and plotted.

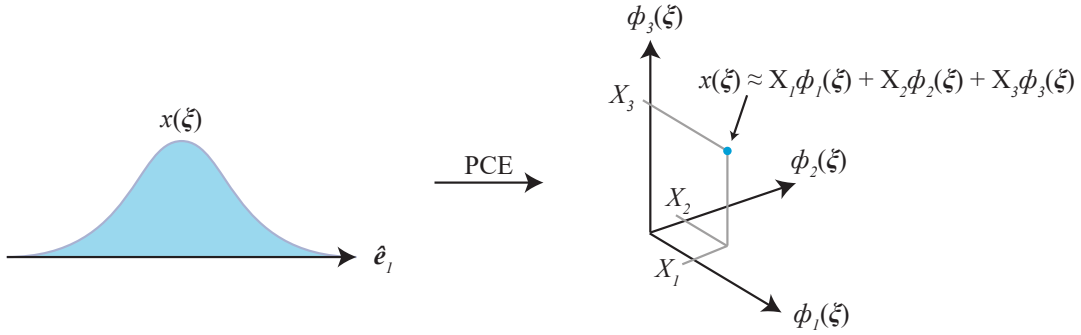

Figure 4.5: An illustration of the principle behind the PCE.

where $p(\boldsymbol{\xi})$ is the probability density function of $\boldsymbol{\xi}$. Keeping in mind that the basis polynomials $\phi_i(\boldsymbol{\xi})$ have specifically been chosen to be orthogonal with respect to the probability distribution $p(\boldsymbol{\xi})$, meaning $\langle \phi_n(\boldsymbol{\xi}),\, \phi_m(\boldsymbol{\xi}) \rangle_p = \phi_n^2 \delta_{nm}$, and also keeping in mind that $\phi_0(\boldsymbol{\xi}) = 1$, we get

$$\mathbb{E}[x(\boldsymbol{\xi})] = \left\langle \sum_{i=0}^{\infty} X_i \phi_i(\boldsymbol{\xi}),\, \phi_0(\boldsymbol{\xi}) \right\rangle_p = \sum_{i=0}^{\infty} X_i \left\langle \phi_i(\boldsymbol{\xi}),\, \phi_0(\boldsymbol{\xi}) \right\rangle_p = \sum_{i=0}^{\infty} X_i \phi_i^2 \delta_{i0} = X_0 \phi_0^2. \tag{4.26}$$

If the orthonormal version of the polynomial basis is used, this gives all $\phi_n^2 = 1$ and thus $\mathbb{E}[x(\boldsymbol{\xi})] = X_0$.

Expressing the variance of $x(\boldsymbol{\xi})$, we first observe that

$$\begin{aligned} &\mathbb{E}[(x(\boldsymbol{\xi}) - \mathbb{E}[x(\boldsymbol{\xi})])^2] = \mathbb{E}\Big[x^2 - 2x\mathbb{E}[x(\boldsymbol{\xi})] + \mathbb{E}^2[x(\boldsymbol{\xi})]\Big] \\ &= \mathbb{E}[x^2(\boldsymbol{\xi})] - 2\mathbb{E}[x(\boldsymbol{\xi})]\mathbb{E}[x(\boldsymbol{\xi})] + \mathbb{E}^2[x] = \mathbb{E}[x^2(\boldsymbol{\xi})] - \mathbb{E}^2[x(\boldsymbol{\xi})]. \end{aligned} \tag{4.27}$$

Inserting the PCE of $x(\boldsymbol{\xi})$ into this expression, keeping in mind that $\mathbb{E}[x(\boldsymbol{\xi})] = \phi_0^2 X_0$, we arrive at

$$\mathbb{E}[x^2(\boldsymbol{\xi})] - \mathbb{E}^2[x(\boldsymbol{\xi})] = \left\langle \Big(\sum_{i=0}^{\infty} X_i \phi_i(\boldsymbol{\xi}) \Big)^2,\, 1 \right\rangle_p - (\phi_0^2 X_0)^2. \tag{4.28}$$

The square of a sum

$$\Big(\sum_i a_i \Big)^2 = \sum_i a_i^2 + 2 \sum_{i<j} a_i a_j \tag{4.29}$$

gives

$$\left\langle \Big(\sum_{i=0}^{\infty} X_i \phi_i(\boldsymbol{\xi}) \Big)^2,\, 1 \right\rangle_p = \sum_{i=0}^{\infty} X_i^2 \left\langle \phi_i^2(\boldsymbol{\xi}) \right\rangle_p + \sum_{j=1,\, i<j}^{\infty} \left\langle X_i \phi_i,\, X_j \phi_j \right\rangle_p, \tag{4.30}$$

which, given the orthogonality of the polynomials, reduces to

$$\sum_{i=0}^{\infty} X_i^2 \left\langle \phi_i^2(\boldsymbol{\xi}) \right\rangle_p + \sum_{j=1,\, i<j}^{\infty} \left\langle X_i \phi_i,\, X_j \phi_j \right\rangle_p = \sum_{i=0}^{\infty} X_i^2 \phi_i^2, \tag{4.31}$$

since i and j are never the same in the second sum on the left side of (4.31). This leaves

$$\mathbb{E}[(x(\boldsymbol{\xi}) - \mathbb{E}[x(\boldsymbol{\xi})])^2] = \sum_{i=0}^{\infty} X_i^2 \phi_i^2 - \phi_0^4 X_0^2 = \sum_{i=1}^{\infty} X_i^2 \phi_i^2, \tag{4.32}$$

as $\phi_0 = 1$ means that $\phi_0^2 X_0^2 - \phi_0^4 X_0^2 = 0$, leading to the subtraction simply removing the 0^{th} term of the sum. This result also tells us that the coefficients X_i for $i = 1, 2, ...$ are related to the variance of $x(\boldsymbol{\xi})$ with respect to different combinations of ξ_i.

Computing higher order moments from the PCE is more complicated but can be done. Lefebvre [46] covers computation of higher order moments in more detail, as does Gallant [45]. Higher order moments are outside of the scope of thesis and will not be covered here.

4.2.2 Polynomial Chaos Expansion of Dynamic Systems

Until this point, we have focused on a single random variable. The purpose of this section is to shed some light on the application of PCE on dynamic systems with several state variables and stationary uncertainties.

Suppose we have a differential equation

$$\dot{\boldsymbol{x}}(t, \boldsymbol{\xi}) = \boldsymbol{f}(t, \boldsymbol{x}(t, \boldsymbol{\xi}), \boldsymbol{u}). \tag{4.33}$$

The random parameter $\boldsymbol{\xi}$ can be viewed as corresponding to parametric uncertainties in the model through relationships like $\boldsymbol{\theta} = \boldsymbol{h}(\boldsymbol{\xi})$, where $\boldsymbol{h}(\boldsymbol{\xi})$ is some arbitrary function mapping the random variable $\boldsymbol{\xi}$ to parameter values $\boldsymbol{\theta}$. The state trajectory $\boldsymbol{x}(t, \boldsymbol{\xi})$ of this system can be viewed as a random process dependent on the stationary random variable $\boldsymbol{\xi}$. Each state $x_k(t, \boldsymbol{\xi})$ in $\boldsymbol{x}(t, \boldsymbol{\xi})$ can then be expanded using the Wiener-Askey chaos as

$$x_k(t, \boldsymbol{\xi}) = \sum_{i=0}^{\infty} X_{ki}(t) \phi_i(\boldsymbol{\xi}), \tag{4.34}$$

where the PCE coefficients $X_{ki}(t)$ are now deterministic functions of time and the stochastic portion of the system is described by the basis polynomials $\phi_i(\boldsymbol{\xi})$. With this, the differential equation (4.33) can be written as

$$\sum_{i=0}^{\infty} \dot{X}_{ki}(t) \phi_i(\boldsymbol{\xi}) = \boldsymbol{f}\left(t, \sum_{i=0}^{\infty} X_{ki}(t) \phi_i(\boldsymbol{\xi}), \boldsymbol{u}\right). \tag{4.35}$$

By using the Galerkin projection [47] of the equation onto each basis polynomial, the differential equation for each state variable becomes

$$\left\langle \sum_{i=0}^{\infty} \dot{X}_{ki}(t) \phi_i(\boldsymbol{\xi}),\, \phi_j(\boldsymbol{\xi}) \right\rangle_p = \left\langle \boldsymbol{f}\left(t, \sum_{i=0}^{\infty} X_{ki}(t) \phi_i(\boldsymbol{\xi}), \boldsymbol{u}\right),\, \phi_j(\boldsymbol{\xi}) \right\rangle_p,\ j = 0, 1, \ldots, \tag{4.36}$$

for which the orthogonality of the polynomials can be used to give

$$\dot{X}_{kj}(t)\phi_j^2 = \left\langle \boldsymbol{f}\left(t, \sum_{i=0}^{\infty} X_{ki}(t)\phi_i(\boldsymbol{\xi}), \boldsymbol{u}\right), \phi_j(\boldsymbol{\xi})\right\rangle_p, \; j = 0, 1, \ldots. \tag{4.37}$$

With (4.37), it is practically possible to simulate the system given some initial conditions and finite N_p and N_{PCE}. On this general form however, the Galerkin Projection has to be computed at every function evaluation. Which, although possible, may be impractical. But by considering the special case of a linear system

$$\begin{aligned} &\dot{\boldsymbol{x}}(t, \boldsymbol{\xi}) = \underline{A}(\boldsymbol{\xi})\boldsymbol{x}(t, \boldsymbol{\xi}) + \underline{B}(\boldsymbol{\xi})\boldsymbol{u}, \\ &\text{for } t > 0, \text{ given } x(0, \boldsymbol{\xi}) = x_0(\boldsymbol{\xi}), \end{aligned} \tag{4.38}$$

the expansion and Galerkin projection of the system onto each polynomial basis gives the dynamics as

$$\underline{F}\dot{\boldsymbol{X}}(t) = \left\langle \underline{\Phi}(\boldsymbol{\xi}), \underline{A}(\boldsymbol{\xi}), \underline{\Phi}^{\intercal}(\boldsymbol{\xi})\right\rangle_p \boldsymbol{X}(t) + \left\langle \underline{\Phi}(\boldsymbol{\xi}), \underline{B}(\boldsymbol{\xi})\right\rangle_p \boldsymbol{u}, \tag{4.39}$$

where $\boldsymbol{X}(t)$ and $\boldsymbol{u}$ can be moved out of the inner products since they are independent of $\boldsymbol{\xi}$ and

$$\boldsymbol{X}(t) = \begin{bmatrix} X_{10}(t) & X_{11}(t) & \ldots & X_{20}(t) & X_{21}(t) & \ldots & X_{N_{\boldsymbol{x}}0}(t) & X_{N_{\boldsymbol{x}}1}(t) & \ldots \end{bmatrix}^{\intercal}, \tag{4.40}$$

with $N_{\boldsymbol{x}}$ being the number of state variables in $\boldsymbol{x}$,

$$\underline{\Phi}(\boldsymbol{\xi}) = \begin{bmatrix} \phi_0(\boldsymbol{\xi}) & \phi_1(\boldsymbol{\xi}) & \ldots \end{bmatrix}^{\intercal} \otimes \underline{I}_{N_{\boldsymbol{x}}}, \tag{4.41}$$

and

$$\underline{F} = \begin{bmatrix} \phi_0^2 & & \\ & \phi_1^2 & \\ & & \ddots \end{bmatrix}, \tag{4.42}$$

which becomes the identity matrix if the polynomial basis is orthonormal [45]. Similarly, the initial state in the PCE formulation is

$$\underline{F}\boldsymbol{X}(0) = \left\langle \underline{\Phi}(\boldsymbol{\xi}), \boldsymbol{x}(\boldsymbol{\xi}, 0)\right\rangle_p. \tag{4.43}$$

By defining

$$\underline{A}_{\text{PCE}} = \underline{F}^{-1}\left\langle \underline{\Phi}(\boldsymbol{\xi}), \underline{A}(\boldsymbol{\xi}), \underline{\Phi}^{\intercal}(\boldsymbol{\xi})\right\rangle_p, \tag{4.44a}$$

$$\underline{B}_{\text{PCE,d}} = \underline{F}^{-1}\left\langle \underline{\Phi}(\boldsymbol{\xi}), \underline{B}(\boldsymbol{\xi})\right\rangle_p, \tag{4.44b}$$

$$\boldsymbol{X}(0) = \underline{F}^{-1}\left\langle \underline{\Phi}(\boldsymbol{\xi}), \boldsymbol{x}(\boldsymbol{\xi}, 0)\right\rangle_p, \tag{4.44c}$$

we get the augmented system

$$\dot{\boldsymbol{X}} = \underline{A}_{\text{PCE}}\boldsymbol{X}(t) + \underline{B}_{\text{PCE,d}}\boldsymbol{u}. \tag{4.45}$$

If the original system has more state matrices, they can also be expanded in the same manner as $\underline{A}$ and $\underline{B}$ were expanded in this derivation.

An important case to review is when the input $\boldsymbol{u}$ is also stochastic $\boldsymbol{u}(\boldsymbol{\xi})$, for example in the case that state feedback $u(t,\boldsymbol{\xi}) = \underline{K}\boldsymbol{x}(t,\boldsymbol{\xi})$ is used [9], [45]. Each input in $u_k(\boldsymbol{\xi})$ of the control signal can then also be expanded, similarly to how the state vector was expanded previously, into

$$u_k(\boldsymbol{\xi}) = \sum_{i=0}^{\infty} U_{ki}\phi_i(\boldsymbol{\xi}) \tag{4.46}$$

or

$$\boldsymbol{u}(\boldsymbol{\xi}) = \underline{\Phi}^{\intercal}(\boldsymbol{\xi})\boldsymbol{U}. \tag{4.47}$$

This changes the expression for the augmented $\underline{B}$ to be similar to that of $\underline{A}$,

$$\underline{B}_{\text{PCE,s}} = \underline{F}^{-1}\left\langle \underline{\Phi}(\boldsymbol{\xi}),\, \underline{B}(\boldsymbol{\xi}),\, \underline{\Phi}^{\intercal}(\boldsymbol{\xi})\right\rangle_p, \tag{4.48}$$

and the differential equation becomes

$$\dot{\boldsymbol{X}} = \underline{A}_{\text{PCE}}\boldsymbol{X}(t) + \underline{B}_{\text{PCE,s}}\boldsymbol{U}. \tag{4.49}$$

Recall that each inner product is an integral as specified in (4.4). As such, (4.44) and (4.45) are all multi-dimensional integral problems. In the case of the initial conditions (4.44c) for example, takes the form

$$\begin{aligned}\boldsymbol{X}(0) &= \underline{F}^{-1}\int_{\mathcal{D}_{\boldsymbol{\xi}}} \underline{\Phi}(\boldsymbol{\xi})\boldsymbol{x}(\boldsymbol{\xi},0)p(\boldsymbol{\xi})\,\mathrm{d}\boldsymbol{\xi} \\ &= \underline{F}^{-1}\int_{\mathcal{D}_{\xi_0}}\int_{\mathcal{D}_{\xi_1}}\cdots\int_{\mathcal{D}_{\xi_\infty}} \underline{\Phi}(\boldsymbol{\xi})\boldsymbol{x}(\boldsymbol{\xi},0)p(\boldsymbol{\xi})\,\mathrm{d}\xi_\infty\,\ldots\,\mathrm{d}\xi_1\,\mathrm{d}\xi_0.\end{aligned} \tag{4.50}$$

In the previous section, it was established that the mean of an expanded variable $x(\boldsymbol{\xi})$ is $\phi_0^2 X_0$ and that its variance is $\sum_{i=1}^{\infty}\phi_i^2 X_i^2$, where X_i are the expansion coefficients. For the expanded dynamic system, the mean trajectory of each state variable $x_k(t,\boldsymbol{\xi})$ is similarly $\phi_0^2 X_{k0}(t)$ and its variance is $\sum_{i=1}^{\infty}\phi_i^2 X_{ki}^2(t)$, which can also be written as

$$\mathbb{E}[\boldsymbol{x}(t,\boldsymbol{\xi})] = \underline{M}\boldsymbol{X}(t), \tag{4.51a}$$

$$\mathbb{E}[(\boldsymbol{x}(t,\boldsymbol{\xi}) - \mathbb{E}[\boldsymbol{x}(t,\boldsymbol{\xi})])^2] = \underline{V}\boldsymbol{X}^{\circ 2}(t), \tag{4.51b}$$

where

$$\underline{Z}^{\circ\eta} = \begin{bmatrix}\zeta_{11}^{\eta} & \zeta_{12}^{\eta} & \cdots \\ \zeta_{21}^{\eta} & \zeta_{22}^{\eta} & \cdots \\ \vdots & \vdots & \ddots\end{bmatrix}, \quad \text{given} \quad \underline{Z} = \begin{bmatrix}\zeta_{11} & \zeta_{12} & \cdots \\ \zeta_{21} & \zeta_{22} & \cdots \\ \vdots & \vdots & \ddots\end{bmatrix}, \tag{4.52}$$

is the Hadamard exponentiation [48] and

$$\underline{M} = \begin{bmatrix}\phi_0^2 & 0 & 0 & \ldots\end{bmatrix} \otimes \underline{I}_{N_{\boldsymbol{x}}}, \tag{4.53}$$

$$\underline{V} = \begin{bmatrix}0 & \phi_1^2 & \phi_2^2 & \ldots\end{bmatrix} \otimes \underline{I}_{N_{\boldsymbol{x}}}. \tag{4.54}$$

It is important to recall that even though the ideal expansion has infinitely many terms, in practice it is necessary to use a truncation up to terms of $N_{\text{PCE}}^{\text{th}}$ order, meaning all terms

$$i \in \mathcal{I},\ \mathcal{I} = \{i \mid ||\boldsymbol{\alpha}_k|| \leq N_{\text{PCE}}, i \in \mathbb{N}\}, \tag{4.55}$$

depending on the desired accuracy. One will also have to consider only a finite number of N_p uncertainties, thus restricting the number of random variables in $\boldsymbol{\xi}$. The number of states in the augmented system will then be

$$N_{\boldsymbol{X}} = N_{\boldsymbol{x}} N_\phi = N_{\boldsymbol{x}} \frac{(N_p + N_{\text{PCE}})!}{N_p! N_{\text{PCE}}!}. \tag{4.56}$$

4.3 Karhunen-Loève Expansion

The random variables considered so far have all been stationary random variables, meaning that their values remain the same irrespective of time and space. In some real systems however, there may be non stationary uncertainties. Such uncertainties can be expressed on the form

$$w = \bar{w} + w_\sigma \alpha(\boldsymbol{\tau}, \boldsymbol{\xi}), \tag{4.57}$$

where $\bar{w}$ is the mean of the random process, w_σ is its standard deviation and $\alpha(\boldsymbol{\tau}, \boldsymbol{\xi})$ is a time- and/or space $\boldsymbol{\tau}$ variant random process with zero mean and unit variance. To generate a realisation for such a process, one would need a random variable for each instance in time or each point in space. However, it is also possible to describe the random process $\alpha(\boldsymbol{\tau}, \boldsymbol{\xi})$ by the Karhunen-Loève expansion

$$\alpha(\boldsymbol{\tau}, \boldsymbol{\xi}) = \sum_{i=0}^{\infty} \sqrt{\lambda_i} f_i(\boldsymbol{\tau}) \xi_i. \tag{4.58}$$

In (4.58), λ_k are the eigenvalues of the covariance function $C(\boldsymbol{\tau}_1, \boldsymbol{\tau}_2)$ of $\alpha(\boldsymbol{\tau}, \boldsymbol{\xi})$ and $f_k(\boldsymbol{\tau})$ are the corresponding eigenfunctions. The eigenvalues and eigenfunctions are the solutions of the Fredholm integral equation

$$\int_{\mathcal{D}_{\boldsymbol{\tau}}} C(\boldsymbol{\tau}_1, \boldsymbol{\tau}_2) f_n(\boldsymbol{\tau}_1) \, \mathrm{d}\boldsymbol{\tau}_1 = \lambda_n f_n(\boldsymbol{\tau}_2), \tag{4.59}$$

where $\mathcal{D}_{\boldsymbol{\tau}}$ is the domain of $\boldsymbol{\tau}$ [8], [9]. The eigenfunctions are orthogonal to each other with respect to $w(\boldsymbol{\tau}) = 1$, meaning that

$$\int f_n(\boldsymbol{\tau}) f_m(\boldsymbol{\tau}) \, \mathrm{d}\boldsymbol{\tau} = \delta_{nm}. \tag{4.60}$$

The infinite valued eigenvalue problem in (4.59) has no analytical solution in the general case. The numerical methodology used to solve it in this project is covered in Chapter 5.

As with the PCE, one may truncate the sum at a point N_{KLE}. The remaining error is then

$$\epsilon_{N_{\text{KLE}}} = \sum_{n=N_{\text{KLE}}+1}^{\infty} \sqrt{\lambda_n} f_n(\boldsymbol{\tau}) \xi_n, \tag{4.61}$$

and a property of the KLE is that the mean square error resulting from this truncation is minimised [8], allowing random processes to be described with arbitrary

accuracy. This representation of the non-stationary random process by a finite number of stationary random variables can be used together with the PCE approach presented in the earlier Section 4.2.2 [9].

As mentioned, the KLE is useful for describing time variant or spatially variant processes with known covariance [9]. A limitation of the KLE is however that white noise cannot be uniquely described by it. For a white noise process the covariance function is $C(\boldsymbol{\tau}_1, \boldsymbol{\tau}_2) = \delta_{\boldsymbol{\tau}_1\boldsymbol{\tau}_2}$, thus (4.59) becomes

$$\int_{\mathcal{D}_\tau} C(\boldsymbol{\tau}_1, \boldsymbol{\tau}_2) f_n(\boldsymbol{\tau}_1)\,\mathrm{d}\boldsymbol{\tau}_1 = \int_{\mathcal{D}_\tau} \delta_{\boldsymbol{\tau}_1\boldsymbol{\tau}_2} f_n(\boldsymbol{\tau}_1)\,\mathrm{d}\boldsymbol{\tau}_1 = f_n(\boldsymbol{\tau}_1) = \lambda_n f_n(\boldsymbol{\tau}_2), \tag{4.62}$$

which has no unique solution. Coloured random process however, can be uniquely defined by this expansion.

4.4 Stochastic Optimal Control Using PCE

When controlling systems towards some form of target state, state feedback is a common approach [37]. Here, the input signal becomes state dependent on the form $\boldsymbol{u}(t) = \underline{K}\boldsymbol{x}(t)$, where $\underline{K}$ is the constant control gain matrix chosen to fulfil the objective

$$\begin{aligned} \underline{K} &= \arg\min_{\underline{K}} \underbrace{\int_0^\infty \boldsymbol{x}^\intercal(t)\underline{Q}\boldsymbol{x}(t) + \boldsymbol{u}^\intercal(t)\underline{R}\boldsymbol{u}(t)\,\mathrm{d}t}_{\text{Cost functional}}, \\ \text{such that } \dot{\boldsymbol{x}}(t) &= f(t, \boldsymbol{x}(t), \boldsymbol{u}(t)), \\ \boldsymbol{x}(0) &= \boldsymbol{x}_0, \end{aligned} \tag{4.63}$$

using the weighting matrices $\underline{Q}$ and $\underline{R}$. The resulting controller is called a least quadratic regulator (LQR).

A so called stochastic LQR (SLQR) can be synthesised based on the expected cost, giving the optimisation problem

$$\begin{aligned} \underline{K} &= \arg\min_{\underline{K}} \underbrace{\mathbb{E}\left[\int_0^\infty \boldsymbol{x}^\intercal(t,\boldsymbol{\xi})\underline{Q}\boldsymbol{x}(t,\boldsymbol{\xi}) + \boldsymbol{u}^\intercal(t)\underline{R}\boldsymbol{u}(t)\,\mathrm{d}t\right]}_{\text{Cost functional}}, \\ \text{such that } \dot{\boldsymbol{x}}(t,\boldsymbol{\xi}) &= f(t, \boldsymbol{x}(t,\boldsymbol{\xi}), \boldsymbol{u}(t)), \\ \boldsymbol{x}(0,\boldsymbol{\xi}) &= \boldsymbol{x}_0(\boldsymbol{\xi}). \end{aligned} \tag{4.64}$$

Fisher [9], [49] proposes four main control schemes, two of which use a deterministic feedback gain based on the stochastic dynamics of the system and the other two use a stochastic feedback gain. The first proposition is state feedback with the augmented state vector $\boldsymbol{X}(t)$ using a constant gain $\underline{K}$ as

$$\boldsymbol{U}(t) = \underline{K}\boldsymbol{X}(t). \tag{4.65}$$

The second proposition also uses a constant gain matrix $\underline{K}$, however the state vector used for feedback is the original state vector $\boldsymbol{x}(t,\boldsymbol{\xi})$,

$$\boldsymbol{u}(t,\boldsymbol{\xi}) = \underline{K}\boldsymbol{x}(t,\boldsymbol{\xi}). \tag{4.66}$$

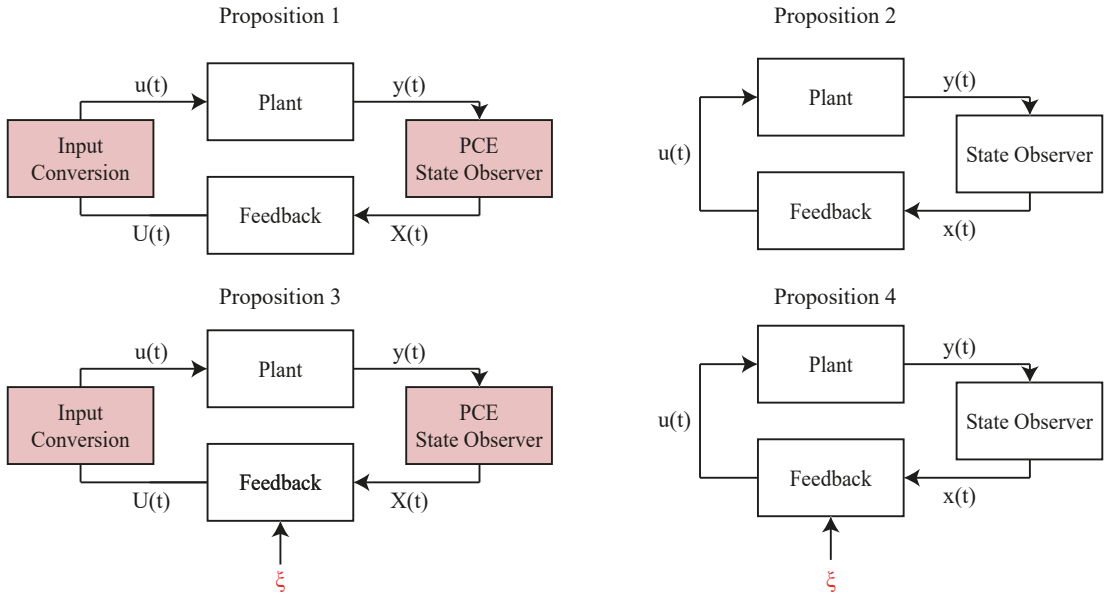

Figure 4.6: Illustrations of control loops for each of the four propositions.

The last two propositions are similar in their feedback structures to the previous two, however the gain matrices are dependent on the random variable $\boldsymbol{\xi}$, resulting in the control structures

$$\boldsymbol{U}(t) = \underline{K}(\boldsymbol{\xi})\boldsymbol{X}(t), \tag{4.67}$$

$$\boldsymbol{u}(t, \boldsymbol{\xi}) = \underline{K}(\boldsymbol{\xi})\boldsymbol{x}(t, \boldsymbol{\xi}). \tag{4.68}$$

Simple control loops for all four of these propositions have been illustrated in Figure 4.6. The control law in (4.66) is the most practical to implement. Once the control gain matrix $\underline{K}$ has been computed, the implementation of the controller is no different to a regular LQR since the control law takes the same form, as can also be seen in the corresponding illustration. In order to use either (4.65) or (4.67), one would need to create some type of observer to estimate the augmented state $\boldsymbol{X}(t)$. Further, the control laws (4.67) and (4.68) would also require estimation of the random variable $\boldsymbol{\xi}$ by some means. These open challenges are marked in red in Figure 4.6.

The constant gain matrix in (4.66) can be lifted into the PC expansion by

$$\boldsymbol{U}(t) = (\underline{K} \otimes \underline{I}_{N_\phi})\boldsymbol{X}(t). \tag{4.69}$$

Since the resulting system

$$\dot{\boldsymbol{X}}(t) = \underline{A}_{\text{PCE}}\boldsymbol{X}(t) + \underline{B}_{\text{PCE,s}}(\underline{K} \otimes \underline{I}_{N_\phi})\boldsymbol{X}(t) \tag{4.70}$$

is again deterministic, one can compute the control gain for it by the optimisation

$$\begin{aligned} \underline{K} = \arg\min_{\underline{K}} & \underbrace{\int_0^\infty \boldsymbol{X}^\intercal(t)\underline{Q}_{\text{PCE}}\boldsymbol{X}(t) + \boldsymbol{U}^\intercal(t)\underline{R}_{\text{PCE}}\boldsymbol{U}(t)\,\mathrm{d}t}_{\text{Cost functional}}, \\ \text{such that } & \dot{\boldsymbol{X}}(t) = f_{\text{PCE}}(t, \boldsymbol{X}(t), \boldsymbol{U}(t)), \\ & \boldsymbol{X}(0) = \boldsymbol{X}_0, \end{aligned} \tag{4.71}$$

which is similar to the already familiar LQR problem in (4.63) and minimised by solving the Riccati equation

$$\begin{aligned}&\underline{A}_{\text{PCE}}^{\intercal}\underline{P} + \underline{P}\underline{A}_{\text{PCE}} + \underline{P}\underline{B}_{\text{PCE,s}}(\underline{K} \otimes \underline{I}_{N_\phi}) + (\underline{K}^{\intercal} \otimes \underline{I}_{N_\phi})\underline{B}_{\text{PCE,s}}^{\intercal}\underline{P} \\ &+ \underline{Q} + (\underline{K}^{\intercal} \otimes \underline{I}_{N_\phi})\underline{R}(\underline{K} \otimes \underline{I}_{N_\phi}) = 0.\end{aligned} \tag{4.72}$$

The optimality of this solution is subject to $\underline{P} = \underline{P}^{\intercal}$, with $\underline{P}$ being positive definite, and whether or not the feasibility condition

$$\underline{A}^{\intercal}\underline{P} + \underline{P}\underline{A} + (\underline{K}^{\intercal} \otimes \underline{I}_{N_\phi})\underline{B}^{\intercal}\underline{P} + \underline{P}\underline{B}(\underline{K} \otimes \underline{I}_{N_\phi}) < 0 \tag{4.73}$$

is fulfilled [9], [37].

Since the first expansion term of each state variable $x_k(t, \boldsymbol{\xi})$ or input signal $u_k(t, \boldsymbol{\xi})$ is related to its mean and the sum of the squares of the rest are related to the variance, one can choose the weighting matrices $\underline{Q}_{\text{PCE}}$ and $\underline{R}_{\text{PCE}}$ to apply different penalties to the expected state trajectory and the variance of the state trajectory.

4.5 Sensitivity Analysis

In practice, it is only feasible to consider a finite amount of N_p uncertainties $\{\xi_i\}_{i=1}^{N_p}$, and it is also of benefit computationally to consider as few uncertainties as possible. As such, a sensitivity analysis may be relevant to inspect how drastically the output of a model changes as a result of a parameter value changing. These results are useful to learn which uncertainties are more critical to consider when looking at a model [50].

In general, Sudret [50] suggests looking at the so called Sobol' indices of a function as a means of sensitivity analysis. For a system

$$y = f(\boldsymbol{\theta}), \tag{4.74}$$

where $\boldsymbol{\theta}$ is a vector of N parameters. For this example, the output y is assumed scalar. The system can then be rewritten by so called Sobol' decomposition

$$f(\boldsymbol{\theta}) = f_0 + \sum_{k=1}^{\infty} f_k(\theta_k) + \sum_{1 \le k < l \le \infty} f_{kl}(\theta_k, \theta_l) + \ldots + f_{1,2,\ldots,N}(\theta_1, \ldots, \theta_N). \tag{4.75}$$

Here, the first term, f_0 is the mean and the first sum is the variance contribution dependent on only one parameter θ_k where as the following terms are the variance contributions from all possible combinations of two different θ_k and the follwing terms are the variance contributions from all possible combinations of three or more θ_k.

This decomposition appears very similar to the PCE, and in fact, as Sudret [50] goes on to show, the Sobol' decomposition is indeed the same as the PCE. Given the PCE of x as presented earlier in (4.23), the Sobol' index SU_i corresponding to a given parameter θ_i, or random variable ξ_i with the PCE notation, is simply the sum

of all $\phi_k^2 X_k^2$ relating to the corresponding expansion terms of order one or higher which are dependent on ξ_i. In other words the term relating to ξ_i from the first sum in (4.75). That is all terms where the polynomials corresponding to all ξ_j where $j \neq i$ are of order zero, divided by the total variance [50],

$$SU_k = \frac{\sum_{j \in \mathcal{J}} \phi_j^2 X_j^2}{\sum_{i=1}^{\infty} \phi_i^2 X_i^2},\ \mathcal{J}\left\{ j \geq 1 \mid \frac{\partial \phi_j(\boldsymbol{\xi})}{\partial \xi_k} \neq 0 \wedge \frac{\partial}{\partial \xi_l} \phi_j(\boldsymbol{\xi}) = 0\ \forall\, l \neq k \right\}. \tag{4.76}$$

A *total sensitivity* SU_i^{T} can also be computed, this is the sum of all $\phi_k^2 X_k^2$ corresponding to terms where the polynomial of ξ_i is at least of order one, i.e. all terms from (4.75) which contain ξ_i, divided by the total variance [50],

$$SU_k^{\mathrm{T}} = \frac{\sum_{j \in \mathcal{J}^T} \phi_j^2 X_j^2}{\sum_{i=1}^{\infty} \phi_i^2 X_i^2},\ \mathcal{J}^T\left\{ j \geq 1 \mid \frac{\partial \phi_j(\boldsymbol{\xi})}{\partial \xi_k} \neq 0 \right\}. \tag{4.77}$$

This can also be clarified by going back to the expansion example of Table 4.4, for which the first order sensitivity with respect to ξ_1 is

$$SU_1 = \frac{\phi_1^2 X_1^2 + \phi_3^2 X_3^2 + \phi_6^2 X_6^2}{\sum_{i=1}^{\infty} \phi_i^2 X_i^2}, \tag{4.78}$$

and the total order sensitivity with respect to the same variable is

$$SU_1^T = \frac{\phi_1^2 X_1^2 + \phi_3^2 X_3^2 + \phi_4^2 X_4^2 + \phi_6^2 X_6^2 + \phi_7^2 X_7^2 + \phi_8^2 X_8^2}{\sum_{i=1}^{\infty} \phi_i^2 X_i^2}. \tag{4.79}$$

5

Methodology

The aim of this project was to investigate the possibility of characterising uncertainties based on measured vehicle data. The execution of this investigation using the theoretical ideas from Chapters 2, 3 and 4 is presented in this chapter. The first step was to generate measured data. In order to conduct the investigation in a controlled manner, the measured data was generated in simulation, where the exact parameters could all be controlled, preventing unexpected effects to affect the data. The modelling of the vehicle and computation of its output statistics are covered in Section 5.1. For clarity, the model described here is referred to as the *real* or *baseline* model.

This section is followed by Section 5.2, where the methodology used to compute the PCE and KLE of the linear vehicle model numerically is presented. The PCE of the linear vehicle model was used as the base for the identification of the distribution parameters of the uncertainties. For this, the approach presented in Section 5.3 was used. Given that the ultimate aim of the stochastic formulation of systems is to use that information for control design, a PCE-based control approach was also tested. This is covered in Section 5.4.

5.1 Stochastic Vehicle Model and Data Synthesis

To create a synthetic reality, a vehicle was modelled based on the theory in Chapter 2 with four stationary uncertainties and one time variant disturbance. Three of the four stationary uncertainties were related to tyre- and vehicle parameters. The friction $\mu(\boldsymbol{\xi})$ between the tyre and road, the mass of the load $m_{\text{load}}(\boldsymbol{\xi})$ and the position of the CoG position relative to front axle $l_{\text{f}}(\boldsymbol{\xi})$. A time variant side wind force

$$F_{\text{w}}(t, \boldsymbol{\xi}) = \bar{F}_{\text{w}}(\boldsymbol{\xi}) + F_{\text{w},\sigma} F_{\text{w},\alpha}(t, \boldsymbol{\xi}) \tag{5.1}$$

was also included, with a stationary uncertain mean $\bar{F}_{\text{w}}(\boldsymbol{\xi})$, a constant standard deviation $F_{\text{w},\sigma}$, and a time variant zero mean, unit variance coloured Gaussian process $F_{\text{w},\alpha}(t, \boldsymbol{\xi})$ with the covariance function

$$C(t_1, t_2) = e^{\frac{-(t_1 - t_2)^2}{T_c^2}}, \tag{5.2}$$

where T_c is a time constant for the covariance function, in this case $T_c = 2\,s$. Associated with the side wind, a yaw moment $M_{\text{w}}(t, \boldsymbol{\xi}) = M_c F_{\text{w}}(t, \boldsymbol{\xi})$ was also modelled,

where the factor M_c is a constant describing the relation between the lateral force and the yaw moment.

In addition to the side wind, the state space model from (2.22) was also extended with two new state variables related to the lateral position of the vehicle, as the specific example studied in this thesis was related to a lane keeping assistance system. This extension of the system changed the equations to

$$\alpha_{\mathrm{f}} = \delta - \tan^{-1}\left(\frac{v_c \sin(\beta) + l_{\mathrm{f}}\dot{\psi}}{v_c \cos(\beta)}\right), \tag{5.3a}$$

$$\alpha_{\mathrm{r}} = -\tan^{-1}\left(\frac{v_c \sin(\beta) - l_{\mathrm{r}}\dot{\psi}}{v_c \cos(\beta)}\right), \tag{5.3b}$$

$$F_{\mathrm{f},z} = mg\frac{l_{\mathrm{r}}}{L}, \tag{5.3c}$$

$$F_{\mathrm{r},z} = mg\frac{l_{\mathrm{f}}}{L}, \tag{5.3d}$$

$$\dot{\psi} = \dot{\psi}, \tag{5.3e}$$

$$I_z\ddot{\psi} = l_{\mathrm{f}}F_{\mathrm{f},y}\cos(\delta) - F_{\mathrm{r},y}l_{\mathrm{r}} + M_{\mathrm{w}}(t,\boldsymbol{\xi}), \tag{5.3f}$$

$$\dot{\beta} = \frac{1}{mv_c}\left(F_{\mathrm{f},y}\cos(\delta) + F_{\mathrm{r},y} + F_{\mathrm{w}}(t,\boldsymbol{\xi})\right)\cos(\beta) - \dot{\psi}, \tag{5.3g}$$

$$\dot{y}_{\mathrm{pos}} = \sin(\psi)v_c, \tag{5.3h}$$

and the linear model (using the small angle approximation for ψ) to

$$\underbrace{\begin{bmatrix}\dot{\psi}\\ \ddot{\psi}\\ \dot{\beta}\\ \dot{y}_{\mathrm{pos}}\end{bmatrix}}_{\dot{\boldsymbol{x}}(t,\boldsymbol{\xi})} = \underbrace{\begin{bmatrix}0 & 1 & 0 & 0\\ 0 & -\frac{c_{\mathrm{f}}l_{\mathrm{f}}^2+c_{\mathrm{r}}l_{\mathrm{r}}^2}{I_z v_c} & \frac{c_{\mathrm{r}}l_{\mathrm{r}}-c_{\mathrm{f}}l_{\mathrm{f}}}{I_z} & 0\\ 0 & \frac{c_{\mathrm{r}}l_{\mathrm{r}}-c_{\mathrm{f}}l_{\mathrm{f}}}{mv_c^2} - 1 & -\frac{c_{\mathrm{f}}+c_{\mathrm{f}}}{mv_c} & 0\\ v_c & 0 & 0 & 0\end{bmatrix}}_{\underline{A}(\boldsymbol{\xi})} \underbrace{\begin{bmatrix}\psi\\ \dot{\psi}\\ \beta\\ y_{\mathrm{pos}}\end{bmatrix}}_{\boldsymbol{x}(t,\boldsymbol{\xi})} + \underbrace{\begin{bmatrix}0\\ \frac{l_{\mathrm{f}}c_{\mathrm{f}}}{I_z}\\ \frac{c_{\mathrm{f}}}{mv_c}\\ 0\end{bmatrix}}_{\underline{B}(\boldsymbol{\xi})} \underbrace{\delta}_{\boldsymbol{u}} + \underbrace{\begin{bmatrix}0\\ \frac{M_{\mathrm{w}}(t,\boldsymbol{\xi})}{I_z}\\ \frac{F_{\mathrm{w}}(t,\boldsymbol{\xi})}{mv_c}\\ 0\end{bmatrix}}_{\underline{W}(t,\boldsymbol{\xi})}. \tag{5.4}$$

The blue portions represent the added states and the red portions the addition of the wind.

A complete list of the vehicle parameters and the values used is presented in Table 5.1, with the tyre parameters used presented in Table 5.2. The values of the uncertain parameters μ, m_{load}, and l_{f} in a particular realisation influence the values of other parameters. These dependencies are also displayed in Table 5.1. The tyre parameters used were chosen such that the tyre model would match the *Dry Tarmac* example from [23] when $\mu(\boldsymbol{\xi}) = 1$.

Measured data was synthesised using both the linear and non-linear vehicle models (5.4) and (5.3) using the sequential Monte Carlo method, as the implementation of the PCE available at the time did not allow expansion of non-linear systems. The input signal used was a sinusoidal steering input with an amplitude of

Table 5.1: The vehicle parameters used.

Parameter	Description	Unit	Value
	Vehicle Parameters		
m_{base}	Mass of the vehicle (without load)	kg	1784
m_{load}	Mass of load	kg	$\mathcal{N}(100, 30)$
m	Total vehicle mass	kg	$m_{\text{base}} + m_{\text{load}}$
J_0	Specific moment of inertia ($I_z = m_{tot} J_0$)	m^2	0.84
l_{f}	Distance between CoG and front axle	m	$\mathcal{N}(1.55, 0.2)$
L	Distance between front and rear axle	m	2.85
l_{r}	Distance between CoG and rear axle	m	$L - l_f$
$c_{S\text{f}}$	Cornering stiffness at the front	-	10.6
$c_{S\text{r}}$	Cornering stiffness at the rear	-	30.4
μ	Frictional coefficient	-	$\mathcal{N}(1, 0.2)$
v_c	Constant speed	m/s	$\frac{70}{3.6}$
M_c	Yaw moment factor	m	-1.2
	Environmental Parameters		
g	Acceleration due to gravity	m/s^2	9.81
$\bar{F}_{\text{w}}$	Side wind mean	N	$\mathcal{U}(-400, 400)$
$C(t_1, t_2)$	Side wind covariance function	-	$e^{\frac{-(t_1-t_2)^2}{2^2}}$

Table 5.2: Tyre parameters used for the vehicle model.

Tyre	B	C	D	E
Front Tyre	$c_{S\text{f}}$	1.9	μ	0.97
Rear Tyre	$c_{S\text{r}}$	1.9	μ	0.97

$\delta_{\max} = 5^\circ = \frac{1}{36}\pi$ rad and a period of 4 s,

$$\boldsymbol{u}(t) = \delta_{\max} \cos\left(\frac{\pi}{2} t\right), \tag{5.5}$$

which corresponds to driving a slalom, ensuring that all state variables of the system are affected.

For each simulation run, a particular realisation of the car was simulated with the input signal in (5.5) from the initial state $\boldsymbol{x}_0 = \mathbf{0}$, over the time span $t_0 = 0$ s to $t_f = 10$ s with a uniform time grid where each grid point was separated by $\Delta t = 0.001$ s. To solve the differential equations for this time grid the Dormand-Prince Runge-Kutta method was used through the MATLAB function `ode45` [51]. A data set was formed by simulating 2000 samples, as the statistics were observed to have converged to a satisfying degree at that number of samples.

It was assumed that each of the state variables could be measured, with the level of noise differing in each of a total of eleven generated data sets. For each signal $s(t)$,

Table 5.3: The value of the noise intensity parameter A for the different data sets.

Data set	1	2	3	4	5	6	7	8	9	10	11
A	0	0.01	0.02	0.03	0.04	0.05	0.06	0.07	0.08	0.09	0.1

the noise was added such that the corrupted signal at each time instance t_k was

$$s_c(t_k) = s(t_k) + A|s|_{\max}\zeta_k, \tag{5.6}$$

where all $\zeta_k \sim \mathcal{N}(0,1)$ and $|s|_{\max} = \max|s(t)|$ was used to scale the noise relative to each individual signal. For each of the eleven data sets, the values for A are presented in Table 5.3. In addition to these eleven data sets, one additional one was created without noise, but using an inverted input signal

$$\boldsymbol{u}(t) = -\delta_{\max}\cos(\frac{\pi}{2}t), \tag{5.7}$$

to later test the input sensitivity of the estimation.

5.2 Numerical KLE and PCE

In order to expand the stochastic linear vehicle model using the PC, it was necessary to first rewrite the uncertainties as functions of stationary variables with standard probability distributions. The four stationary uncertainties were modelled as

$$\mu(\boldsymbol{\xi}) = 1 + 0.2\xi_1, \qquad \xi_1 \sim \mathcal{N}(0,1), \tag{5.8}$$
$$m_{\text{load}}(\boldsymbol{\xi}) = 100 + 30\xi_2, \qquad \xi_2 \sim \mathcal{N}(0,1), \tag{5.9}$$
$$l_{\text{f}}(\boldsymbol{\xi}) = 1.55 + 0.2\xi_3, \qquad \xi_3 \sim \mathcal{N}(0,1), \tag{5.10}$$
$$\bar{F}_{\text{w}}(\boldsymbol{\xi}) = \frac{400 + (-400) + \xi_4(400 - (-400))}{2}, \qquad \xi_4 \sim \mathcal{U}(-1,1), \tag{5.11}$$

and $F_{\text{w}}(t,\boldsymbol{\xi})$ was modelled using the KLE (4.58), for which all random variables follow the standard normal distribution. With the KLE, the disturbance matrix $\underline{W}(t,\boldsymbol{\xi})$ can be split into $\underline{W}(\boldsymbol{\xi})\boldsymbol{f}(t)$, where $\boldsymbol{f}(t)$ are the eigenfunctions in the KLE. It was then possible to expand the linear state space system by PCE, using the same method for $\underline{W}(\boldsymbol{\xi})$ as for $\underline{B}$ in (4.44b).

Both the Galerkin projection of the PC expanded system matrices (4.44a), (4.44b), (4.44c) and/or (4.45) and the Fredholm equation (4.59) are integral problems without a straightforward analytical solution. For this reason, they needed to be approximated. Numerical computation of integrals is often done by approximating them as sums

$$\int_a^b f(x)\,\mathrm{d}x \approx \sum_{k=0}^{N} w_k f(x_k),\ x_k \in [a,b]\,\forall k = 0,\,1\,\ldots,\,N, \tag{5.12}$$

where w_k is some weight such as a step length. A question that naturally arises is how to choose the points x_k at which the function is evaluated. The scheme used in this project was the Gauss-Legendre quadrature (GLQ), as described by Schmidt [52], which can be applied to both one- and multidimensional integrals.

Using the GLQ involves choosing N_{GLQ} evaluation points to deliver the optimal approximation when integrating polynomials. In fact, using this method for polynomials of degrees up to $2N_{\text{GLQ}}-1$ ensures an exact solution. For any general (non-polynomial) function $f(x)$, this ensures that approximation error of the quadrature is at most the same as the error one would get from approximating $f(x)$ as a polynomial of degree $2N_{\text{GLQ}}-1$. This makes it possible to approximate the integral over the normal interval $[-1,\, 1]$ of a sufficiently smooth function $f(x)$ as

$$\int_{-1}^{1} f(x)\,dx \approx \sum_{k=0}^{N-1} f(x_k^*)w_k = \boldsymbol{f}^{\intercal}\boldsymbol{w},\ \boldsymbol{f},\boldsymbol{w} \in \mathbb{R}^N. \tag{5.13}$$

Each point x_k^* is associated with a weight w_k. The pair (x_k^*, w_k) will be referred to as a Gauss point.

The evaluation points x_k^* are the zeros of the $N_{\text{GLQ}}^{\text{th}}$ order Legendre polynomial $L_n(x)$. These zeros are in turn also approximated numerically using a Newton-Raphson method. The weights w_k come from the matrix equation

$$\underbrace{\begin{bmatrix} x_1^{*0} & \dots & x_{N\text{GLQ}}^{*\,0} \\ \vdots & \ddots & \vdots \\ x_1^{*N_{\text{GLQ}}-1} & \dots & x_{N\text{GLQ}}^{*\,N_{\text{GLQ}}-1} \end{bmatrix}}_{\text{Vandermonde Matrix}} \begin{bmatrix} w_1 \\ \vdots \\ w_N \end{bmatrix} = \begin{bmatrix} \frac{1+(-1)^0}{0+1} \\ \vdots \\ \frac{1+(-1)^{N_{\text{GLQ}}-1}}{(N-1)+1} \end{bmatrix}. \tag{5.14}$$

A visual representation of Gauss points with $N_{\text{GLQ}} = 10$ is presented in Figure 5.1. Evidently, these points are not equidistantly spaced but since the Legendre polynomials are always either even or odd, their zeros (and thus the Gauss points) are spaced symmetrically around the origin.

The explanation provided thus far hinges on the integration interval $[-1,\, 1]$. For the arbitrary integration interval $[a, b]$, the evaluation points were mapped such that

$$x_k = \frac{b + a + x_k^*(b-a)}{2} \tag{5.15}$$

and the weights were kept the same. For multidimensional integrals, such as the Galerkin projection, a grid was formed over the integration space using the Gauss points in each dimension of the integration space.

The computation of the KLE hinged on solving for the eigenvalues and eigenfunctions using the Fredholm integral 4.59. For this, a so called *Nyström approximation* was used [53]. This method involves taking the Fredholm equation

$$\int_a^b C(\boldsymbol{\tau}_1, \boldsymbol{\tau}_2) f_n(\boldsymbol{\tau}_1)\,\mathrm{d}\boldsymbol{\tau}_1 = \lambda_n f_n(\boldsymbol{\tau}_2) \tag{5.16}$$

and approximating it as

$$\sum_{k=0}^{N_{\text{GLQ}}-1} C(t_k, t_2) w_k f_n(t_k) = \lambda_n f_n(t_2), \tag{5.17}$$

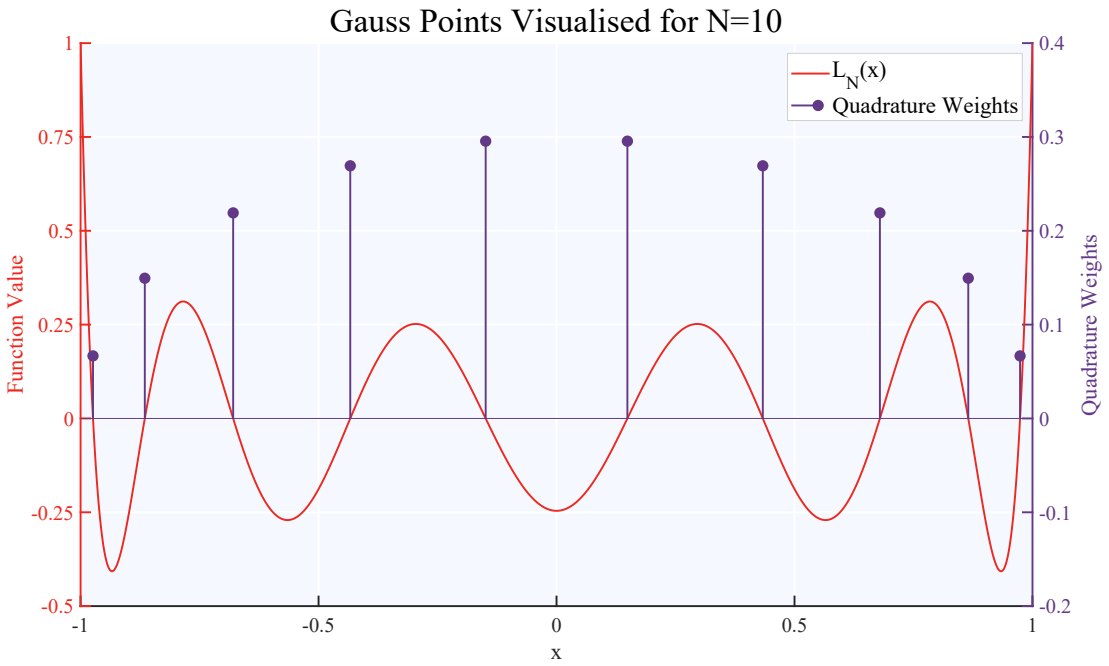

Figure 5.1: Visual representation of the Gauss points relative to the corresponding Legendre polynomial.

where the points (t_k, w_k) are Gauss points from the $N_{\text{GLQ}}^{\text{th}}$ order GLQ. Under the assumption that this approximation holds exactly for all $t_2 \in \{t_k\}_{k=0}^{N_{\text{GLQ}}-1}$, we can solve for λ_n and $f_n(t_k)$ by solving the matrix equation

$$\underline{C}(\boldsymbol{t}_{\text{GLQ}}, \boldsymbol{t}_{\text{GLQ}})\underline{W}_{\text{GLQ}}\underline{V}_f(\boldsymbol{t}_{\text{GLQ}}) = \boldsymbol{\lambda}\underline{V}_f(\boldsymbol{t}_{\text{GLQ}}). \tag{5.18}$$

where $\underline{C}$ is the covariance matrix stemming from the covariance function $C(t_1, t_2)$,

$$\underline{W} = \begin{bmatrix} w_0 & & \\ & \ddots & \\ & & w_{N_{\text{GLQ}}} \end{bmatrix},$$

and the n^{th} row and k^{th} column of $\underline{V}_f(\boldsymbol{t}_{\text{GLQ}})$ is $f_n(t_k)$. Given these matrices, the continuous $f_n(t)$ were approximated by

$$\underline{V}_f(t) \approx \underline{\Lambda}^{-1}\underline{V}_f(\boldsymbol{t}_{\text{GLQ}})^{\intercal}\underline{W}\underline{C}(\boldsymbol{t}_{\text{GLQ}}, t), \tag{5.19}$$

where $\underline{\Lambda}$ is a diagonal matrix with the eigenvalues λ_k in the diagonal, which gives

$$f_n(t) \approx \lambda_n^{-1} \sum_{k=0}^{N_\lambda - 1} C(t_k, t) w_k f_n(t_k). \tag{5.20}$$

By this approximation, only N_{GLQ} eigenvalues and eigenfunctions were computed, thus, the sum of (4.58) was reduced to

$$\sum_{i=0}^{N_{\text{GLQ}}-1} \sqrt{\lambda_i}\xi_i f_i(\boldsymbol{\tau}). \tag{5.21}$$

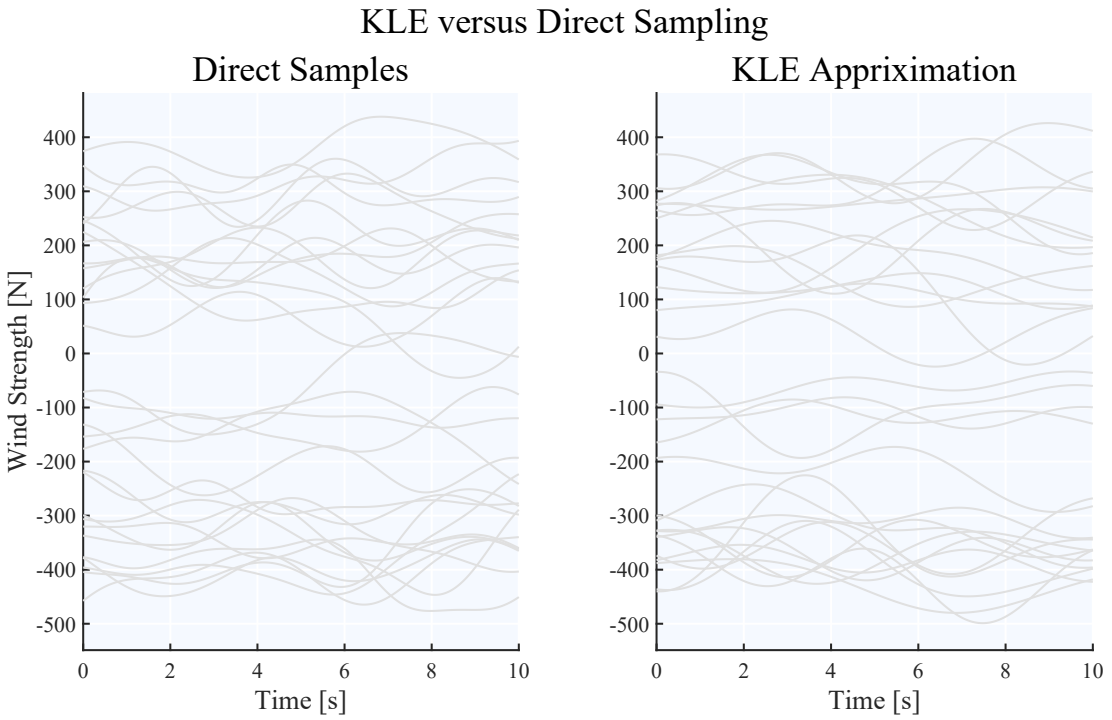

Figure 5.2: Comparison between realisations of the random process using direct sampling with MATLAB's mvnrnd and the KLE approximation with $N_{\mathrm{GLQ,KLE}} = 350$ and $p_c = 0.95$.

Recalling the fact that the number of PCE coefficients increase combinatorically with the amount of random variables, it is reasonable to reduce the number of eigenvalues as much as possible. From (4.58), one may observe that the greater eigenvalues will have the most influence on the value of the sum. Thus, in order to reduce the number of random variables further, the sum was truncated by only considering the N_c greatest and therefore most significant eigenvalues, where the smallest possible N_c was chosen such that

$$\sum_{i=0}^{N_c-1} \lambda_i \geq p_c \sum_{i=0}^{i_{\mathrm{GLQ}}-1} \lambda_i, \tag{5.22}$$

where p_c is the truncation factor.

As standard within this project, the PCE order $N_{\mathrm{PCE}} = 2$ was used together with the quadrature order $N_{\mathrm{GLQ,PCE}} = 4$. For the KLE, the quadrature order $N_{\mathrm{GLQ,KLE}} = 350$ with the truncation factor $p_c = 0.95$ was used. These KLE settings were chosen as the resulting approximation of the wind appeared sufficiently accurate as displayed in Figure 5.2, where 30 random realisations have been plotted using direct sampling using mvnrnd in MATLAB and the KLE approximation. The PCE settings were chosen as the simulation data showed sufficient agreement with the results of the Monte Carlo simulations, as seen in Figure 5.3.

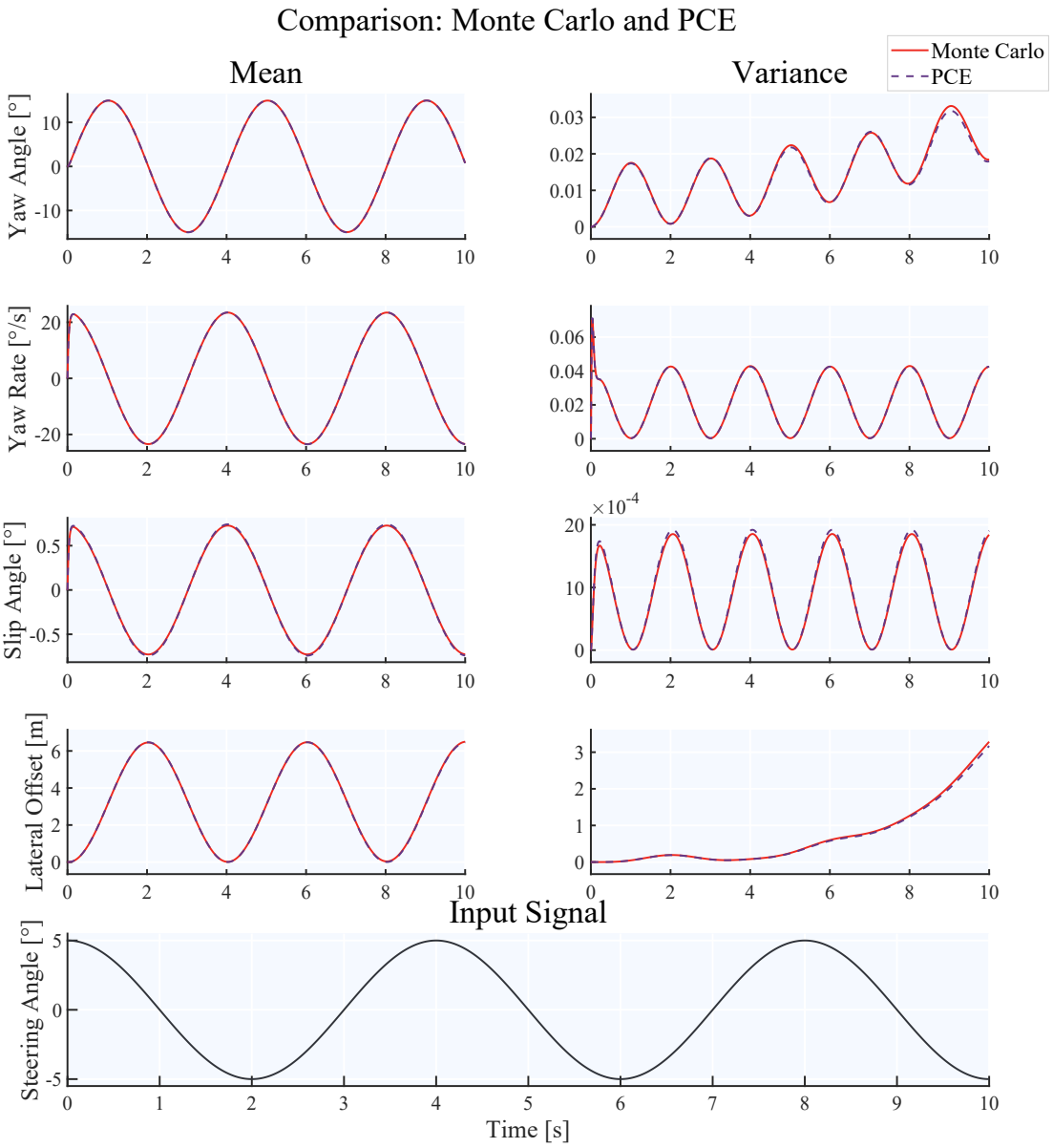

Figure 5.3: Comparison between simulation results using the Monte Carlo method and PCE.

5.3 Identification of Probability Distributions

With measured data generated, the next step was to use this data as a base in order to identify the distribution parameters of the uncertainties in the model. The model structure used for this is presented in Section 5.3.1. The estimation method and the different tests conducted are covered in Section 5.3.2.

5.3.1 Identification Model

For the identification, a linear single track model was used where the friction, CoG position, load and wind were all considered as stochastic parameters with unknown probability distribution parameters, but known or assumed distribution type. Before identifying any parameter values, an identifiability analysis was conducted to investigate whether or not all parameters could be identified. This was done in two different steps. First, the observability matrix approach described in Section 3.2 was used. In this part of the analysis, the time variant component of the wind was omitted, and only the mean wind strength was considered, giving the unknown parameter vector

$$\boldsymbol{\theta} = \begin{bmatrix} \mu & m_{\text{load}} & l_{\text{f}} & \bar{F}_{\text{w}} \end{bmatrix}^{\mathsf{T}}. \tag{5.23}$$

As per (3.12), the LST model state vector was extended with $\boldsymbol{\theta}$, which lead to a non-linear model, necessitating the usage of the non-linear observability matrix (3.9). For the evaluation of ORC, the constant input $\boldsymbol{u}(t) = \delta_{\max}$ was used. At evaluation, the ORC was not fulfilled, the rank of the matrix being 7 whereas full rank would have been 8. By removing each column individually and computing the rank of the matrix again, it was found that the identifiability of the parameter m_{load} could not be guaranteed.

Given that the input used did not exactly match the time variant input signal used in the data, and the fact that ORC when using the non-linear observability matrix is merely a sufficient but not necessary condition, the identifiability of m_{load} could not be definitively ruled out by this method. To further investigate, a sensitivity analysis of the sort described in Section 4.5 was used. For this, the PCE of the stochastic LST model with the known parameter values in Table 5.1 was used. In this sensitivity analysis, the time variant disturbance was also included. The sensitivity towards the disturbance was split into a sensitivity to the mean and a sensitivity against its time variant portion, which was computed by summing the sensitivities against all ξ_i from the KLE. The sensitivity analysis on this form is input specific, thus the input used was the same as in the testing data (5.5).

The first order sensitivity of every state variable of the LST model against every uncertainty has been plotted in Figure 5.4. From this sensitivity analysis, it was noted that the sensitivity against both the load and time variant portion of the side wind were low compared to the other parameters. Combined with the outcome of the identifiability analysis using the observability matrix, m_{load} was therefore considered unidentifiable. As a consequence of this, it was modelled as being a constant in the identification model, and its value was assumed to be measured through other means

than system identification. Additionally, as the sensitivity against the time variant portion of the wind was low, it was also modelled as being constantly zero. The wind was still modelled as stochastic through the mean $\bar{F}_{\mathrm{w}}$, but constant over time. The vehicle parameters of the identification model are listed in Table 5.4, with the parameters to identify being

$$\boldsymbol{\theta} = \begin{bmatrix} \theta_1 & \theta_2 & \theta_3 & \theta_4 & \theta_5 & \theta_6 \end{bmatrix}^{\intercal}, \tag{5.24}$$

and $\hat{m}_{\mathrm{load}}$ being an estimate of the mean of m_{load} estimated by some other means, as it has been indicated that it cannot be estimated through system idetnifcation.

Table 5.4: The vehicle parameters used in the identification model.

Parameter	Description	Unit	Value
	Vehicle Parameters		
m_{base}	Mass of the vehicle (without load)	kg	1784
m_{load}	Mass of load	kg	$\hat{m}_{\mathrm{load}}$
m	Total vehicle mass	kg	$m_{\mathrm{base}} + \hat{m}_{\mathrm{load}}$
J_0	Specific moment of inertia ($I_z = m_{tot} J_0$)	m^2	0.84
l_{f}	Distance between CoG and front axle	m	$\mathcal{N}(\theta_3, \theta_4)$
L	Distance between front and rear axle	m	2.85
l_{r}	Distance between CoG and rear axle	m	$L - l_f$
$c_{S\mathrm{f}}$	Cornering stiffness at the front	-	10.6
$c_{S\mathrm{r}}$	Cornering stiffness at the rear	-	30.4
μ	Frictional coefficient	-	$\mathcal{N}(\theta_1, \theta_2)$
v_c	Constant Speed	m/s	$\frac{70}{3.6}$
M_c	Yaw moment factor	m	-1.2
	Environmental Parameters		
g	Acceleration due to gravity	m/s^2	9.81
$\bar{F}_{\mathrm{w}}$	Side wind mean	N	$\mathcal{U}(\theta_5, \theta_6)$

5.3.2 Estimation

The main aim of this project was to investigate whether or not the distribution parameters of the uncertainties could be identified, and what role model simplifications would play. This was done by first testing a baseline where the model structure of the identified model matched that of the model used for data generation, by using linear single track models for both as illustrated in Figure 5.5. A differnt case was then set up, where data generated from a non-linear single track model was used instead to identify the same linear single track model as before. This case is illustrated in Figure 5.6.

Estimating the unknown parameters from the data was treated as a non-linear system identification problem, since the standard deviation from the PCE augmented state vector (4.51b) is a non-linear function of the state vector. From the testing data, the mean and standard deviation of the output trajectories had been

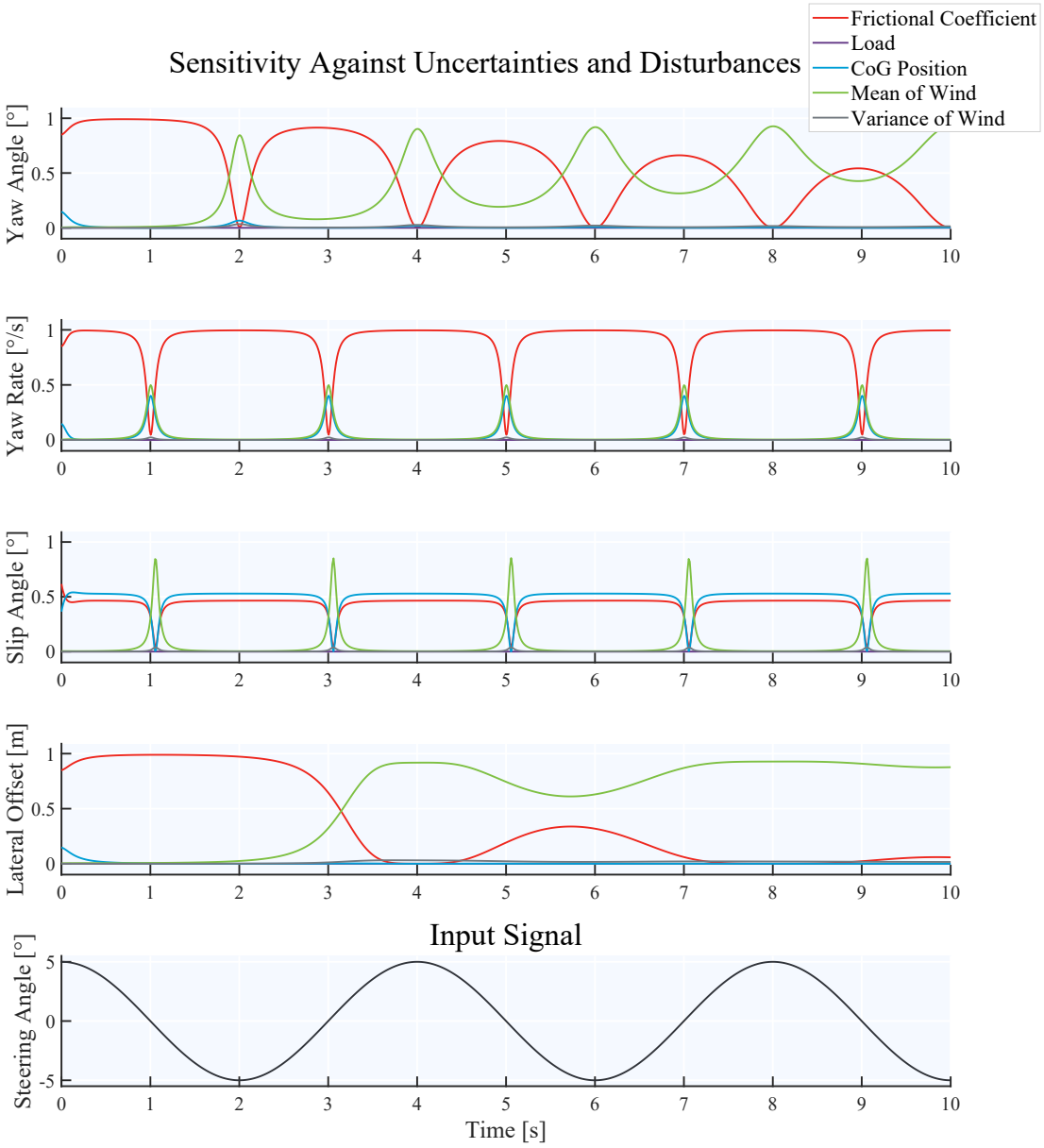

Figure 5.4: The first order sensitivity analysis of the system against all uncertainties.

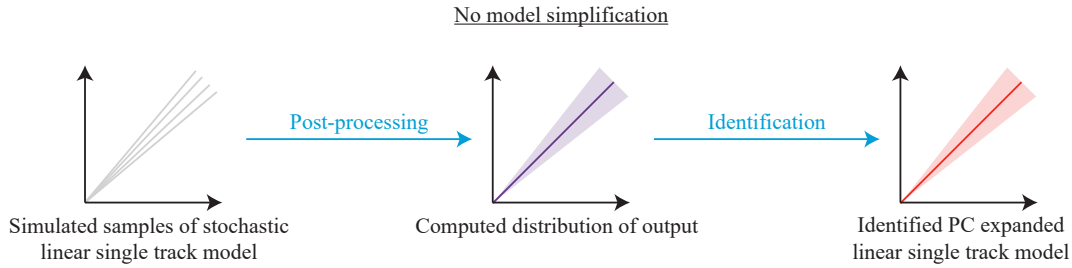

Figure 5.5: An illustration of the process of identifying a model without model simplification.

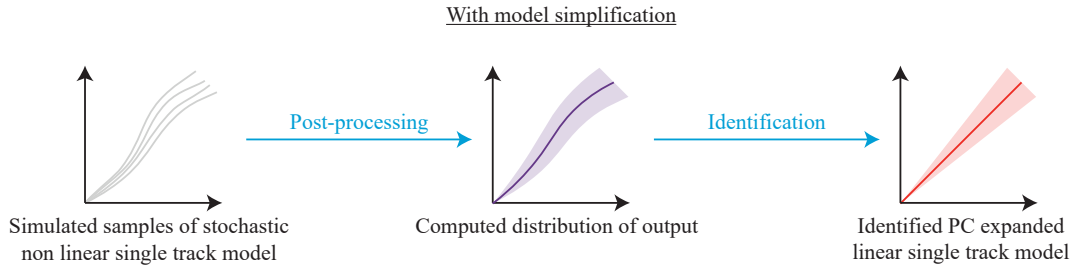

Figure 5.6: An illustration of the process of identifying a model with model simplification.

computed, and the approach used was to identify the unknown parameters of the identification model to match the measured mean and standard deviation as well as possible.

Three different cost functions were formulated, all on the general form

$$J(\hat{\boldsymbol{x}}) = \sum_{k=0}^{N} \boldsymbol{w}_k(\hat{\bar{\boldsymbol{x}}}_k - \bar{\boldsymbol{x}}_k^*)^2 + \boldsymbol{w}_k(\hat{\boldsymbol{x}}_{\sigma,k} - \boldsymbol{x}_{\sigma,k}^*)^2, \tag{5.25}$$

where $\hat{\bar{\boldsymbol{x}}}_k$ is the estimated mean and $\bar{\boldsymbol{x}}_k^*$ is the measured mean, both at sample k, $\hat{\boldsymbol{x}}_{\sigma,k}$ and $\boldsymbol{x}_{\sigma,k}^*$ are the estimated standard deviation and the measured standard deviation respectively. The weights $\boldsymbol{w}_k$ were changed for different cases. Note that in this case, the same weights are applied both to the mean- and standard deviation errors. When the estimation data from the linear model was used, $\boldsymbol{w}_k^{\text{STD}} = \begin{bmatrix} 1 & 1 & 1 & 1 \end{bmatrix}$, $\forall k = 1, \ldots, N$, were the weights used, as the identified model should be able to match the data exactly at every point of time assuming the correct parameter values can be found.

For the remaining two cost functions, two different weighting schemes were used. As was mentioned in Chapter 3, one reason to apply weights in the cost function could be to give more importance to samples which would be expected to have smaller error. When the measured data from the NLST model was used as the base for identification, there would be some error due to model simplifications in the LST identification model. The two models would be expected to behave more similarly to each other for small steering angles. Therefore, an input weighted cost function referred to as *INP* was used where each sample was weighted to depending on the absolute value of the steering angle by

$$\boldsymbol{w}_k^{\text{INP}} = e^{-|u(t_k)|} \begin{bmatrix} 1 & 1 & 1 & 1 \end{bmatrix}, \tag{5.26}$$

thus lending more importance to samples with small steering angles, where the model error would be expected to be smallest.

With the synthetic reality used within this project, perfect knowledge over it was held. It was thus possible to directly calculate the mismatch between the real LST and NLST models. For this, the Kullback-Leibler divergence [54] (KLD) was a natural choice. For two normal distributions $P \sim \mathcal{N}(\mu_p, \sigma_p)$ and $Q \sim \mathcal{N}(\mu_q, \sigma_q)$, the

KLD is given by

$$D_{\mathrm{KL}}(P||Q) = \frac{1}{2}\frac{\sigma_p}{\sigma_q} - 1 + \frac{(\mu_q - \mu_p)^2}{\sigma_q} + \log\left(\frac{\sigma_q}{\sigma_p}\right), \tag{5.27}$$

which was calculated between the approximated normal distributions of each state variable at each time step of both the LST and NLST models. The computed mismatch was then used to weight the cost function by

$$\begin{aligned} \boldsymbol{w}_k^{\mathrm{DST}} &= \begin{bmatrix} w_{k1} & w_{k2} & w_{k3} & w_{k4} \end{bmatrix}, \\ w_{ki} &= e^{-|D_{ki,KL}|}, \end{aligned} \tag{5.28}$$

where $D_{ki,\mathrm{KL}}$ is the KLD between the approximated normal distribution of output of the state variable $x_i(t_k, \boldsymbol{\xi})$ at time t_k using the LST and NLST models respectively.

In order to compare different estimates to each other, some metric was needed. As the objective was to estimate probability distributions, an appropriate type of metric was one that could quantify the difference between two probability distributions. The Kullback-Leibler divergence $D_{\mathrm{KL}}(P||Q)$ used to form the distance based cost function could not be used, as it is only defined in the case that $P(x) = 0$ for all x where $Q(x) = 0$, which cannot be guaranteed for two arbitrary uniform distributions. Instead the Wasserstein-metric was chosen. Its background is described in greater detail by [45], [55], [56]. For the purposes of this thesis, it is sufficient to present the definition of the p-Wasserstein distance between two one-dimensional probability distributions P and Q, which is defined by

$$W_p(P, Q) = \left(\int_0^1 |F^{-1}(q) - G^{-1}(q)|^p \, \mathrm{d}q\right)^{\frac{1}{p}}, \tag{5.29}$$

where $F^{-1}(q)$ and $G^{-1}(q)$ are the quantile functions of P and Q respectively. Within the scope of this project, only normal and uniform distributions are considered. The 2-Wasserstein distance between two normal distributions $\mathcal{N}(\mu_1, \sigma_1)$ and $\mathcal{N}(\mu_2, \sigma_2)$ is

$$W_2(P, Q) = \sqrt{|\mu_1 - \mu_2|_2^2 + \sigma_1 + \sigma 2_2 \sqrt{\sqrt{\sigma_2}\sigma_1\sqrt{\sigma_2}}}. \tag{5.30}$$

For two uniform distributions $P \sim \mathcal{U}(a_1, b_1)$ and $Q \sim \mathcal{U}(a_2, b_2)$ it is

$$\begin{aligned} W_2(P, Q) =& \sqrt{\frac{1}{3}(a_2 - a_1 + b_1 - b_2)^2} \\ &+ \frac{1}{2}(a_2 - a_1 + b_1 - b_2)(a_1 - a_2) + (a_1 - a_2)^2. \end{aligned} \tag{5.31}$$

One property of the Wasserstein-metric is that it inherits the dimension of the distributions it is comparing. For example for $P_1 \sim \mathcal{U}(0, 1)$ and $Q_1 \sim \mathcal{U}(-1, 2)$, $W_2(P_1, Q_1) \approx 1.15$, but for $P_2 \sim \mathcal{U}(0, 10)$ and $Q_2 \sim \mathcal{U}(-10, 20)$, $W_2(P_2, Q_2) \approx 11.5$, i.e. ten times greater, even if the relative error between P_1 and Q_1 is the same as the relative error between P_2 and Q_2. To account for this, and make metrics for different distributions more comparable, all distributions were first mapped onto the

standard normal distribution $\mathcal{N}(0,1)$ or uniform distribution $\mathcal{U}(-1,1)$ respectively with respect to the reference distribution to compare to. For a normal distribution $Q \sim \mathcal{N}(\mu, \sigma)$ with reference distribution $P \sim \mathcal{N}(\mu_{\text{ref}}, \sigma_{\text{ref}})$ the mapping gives

$$\begin{aligned} \hat{Q} &\sim \mathcal{N}(\hat{\mu}, \hat{\sigma}), \\ \hat{\mu} &= \frac{\mu - \mu_{\text{ref}}}{\sigma_{\text{ref}}}, \\ \hat{\sigma} &= \frac{\sigma}{\sigma_{\text{ref}}}. \end{aligned} \tag{5.32}$$

For a uniform distribution $Q \sim \mathcal{U}(a, b)$ with reference distribution $P \sim \mathcal{U}(a_{\text{ref}}, b_{\text{ref}})$ the mapping gives

$$\begin{aligned} \hat{Q} &\sim \mathcal{U}(\hat{a}, \hat{b}), \\ \hat{a} &= 2\frac{a - a_{\text{ref}}}{b_{\text{ref}} - a_{\text{ref}}} - 1, \\ \hat{b} &= 2\frac{b - a_{\text{ref}}}{b_{\text{ref}} - a_{\text{ref}}} - 1. \end{aligned} \tag{5.33}$$

When evaluating the metrics for the identified distributions to the actual distributions this was done by first mapping the identified distribution onto the relevant standard distribution with the actual distribution as a reference, and then calculating the 2-Wasserstein distance between the respective standard distribution and the remapped identified distribution. This will be referred to as the normalised 2-Wasserstein distance in this work.

The optimisation of the cost function was carried out using the quasi-Newton algorithm through the MATLAB function fminunc [57]. Different initial points were used for each estimation attempt, which were generated randomly within a certain range of the actual value. For each run the initial guess was randomly generated such that the guessed value $\hat{\theta}$ would deviate from the real value θ by at most some upper error limit $e_{\max}$ and at least by some lower error limit $e_{\min}$ according to

$$\hat{\theta} \in \{x : (1 + e_{\max})\theta \leq x \leq (1 + e_{\min}) \vee (1 - e_{\min})\theta \leq x \leq (1 - e_{\max})\}. \tag{5.34}$$

A visual representation of this scheme is illustrated in Figure 5.7, where the purple lines denote the range within which the generated value may land, the red points mark the error limits and the green point marks the actual value.

A total of three different tests were conducted, each with a different focus. First, to test whether or not the estimation worked at the most basic level, a total of ten estimation runs were carried out using the noiseless data. The initial guess was randomly generated with a lower error bound of 0% and an upper error bound of 25% for each run, with the mass of the load, $\hat{m}_{\text{load}}$, additionally being guessed for each identification run to be within the same error bounds. As mentioned, m_{load} was not being identified, but as its value was considered an unknown, which is why a random guess of its value was used as opposed to using the real mean value. This process was also repeated using the data with the inverted input signal $\boldsymbol{u}(t) = -\delta_{\max} \cos(\frac{\pi}{2}t)$. The purpose of this test was to see whether or not a different input signal would

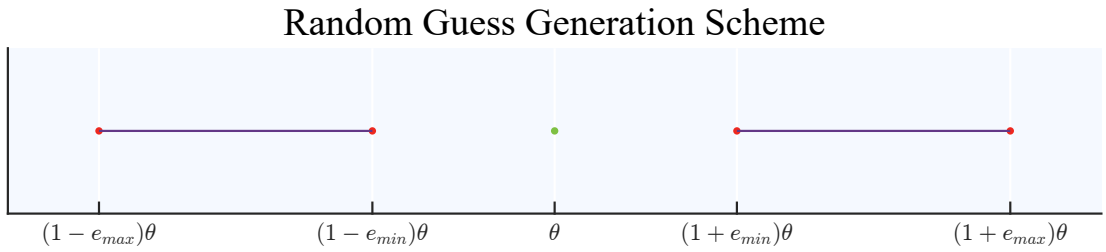

Figure 5.7: An illustration showing how the definition of the allowed range of initial guesses relative to the true value.

Table 5.5: The deviation of the initial guesses for each of the identified parameter values with respect to their actual values.

Estimation Run	1	2	3	4	5	6	7	8	9	10
Deviation	5%	10%	15%	20%	25%	30%	35%	40%	45%	50%

change the estimation error when using the data from the NLST model as estimation data.

Four estimates were produced in each estimation run. The first one using the measured data generated with the LST and using the STD cost function. The remaining three estimates were all produced using the measured data generated with the NLST. For each of these three estimates, a different cost function was used. STD for the first one, INP for the second one and DST for the final one.

The next step was to investigate the impact of poorer initial guesses. To achieve this, a further ten estimation runs were carried out, with initial guess deviations listed in Table 5.5. The error bounds for $\hat{m}_{\text{load}}$ were kept constant for all estimation runs, with the error being exactly 10%. As before, four estimates were produced in each estimation run with the same sets of measured data and cost functions being used as in the previous test.

Up until this point, the estimation had been performed assuming that the signals in the measured data are perfect. In practice however, signals will usually be imperfect and contain some level of noise. Therefore, in the same manner as before, a total of ten estimation runs were carried out, this time using the measured data sets two to eleven as listed in Table 5.3. For this, the deviation of the initial guesses and $\hat{m}_{\text{load}}$ was exactly 10% for each run.

After each identification run, the normalised 2-Wasserstein distance between each identified distribution and the corresponding real distribution was computed and plotted. Further, each of the identified distributions were plotted alongside the real distribution for visual comparison. These visualisations were used to observe the character of the identified distributions, in particular for the tests with increasing initial guess deviation and increasing noise.

Figure 5.8: An illustration of the test case used for evaluation of the controller.

5.4 Optimal Control with PCE

At last, the characteristics of controller based on the identified model were investigated. For this, a testing scenario of a lane keeping assistant was chosen. Here, a reference path was assumed to be set by some higher order system. The path was in this case set to be a straight line along $y = 0$, with the car's initial conditions being partially uncertain. The initial lateral offset was set to be uniformly distributed according to $\mathcal{U}(0\,\mathrm{m},\ 1.75\,\mathrm{m})$ with an initial uncertain yaw angle distributed by $\mathcal{U}(-5°,\ 5°)$. The car was set to be travelling at 70 $^{\mathrm{km}}/_{\mathrm{h}}$ with zero yaw rate and slip angle. The initial offset was chosen based on the assumption that a lane is typically 3.5 m wide [58], [59]. The chosen lateral offset thus corresponds to half of the width of the vehicle being outside of the desired lane. This testing scenario is illustrated in Figure 5.8.

In the typical LQR cost function in (4.63), the weighting matrices $\underline{Q}$ and $\underline{R}$ are $N_{\boldsymbol{x}}$ by $N_{\boldsymbol{x}}$ and $N_{\boldsymbol{u}}$ by $N_{\boldsymbol{u}}$ matrices respectively, where $N_{\boldsymbol{u}}$ is the number of input signals, in which the weights have to be chosen depending on the desired characteristics of the controller. When using the augmented system, the state vector and input vectors are both N_ϕ times longer than before, with the consequence that the weighting matrices $\underline{Q}_{\mathrm{PCE}}$ and $\underline{R}_{\mathrm{PCE}}$ in (4.71) have significantly more elements than their counterparts for the original system formulation. Since the elements of these matrices are all design parameters, the task of choosing these becomes more complex.

The approach used in this project was inspired by that of Gallant [45]. Weighting matrices $\underline{Q}$ and $\underline{R}$ were chosen for the original system first. A single new design parameter γ was then introduced to adjust the variance penalty, with which $\underline{Q}_{\mathrm{PCE}}$ and $\underline{R}_{\mathrm{PCE}}$ were set as

$$\underline{Q}_{\mathrm{PCE}} = \gamma \underline{Q} \otimes \begin{bmatrix} 1 & & \\ & 0 & \\ & & 0 \\ & & & \ddots \end{bmatrix} + (1-\gamma)\underline{Q} \otimes \begin{bmatrix} 0 & & \\ & 1 & \\ & & 1 \\ & & & \ddots \end{bmatrix}, \tag{5.35}$$

and

$$\underline{R}_{\text{PCE}} = \gamma \underline{R} \otimes \begin{bmatrix} 1 & & & \\ & 0 & & \\ & & 0 & \\ & & & \ddots \end{bmatrix} + (1-\gamma)\underline{R} \otimes \begin{bmatrix} 0 & & & \\ & 1 & & \\ & & 1 & \\ & & & \ddots \end{bmatrix}. \tag{5.36}$$

Meaning that the weights from $\underline{Q}$ and $\underline{R}$ were split between the mean and variance of each state- or input variable by some ratio γ. This way, the number of design parameters was kept lower than by weighting each of the expanded system's state variables individually. Further, the matrices $\underline{Q}$ and $\underline{R}$ could be picked as in the more familiar LQR case. Again inspired by Gallant [45], whose work pertains to a similar control problem as the one studied here, the weighting matrices were chosen as

$$\underline{Q} = \begin{bmatrix} 1 & 0 & 0 & 0 \\ 0 & 1 & 0 & 0 \\ 0 & 0 & 1 & 0 \\ 0 & 0 & 0 & 10 \end{bmatrix}, \tag{5.37a}$$

$$\underline{R} = 100. \tag{5.37b}$$

With the weighting matrices set, an LQR and SLQR were synthesised based on the known model. The LQR was synthesised using the mean values for each of the stochastic uncertainties. The weighting matrices used were $\underline{Q}$ and $\underline{R}$ using the MATLAB function lqr, ignoring the disturbance. The SLQR was based on proposition (4.66), taking the time variant disturbance into account.

When the time variant disturbance is modelled by KLE, the dynamic model is only valid over a limited time span $[0, T]$ as the method used to compute the KLE made it valid only over a finite time horizon. This had the consequence that the analytical formulations for stochastic optimal control (4.72) [9], [49] could not be used. Instead, the cost function (4.71) was reformulated to a discrete sum

$$\begin{aligned} &\underline{K} = \arg\min_{\underline{K}} \sum_{i=0}^{N} \boldsymbol{X}^{\intercal}(t_i) \left(\underline{Q}_{\text{PCE}} + (\underline{K}^{\intercal} \otimes \underline{I}_{N_{\boldsymbol{X}}}) \underline{R}_{\text{PCE}} (\underline{K} \otimes \underline{I}_{N_{\boldsymbol{X}}}) \right) \boldsymbol{X}(t_i), \\ &\text{such that } \dot{\boldsymbol{X}}(t) = f_{\text{PCE}}(t, \boldsymbol{X}(t), \boldsymbol{U}(t)), \\ &\qquad\qquad \boldsymbol{X}(0) = \boldsymbol{X}_0, \end{aligned} \tag{5.38}$$

which was evaluated by simulating the linear PCE augmented system from time 0 to time T using the same stochastic initial conditions as in the test case. To choose T, the system was simulated using the LQR. Based on the simulation output from this, T was then chosen to be greater than the time taken for the system to reach its steady state.

6

Results

The results are all covered in this chapter. First, the measured data generated using Monte Carlo simulations is presented in Section 6.1. This section is followed by an overview of the identification results in Section 6.2. The results of the controller testing are listed in Section 6.3.

6.1 Measured Data

In Figure 6.1, the noiseless data from the 2000 sample Monte Carlo simulation of the LST model are presented. The mean and variance over time is visualised, with the variance band in the figure encompassing three standard deviations either side of the mean, thus capturing 99% of output trajectories. Similarly, the noiseless data produced by simulating the NLST model are presented in Figure 6.2. Further, the means and variances over time of the noise-corrupted LST and NLST data sets have been plotted in Figures 6.3 and 6.4 respectively.

As can be seen in Figures 6.3 and 6.4, increasing the noise adds variance in the system output for all times. This effect is most prevalent for state variables which have relatively small variance, as the added noise than accounts for a larger proportion of the total variance. The addition of noise in the signal does not affect the means noticeably.

Moreover, both the LST- and NLST model outputs without noise have been plotted together in Figure 6.5 and the KLD between the noiseless LST model and NLST model data over time has been plotted in Figure 6.6. This provides a measure of how different the normal distributions of each state variable are for the LST and NLST models. Recall that this was used as the basis of the DST cost functional (5.28) for the identification.

6.2 Identification of Probability Distributions

The results from the estimations of probability distribution parameters are presented in this section. In Section 6.2.1, the ten estimates produced using random initial guesses are presented along with the estimate using the data from the non-linear model with opposite steering input, the estimates using the inverted steering input

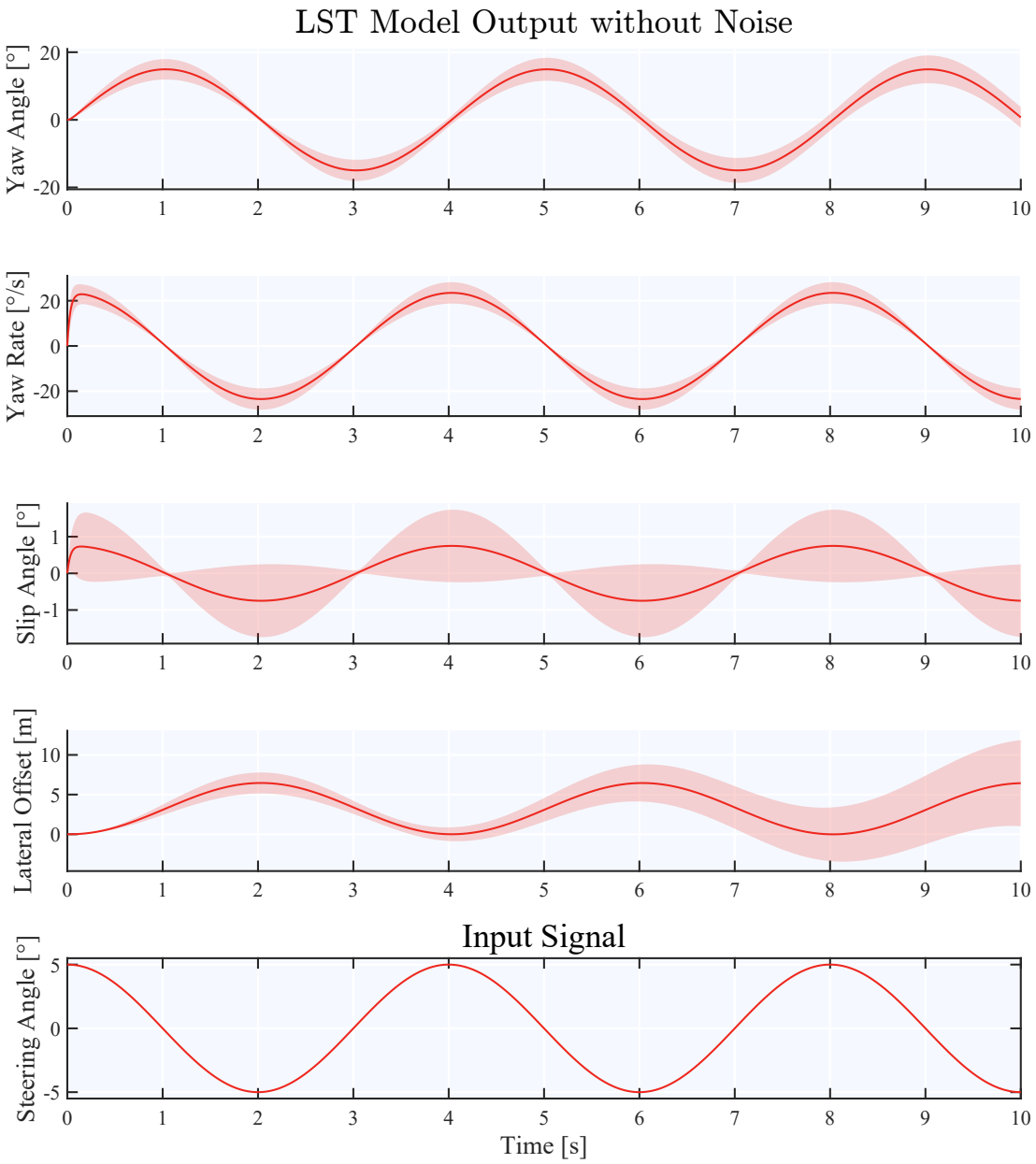

Figure 6.1: The measured data from 2000 simulated samples of the LST model.

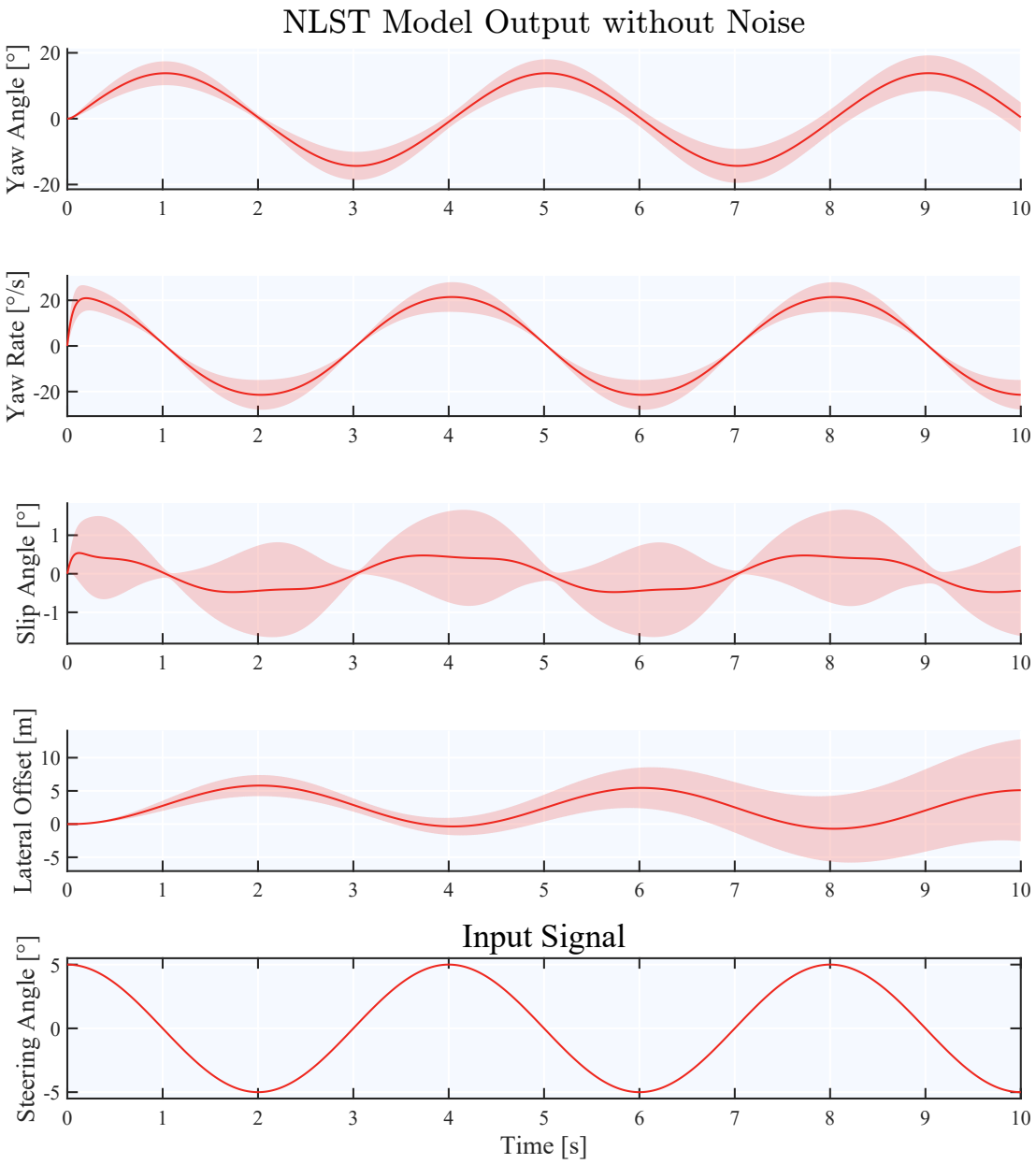

Figure 6.2: The measured data from 2000 simulated samples of the NLST model.

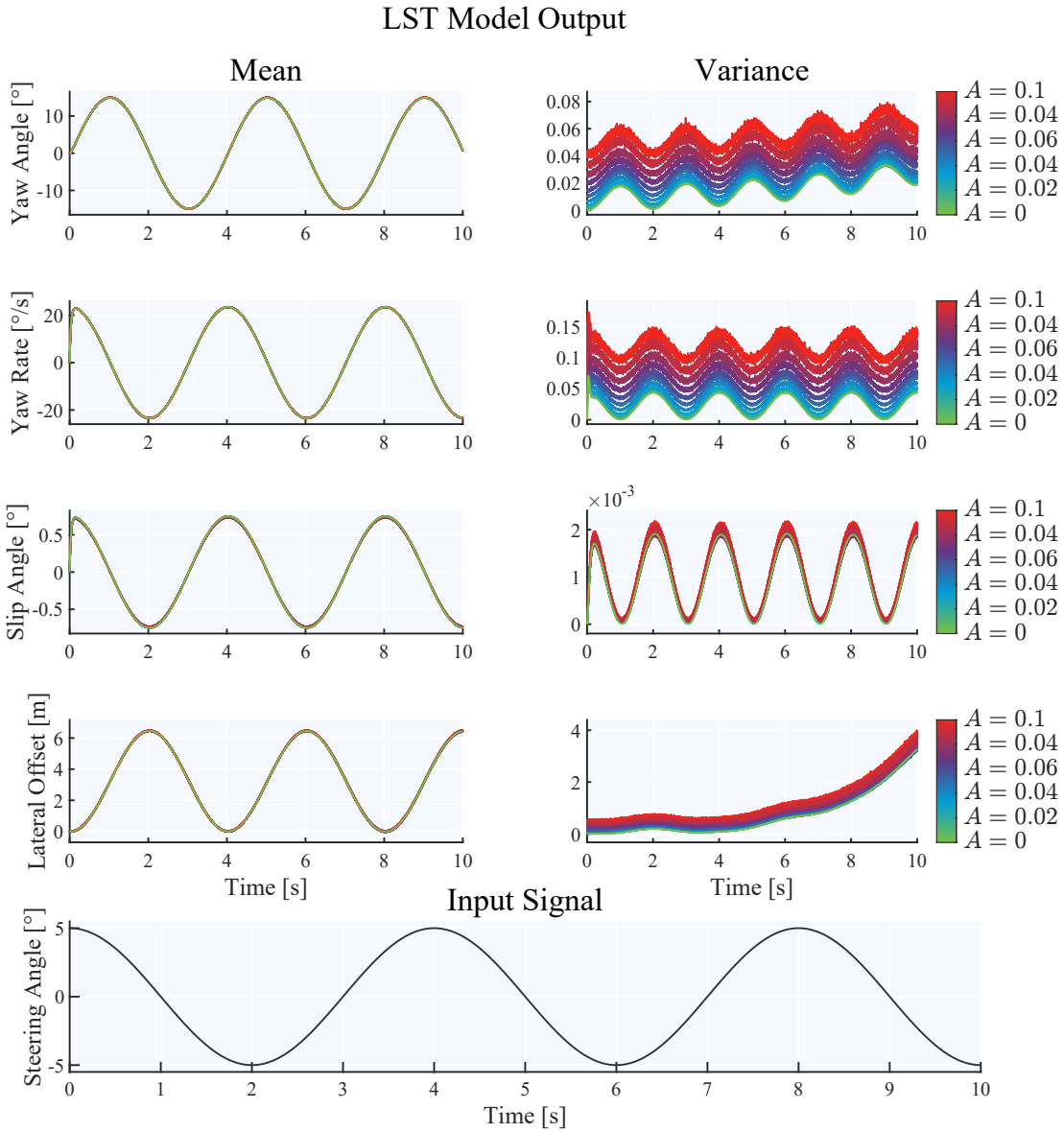

Figure 6.3: The means and variances of the LST model outputs for differing noise intensities.

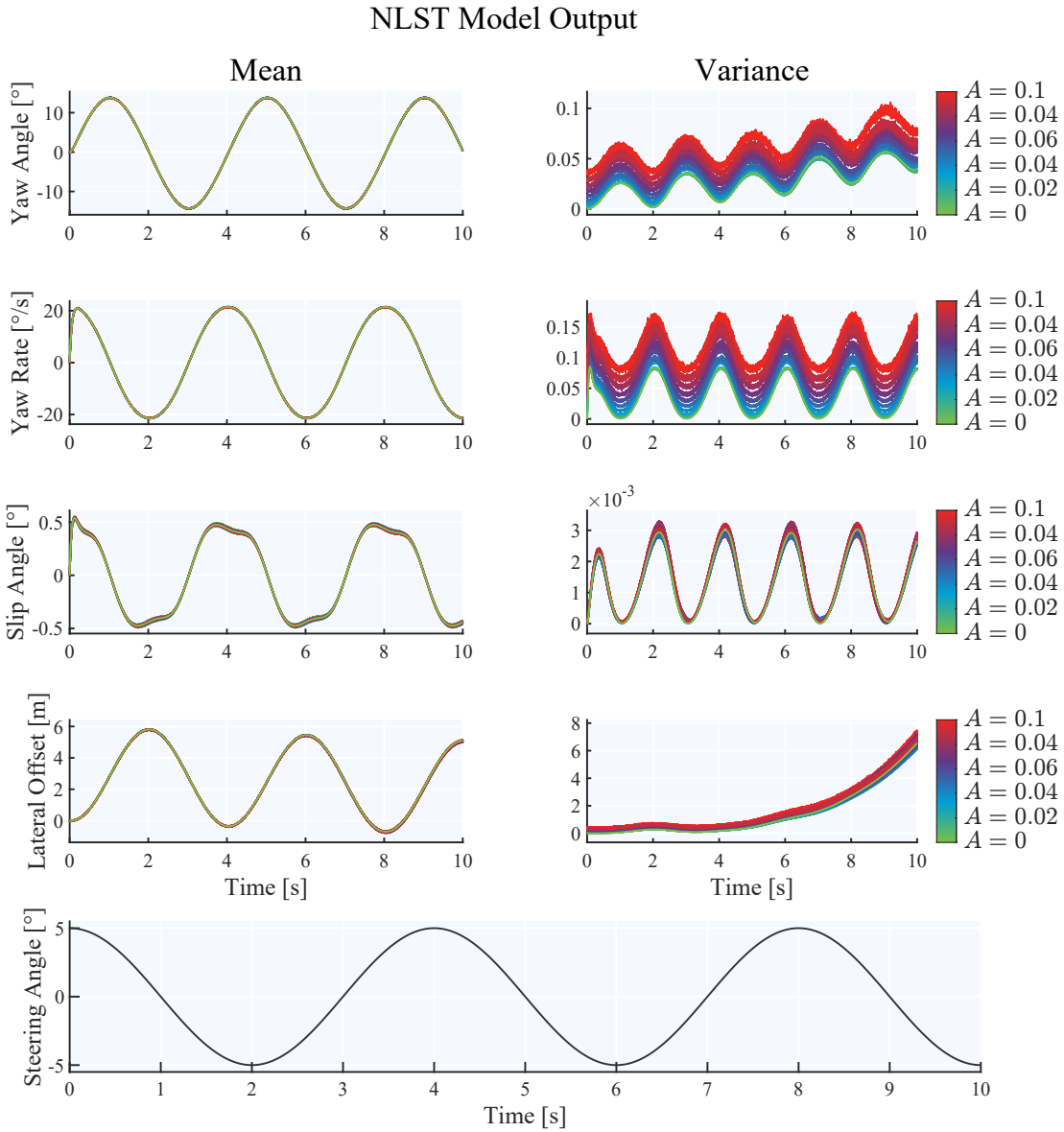

Figure 6.4: The means and variances of the NLST model outputs for differing noise intensities.

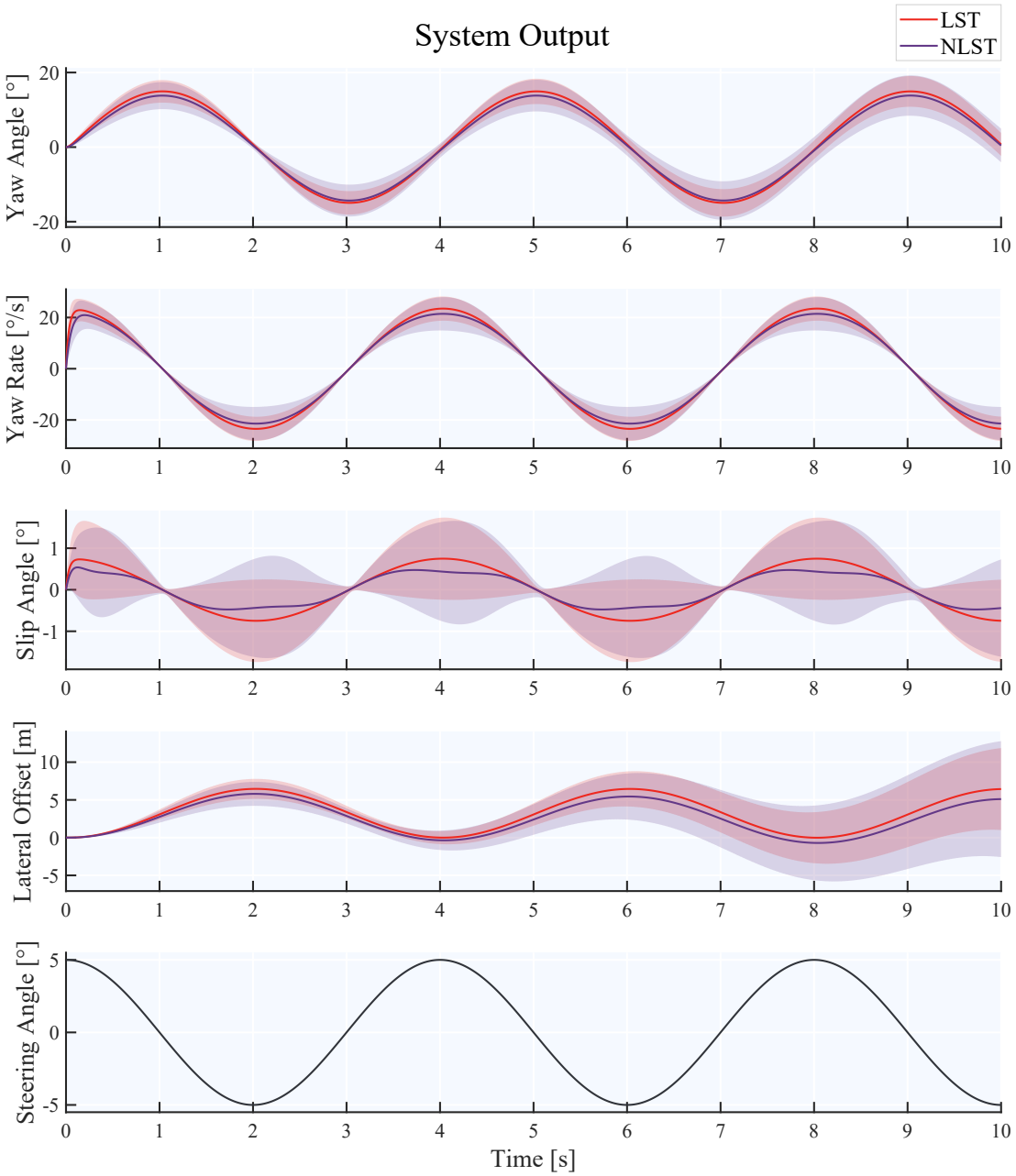

Figure 6.5: Outputs of both the LST and NLST models with stochastic parameter values.

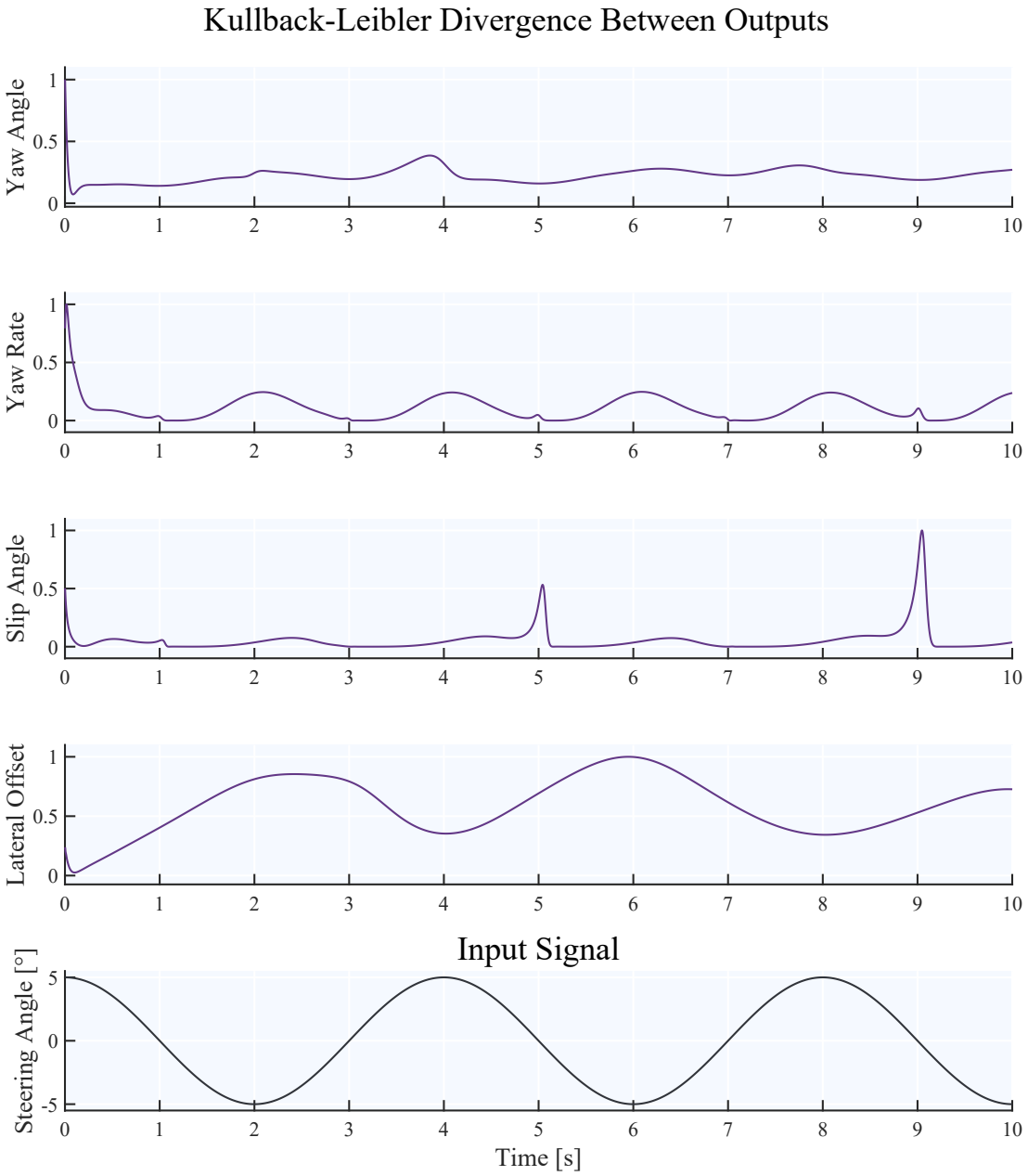

Figure 6.6: Kullback-Leibler divergence over time between the LST and NLST outputs of each state variable.

Table 6.1: True distributions of the parameters identified.

Parameter	μ	l_f [m]	$\bar{F}_\mathrm{w}$ [N]
Distribution	$\mathcal{N}(1, 0.2)$	$\mathcal{N}(1.55, 0.2)$	$\mathcal{U}(-400, 400)$

Table 6.2: Numeric values of the estimates produced using the inverted steering input.

Data Source	Cost Function	μ	l_f [m]	$\bar{F}_\mathrm{w}$ [N]
LST	STD	$\mathcal{N}(0.998, 0.202)$	$\mathcal{N}(1.542, 0.196)$	$\mathcal{U}(-412, 419)$
NLST	STD	$\mathcal{N}(0.797, 0.192)$	$\mathcal{N}(1.523, 0.222)$	$\mathcal{U}(-389, 608)$
NLST	INP	$\mathcal{N}(0.798, 0.192)$	$\mathcal{N}(1.524, 0.223)$	$\mathcal{U}(-383, 603)$
NLST	DST	$\mathcal{N}(0.807, 0.199)$	$\mathcal{N}(1.533, 0.213)$	$\mathcal{U}(-392, 596)$

data also appears in this section as a special case. Another eleven estimates are presented in Section 6.2.2, where the accuracy of the initial guesses was gradually increased. The estimates using the data sets with noise are presented in Section 6.2.3.

In the following, identifications performed using the data from the linear model are refferd to as LST-LST, and those performed using the recorded data from the non-linear model have been denoted NLST-LST. Further, the type of cost function used may also be denoted in square brackets, so NLST-LST [INP] denoted an identification carried out using the NLST model data with the input weighted cost function. For each of the tests, the estimated distributions have been plotted together with the true distributions for a visual representation. The figures seen as most relevant are presented here, the remaining figures can be found in Appendix B. The numeric values of the identified distributions are presented in tables throughout this section. for reference, the actual distributions are presented in Table 6.1.

6.2.1 Basic Identification Test

Figures 6.7 and 6.8 show the two 2-Wasserstein distance between each identified distribution to the real distribution, for each estimate. It can be seen in general that the 2-Wasserstein distances of the estimates to the real distributions are consistent across all ten estimates regardless of the initial guess. It can further be observed that when the measured data from the non-linear model is used, the DST cost function produces estimated which mostly have a slightly lower 2-Wasserstein distance to the real distributions across all ten estimation runs. The average numeric values of the ten estimated can be seen in Table 6.2. The results using the inverted steering data set are presented in Section 6.2.1.1 and the results seen from this test are briefly discussed in Section 6.2.1.2.

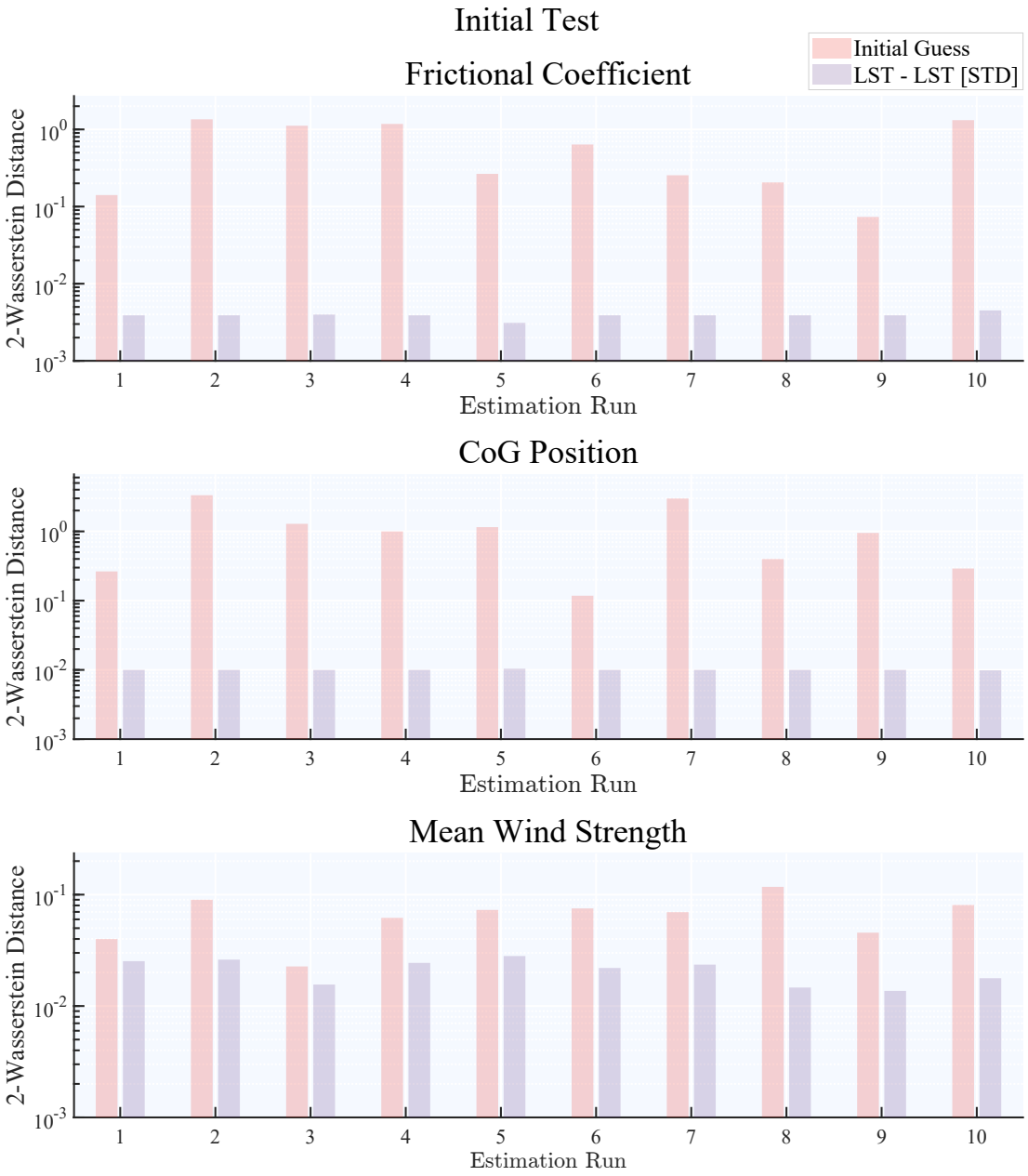

Figure 6.7: The normalised 2-Wasserstein distance between the distributions identified based on the data from the LST model and the real distributions.

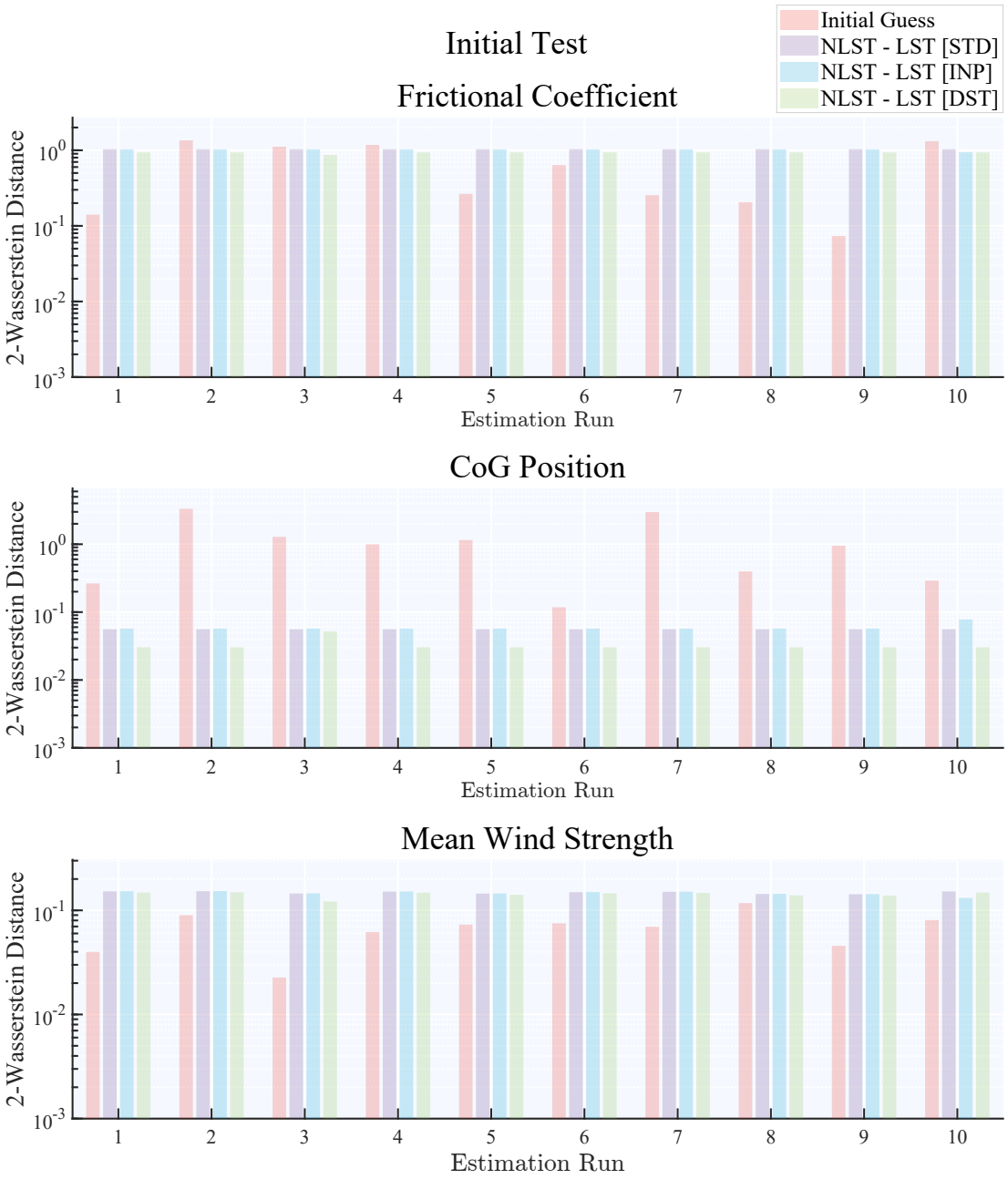

Figure 6.8: The normalised 2-Wasserstein distance between the distributions identified based on the data from the NLST model and the real distributions.

Table 6.3: Numeric values of the estimates produced using the inverted steering input.

Data Source	Cost Function	μ	l_f [m]	$\bar{F}_\mathrm{w}$ [N]
NLST	STD	$\mathcal{N}(0.796, 0.189)$	$\mathcal{N}(1.514, 0.219)$	$\mathcal{U}(-370, 597)$
NLST	INP	$\mathcal{N}(0.796, 0.189)$	$\mathcal{N}(1.513, 0.219)$	$\mathcal{U}(-374, 601)$
NLST	DST	$\mathcal{N}(0.805, 0.195)$	$\mathcal{N}(1.523, 0.211)$	$\mathcal{U}(-378, 590)$

6.2.1.1 Inverted Steering

The identified disturbances using the STD cost function with the inverted steering input can be seen in Figure 6.9. From the figure, it appears that there is no discernible difference in the frictional coefficient and CoG position estimates, however the estimate of the mean wind strength distribution appears slightly shifted in the opposite direction to what was seen in the previous results. The numerical values of the estimates are presented in Table 6.3.

6.2.1.2 Modelling Error Propagation

When identifying the model based on the data from the LST model, the errors between the identified distributions and actual distributions small for the initial guesses within error range 0% to 25%. This result suggests that under the condition that the model being identified has a similar enough structure to the real system, the approach used in this project is capable of providing accurate estimates of the distributions of uncertainties in a dynamic model.

By identifying the LST model based on data from the NLST model, it can be observed from the values in Table 6.2, that the model simplifications propagate through and result in errors between the identified distributions and actual distributions. Still, the identification results appear to be consistent for the initial guesses within the 0% to 25% error interval. In general, the frictional coefficient is underestimated, although its variance is close to correct. This tendency to underestimate the friction is not a surprise. The ideal magic formula linearisation $F(F_z, x) = F_z BCDx$ used for the LST model, linearises the tyre curve at the origin, meaning that the level of traction is always somewhat overestimated compared to the non-linear tyre model. When identifying a linear tyre model based on the non-linear model, the slope of the identified line is therefore somewhat lower that the ideal magic formula linearised model. This is also illustrated in Figure 6.10, where the tyre curves for the non-linear model, the ideal linearisation and one of the NLST-LST estimated models corresponding to their respective mean frictional coefficients have been plotted.

The distance between the front axle and the CoG is also slightly underestimated in the estimate produced based on the NLST model data. The CoG position has a large influence on the slip angle of the vehicle, evident from the sensitivity analysis in Figure 5.4. This result would be expected since the slip angle is calculated at the CoG, thus implicitly connecting the CoG position to the slip angle. The error here is therefore likely in large part due to the mismatch in slip angles between the LST

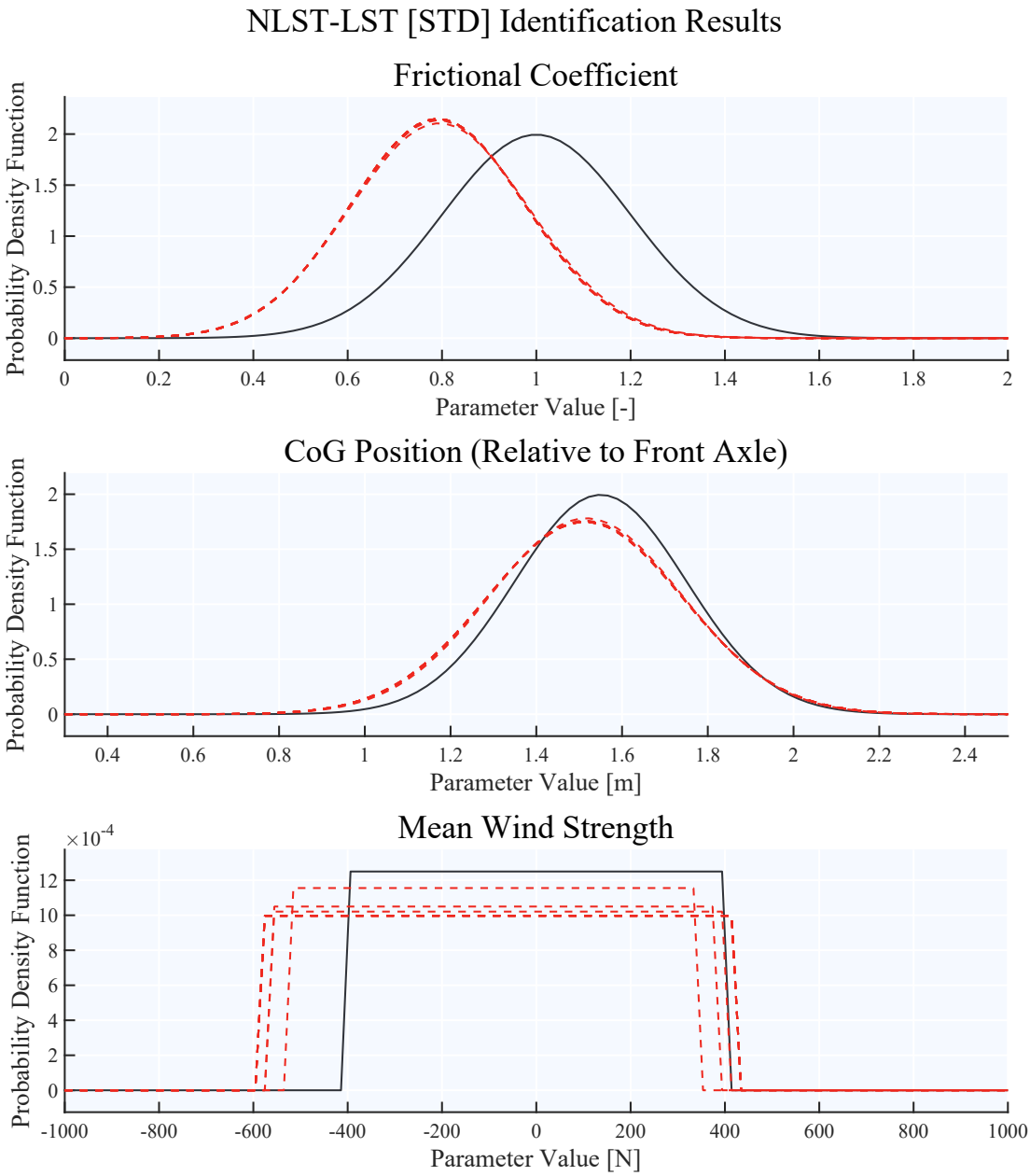

Figure 6.9: Estimates produced based on the NLST model data using the STD cost function and inverted steering angle.

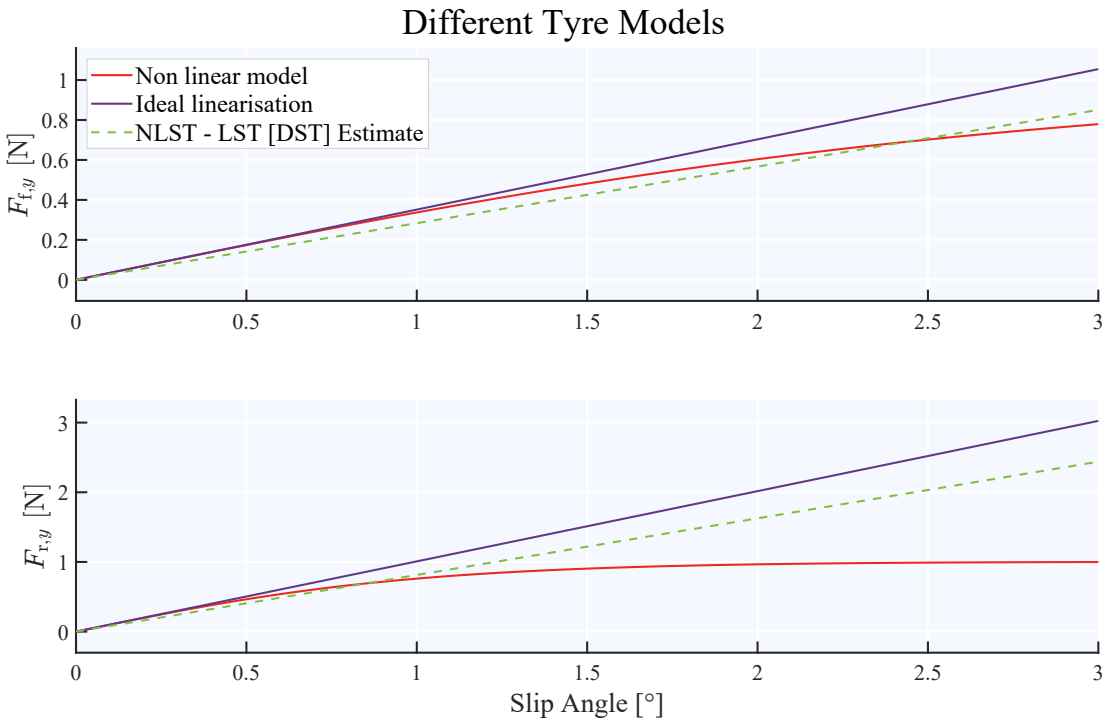

Figure 6.10: Ideal and estimated tyre curves plotted for comparison.

and NLST models. In some applications, the slip angle is instead calculated at a point fixed to the car body. In such a case, the sensitivity may be different.

What is also notable in the identified distributions estimated on NLST model data, is that the distribution of the mean wind strength is shifted slightly in the positive direction. This effect is reversed when reversing the steering angle as can be seen from the values in Table 6.3, where it can be seen that the estimate of the same distribution shifts the other way. This can be explained by the fact that the vehicle then moves in the opposite direction, it is possible that the error in the estimate is a compensation for the error in lateral offset seen between the LST and NLST models in Figure 6.5 earlier.

In more general terms however, this observation suggests that the propagation of the model error into the estimated probability distribution is also input-specific. This is reasonable as different inputs have the potential of highlighting different aspects of the modelling error, making that error then also appear more prominently in the estimates. This also means that it may be possible to find some ideal input trajectory to minimise the model error. In this project for example, the error in the mean wind strength distribution estimate could possibly have been mitigated by choosing an input such that the car would drive a symmetrical path around the line of zero lateral offset, rather than the asymmetric paths which are driven with both steering profiles used in this project.

6.2.2 Initial Guess Sensitivity

As before, the identified distributions can be found in Appendix B. Again, the 2-Wasserstein distance of each initial guess and estimate to the true distributions has been plotted in Figures 6.11 and 6.12. The results show that the estimates of the frictional coefficient and CoG position are consistent regardless of the initial guess, however, the estimate of the wind varies across the different estimates.

Weighting schemes were used here to see if they could improve the identification accuracy when using the NLST model data, and indeed, using the DST cost function often returned better results than using the STD or INP cost functions, except for the case when the initial guess deviation was 45% or above. There was however little difference between the STD and INP cost functions. Although the improvement with the DST cost function was minor, the result suggests that it is possible to use well thought out weighting schemes to mitigate some of the model simplification error. The exact weighting schemes used in this project were chosen relatively arbitrarily. Conducting a more methodical investigation into different weighting schemes may make it possible to generate more accurate estimates.

The observation that the estimates produced with initial guesses deviating 50% from the actual values suggests that it is of importance that the initial guess is within a certain range. Why exactly this occurs is unclear, a possibility is that the optimiser finds some local minimum. To investigate this, the shape of the cost function would have to be investigated further. This is also something that would have to be considered in general on a system-by-system basis, since the geometry of the cost function would be system specific.

6.2.3 Noise Sensitivity

With increasing noise, the 2-Wasserstein distance of the estimates increases with increasing noise as can be seen in Figures 6.13 and 6.14. a pattern can be seen in the identified distributions when the identification model structure matches the real system. For the frictional coefficients, the mean tends to increase, as does the variance when the level of noise increases. The mean of the CoG position remains unchanged with increasing noise, but the variance tends to decrease, at some point reaching close to zero. The distribution for the wind tends to get wider as the level of noise increases. When the data from the non-linear model is used as the estimation data, the same tendency is shown, but the pattern is slightly less clear.

Adding noise in the data appears to reduce the overall accuracy. This addition results in wider variance bands in the data, which results in a larger variance and higher mean being identified for the frictional coefficient. The opposite is true for the CoG position, for which the identified variance decreases while the mean remains the same. The identified range of wind strengths also increases with increasing noise.

The increase in variance in the frictional coefficient estimate and the increased range of the wind strength estimate likely account for the increased variance recorded in all state variables when the noise is added. The fact that the variance of the CoG

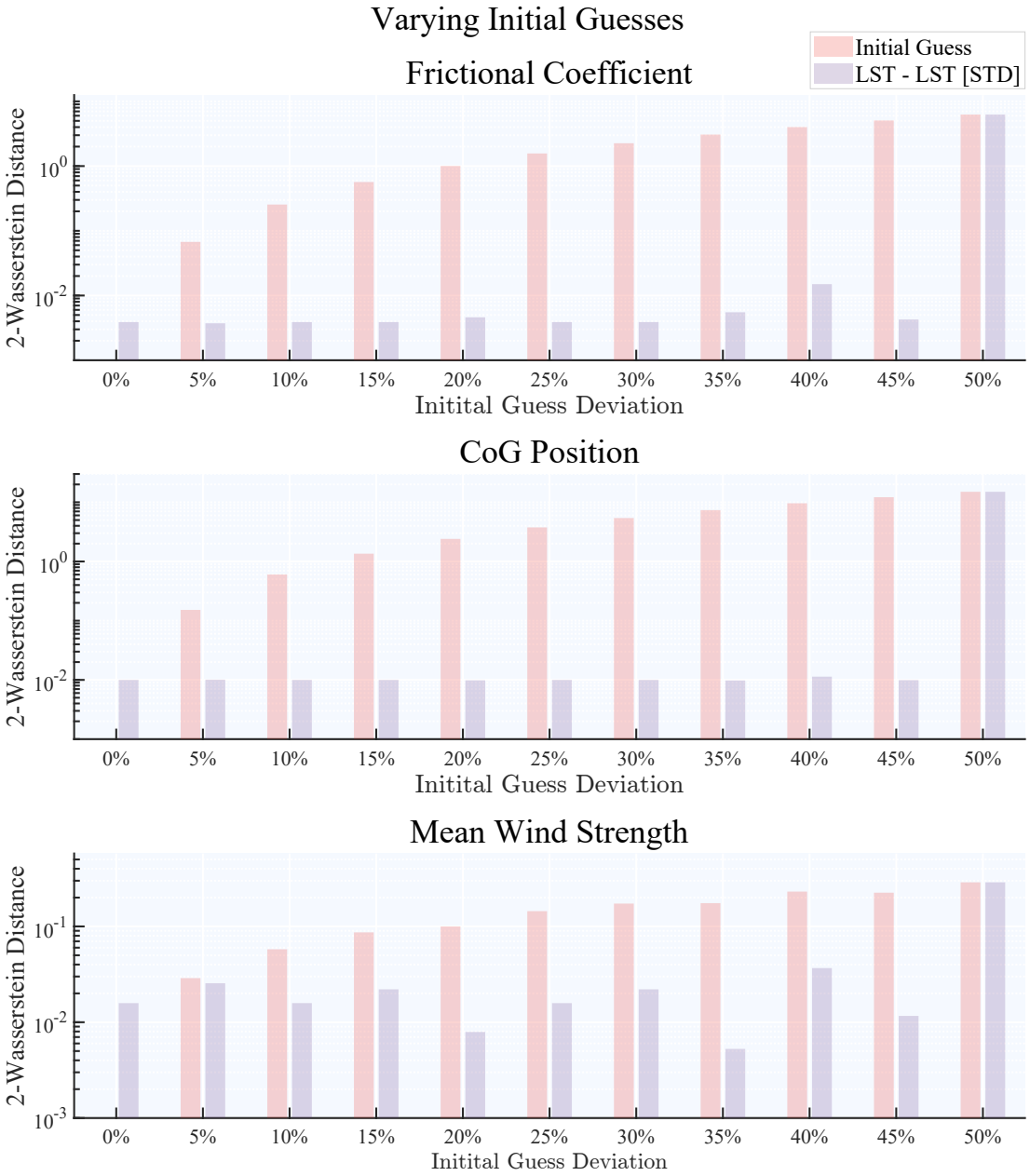

Figure 6.11: The normalised 2-Wasserstein distance between the distributions identified based on the data from the LST model and the real distributions for different noise initial guesses.

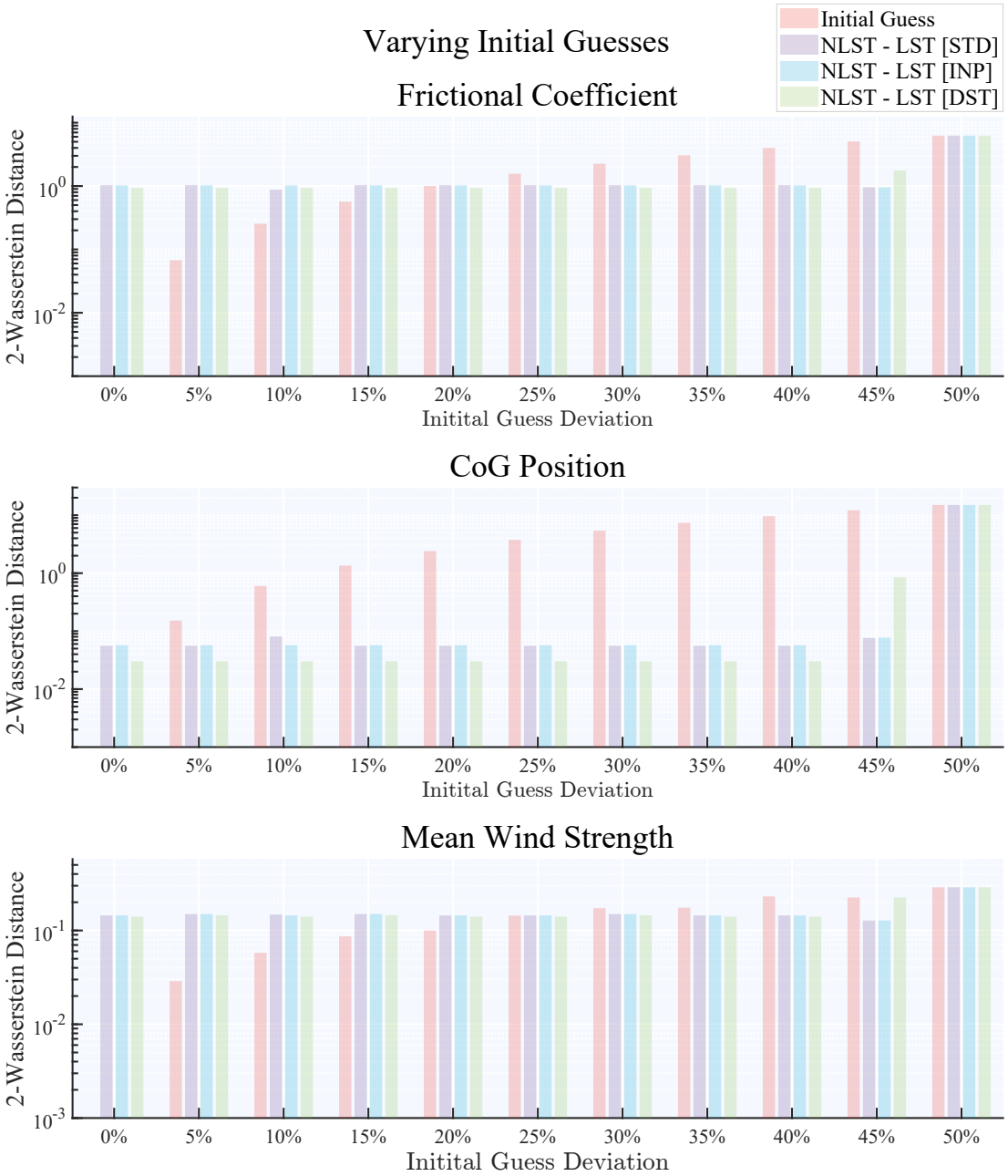

Figure 6.12: The normalised 2-Wasserstein distance between the distributions identified based on the data from the NLST model and the real distributions for different noise initial guesses.

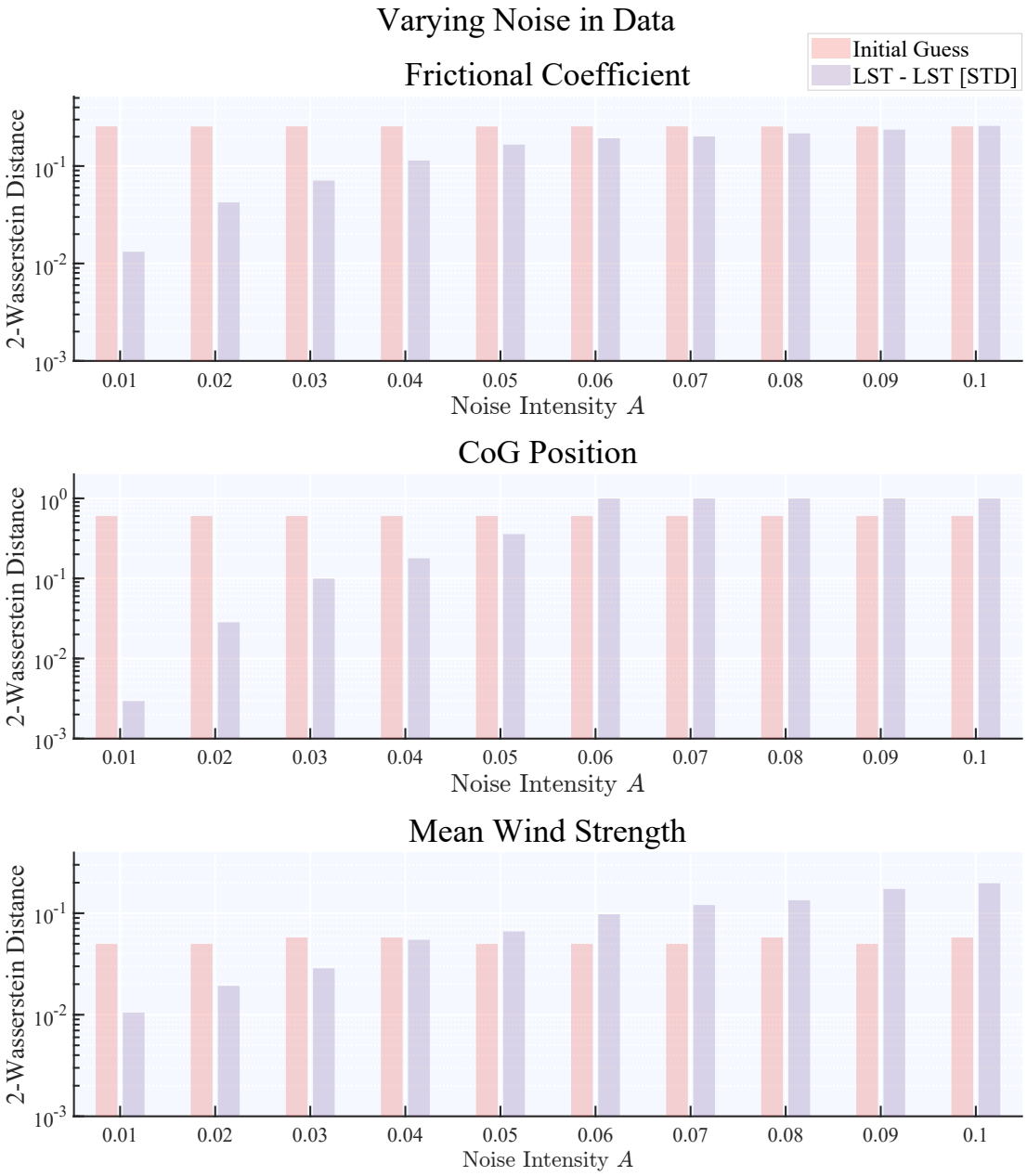

Figure 6.13: The normalised 2-Wasserstein distance between the distributions identified based on the data from the LST model and the real distributions for different noise intensity levels.

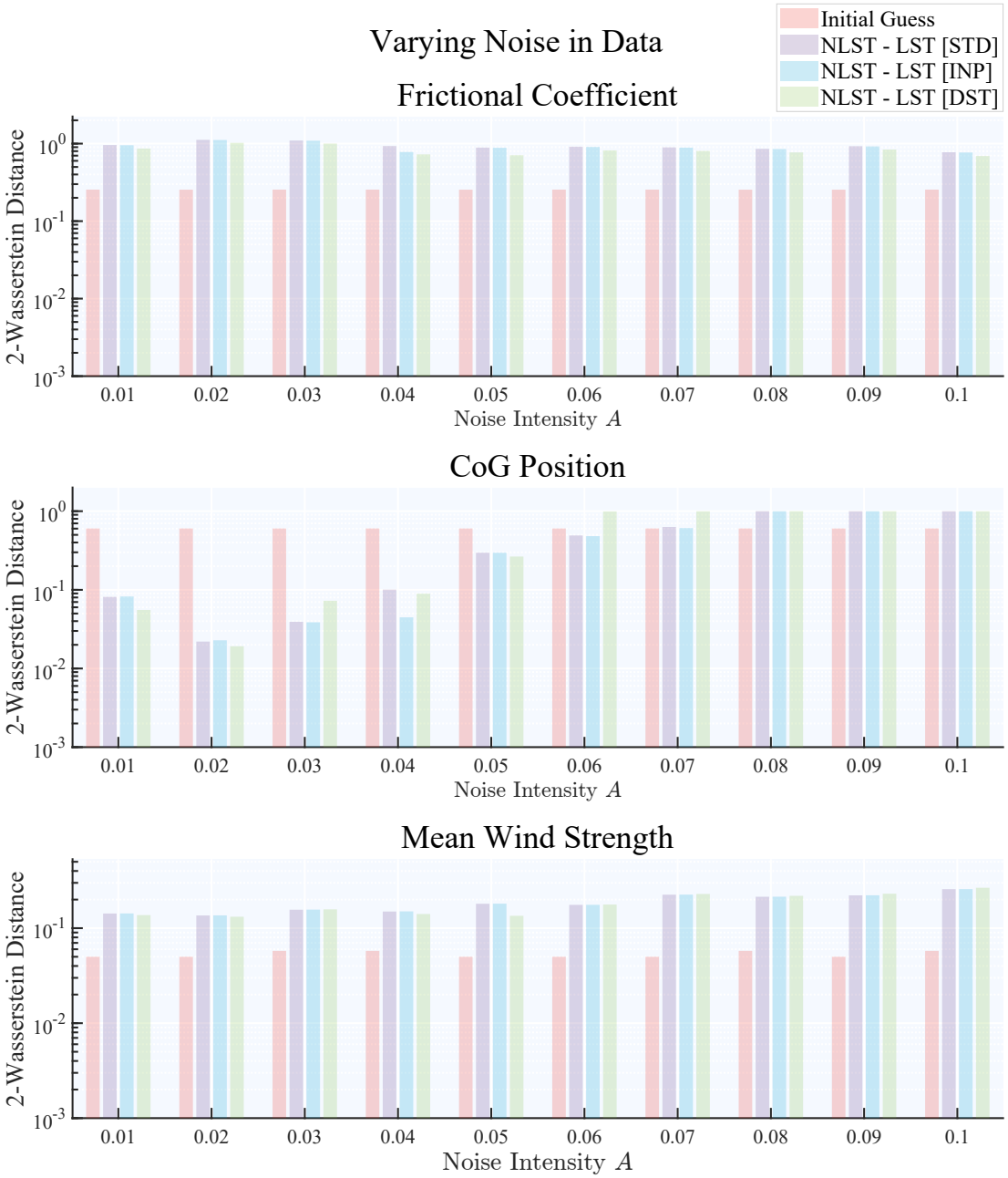

Figure 6.14: The normalised 2-Wasserstein distance between the distributions identified based on the data from the NLST model and the real distributions for different noise intensity levels.

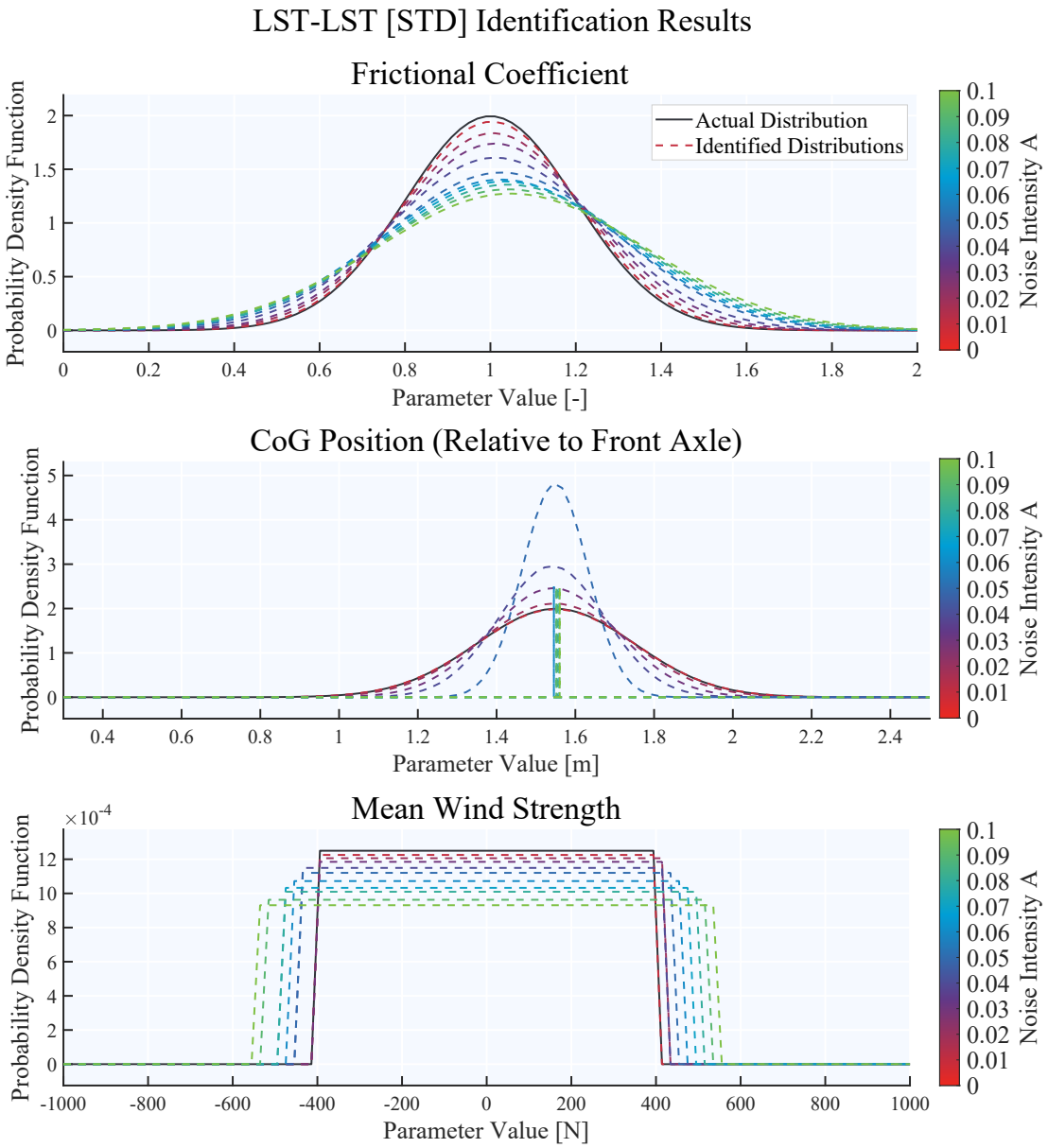

Figure 6.15: Estimates produced based on the LST model data using the STD cost function.

position estimate decreases may be explainable by looking at the sensitivity analysis in Figure 5.4. Here, it can be seen that the CoG position only has significant influence on the slip angle state variable. The frictional coefficient also has a significant influence on the slip angle as well as all other state variables. Therefore, one possible explanation for the decrease in variance in CoG position is that the increased variance in frictional coefficient accounts for all slip angle variance alone.

In general, it is evident from the results that adding noise to the measurements results in worse estimates. Adding noise to the measurement data increases the calculated output variance, although the mean remains the same. But since the parameters of the identified model are chosen to try to match the recorded variance and mean, the increased variance naturally produces different estimates. This highlights the importance of dealing with noise in post-processing ahead of estimation in order to generate good estimates.

6.3 Control Using SLQR

Synthesising an LQR based on the mean of all stochastic parameters resulted in the control gain matrix

$$\underline{K} = \begin{bmatrix} -1.85 & -0.05 & -0.49 & -0.32 \end{bmatrix}. \tag{6.1}$$

Simulating the test case using the stochastic LST model with this control gain resulted in the system output plotted in Figure 6.16. As the system appears to have settled after about one second, with this information, T was set to two for the SLQR synthesis, which resulted in the control gain

$$\underline{K} = \begin{bmatrix} -1.81 & -0.067 & 0.22 & -0.30 \end{bmatrix}, \tag{6.2}$$

when using $\gamma = 0.001$, a choice made based on the observations of Gallant [45].

The results of simulating the test case with both the LQR and SLQR can be seen in Figure 6.17. As both control gains are very similair to each other, the resulting output is also very close. A slight difference between the two controllers can be seen when simulating the test case is simulated using the stochastic NLST model, for which the outputs with both the LQR and SLQR have been plotted in Figure 6.18. Here, using the SLQR appears to result in a slightly smaller variance in the slip angle, but is otherwise mostly indistinguishable from the LQR case.

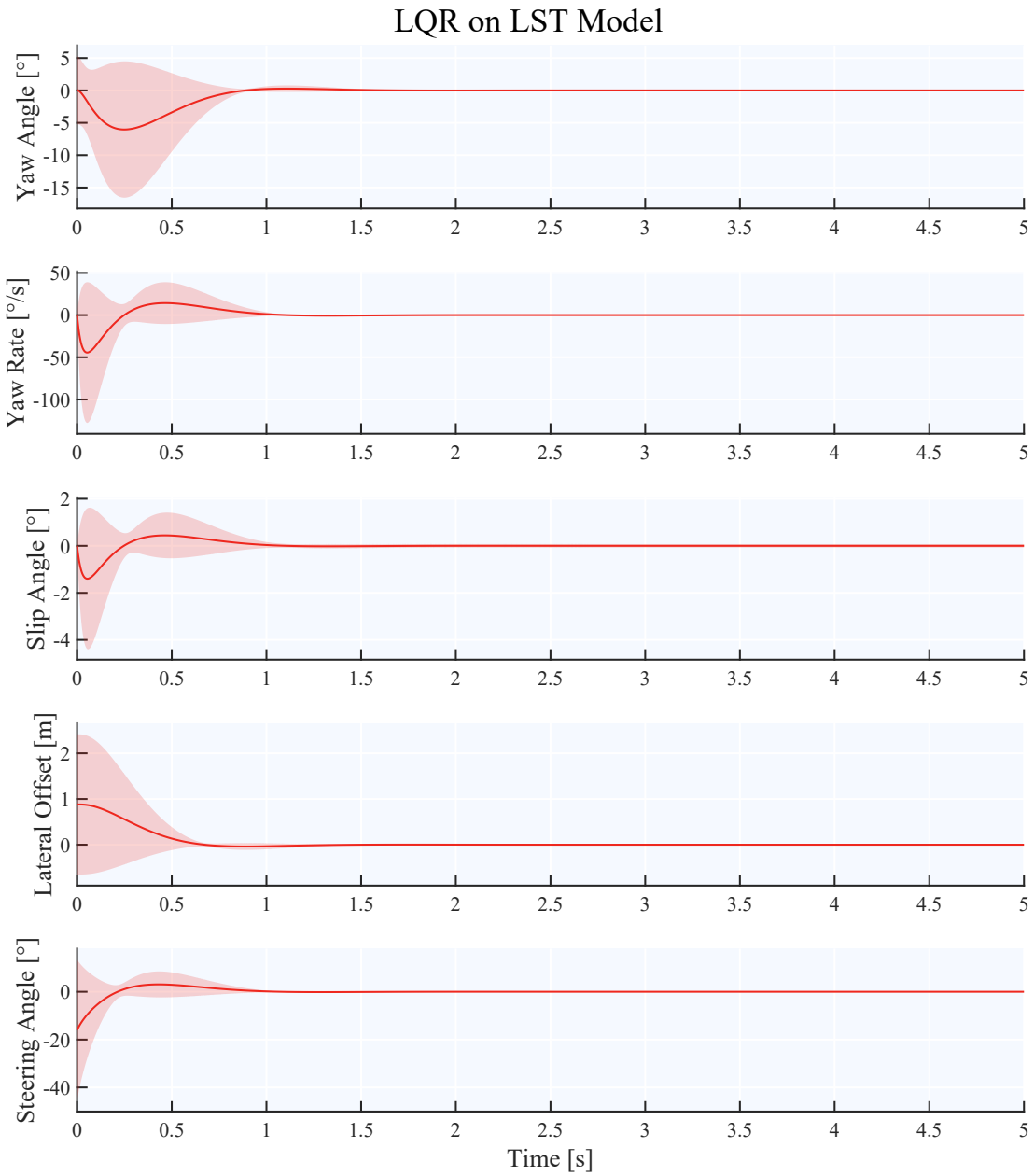

Figure 6.16: Simulation results using the LST model in the test case with the LQR. Used to pick T.

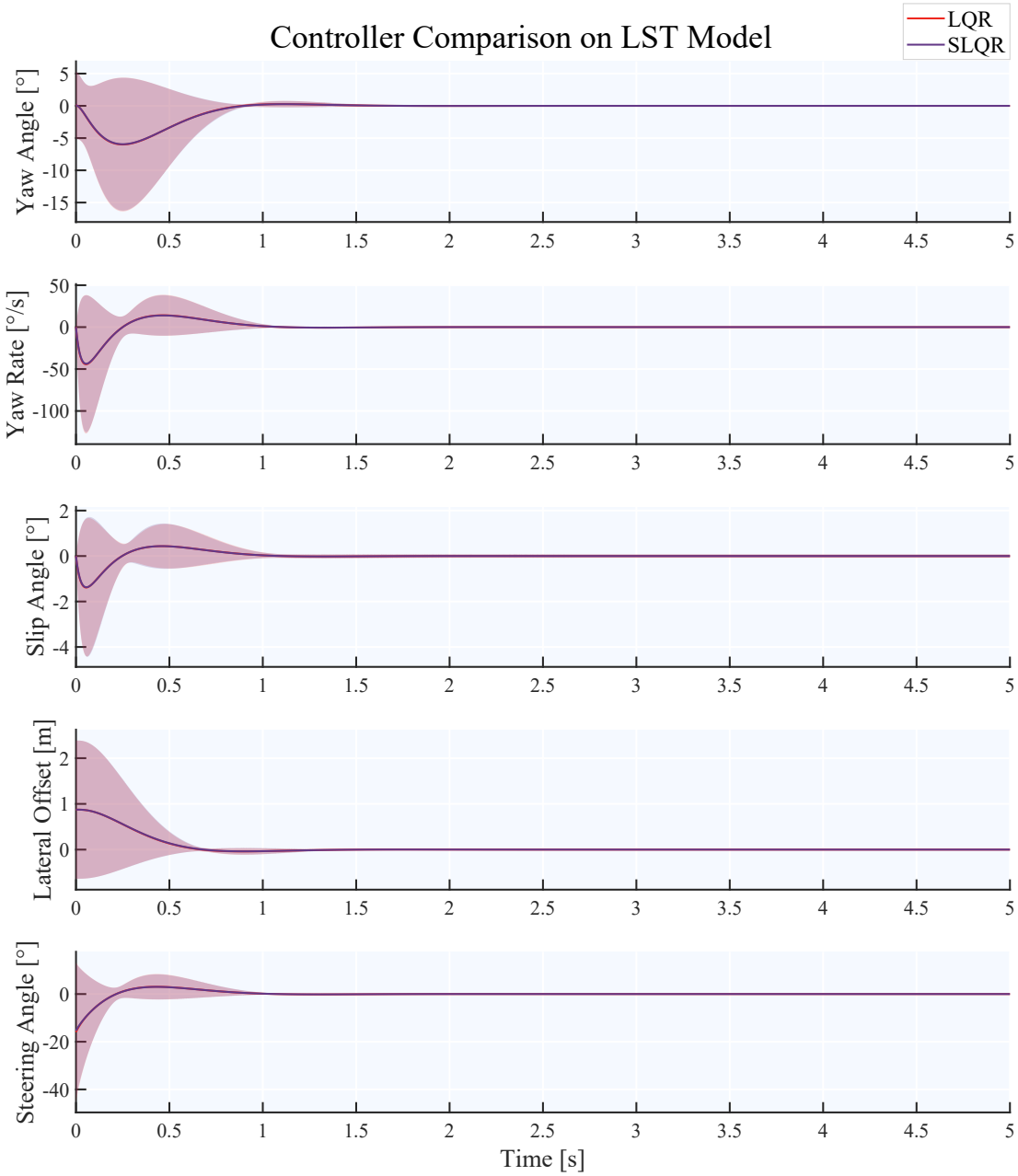

Figure 6.17: Simulation results using the LST model in the test case with both the LQR and SLQR.

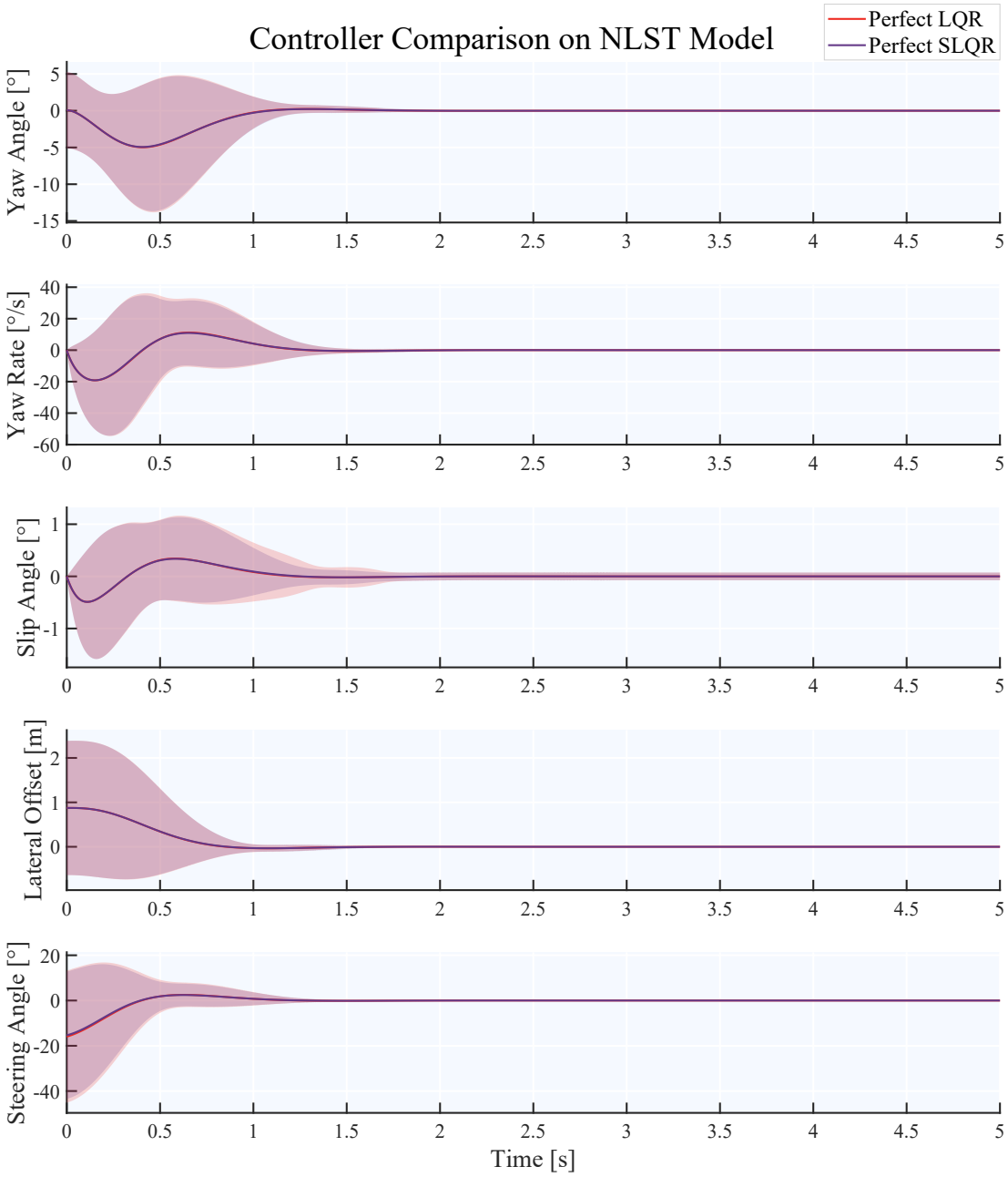

Figure 6.18: Simulation results using the NLST model in the test case with both the LQR and SLQR.

7

Future Outlook

In this chapter, the project's relevance in the broader context is discussed. Recommendations based on the experience gathered during the project are presented, which can be used as a base for future research, or as points of consideration in general when applying the concepts and methods used in this project. The estimation process is covered first in Section 7.1, followed by discussion regarding control of a system using the PCE model in section 7.2. Lastly, a discussion about the PCE and KLE as used in the project is presented in Section 7.3.

7.1 Identification of Parameters

The approach used to identify parameters has in general proven itself to work, delivering consistent results. As is shown by the results, when a perfect model structure is used, the estimate gets close to the correct solution. When the identified model has a simplified structure compared to the model from which the data comes, the estimates are consistent with each other, but contain some error compared to the actual distributions due to the simplification of the identification model. Moving forwards, there will are a number of aspects worth considering. Recommendations and discussion regarding the modelling approach are in Section 7.1.1, and ideas regarding the estimation approach are covered in Section 7.1.2.

7.1.1 Model Structure and Uncertainties

The non-linear single track model was the most complex model considered here. It is however still a very simplified model of a real car. The model complexity could be increased further by using a planar two track model like the one illustrated in Figure 2.4, or by using a multibody model. The ultimate level of complexity would be to use data from a real car. Increasing the model complexity would come with several new challenges to solve. Identifying a linear model would mean a larger simplification error. Changing the identification model to a more complex non-linear one could potentailly help to reduce the simplification error, but such an approach would also come with computational challenges. In the case of real measurements, these would be corrupted by noise and additionally, slip angles are difficult to measure or observe in real life, meaning that slip angle data would likely not be available as a part of the basis for identification. Investigating these challenges closer would be one of the

most crucial next steps.

It was observed in this project that the mean output trajectories were largely unaffected by increasing noise intensity, however the added noise did have a significant effect on the measured output variance. Noise reduction in post processing would perhaps be the most intuitive way to deal with the noise. A potential alternative may be to model the noise in the PCE model, which could possibly also be a way to identify the noise characteristics of sensors themselves. Modelling white noise processes using PCE is still an open challenge at the time of writing however.

A real system would also likely have more uncertainties than those which were considered here. Therefore another natural progression of this project would be to investigate what happens when the number of uncertainties is increased. Identifiability issues may become greater when more uncertainties are included. Further, in this project, neglecting insignificant uncertainties proved to be a viable approach, however, when several individually insignificant uncertainties are neglected, their cumulative influence may be too great to neglect. Further investigation will be required to find out how viable the methods presented in this thesis are for more complex applications. Depending on the results, further methods may need to be developed to deal with larger sets of uncertainties. One may also note that some uncertainties ought to be related to each other. For example, in this case, the load and CoG position were completely independent of each other. In reality, it would most likely be more accurate to model the CoG position as being dependent on the load, as a change in mass distribution is what shifts the CoG position.

One weakness however of the used approach which would become more of an issue as the number of uncertainties increases, is that matrices of the PCE system need to be computed every time the probability distribution parameters change. In the identification scenario, this means that every evaluation of the cost function with a different set of parameters requires the augmented system matrices to be computed. As the number of random variables increases, the number of states in the augmented system increases combinatorically. The time required to compute the augmented system matrices increases along with the number of state variables. One avenue to explore would be the possibility of computing the augmented system matrices symbolically, allowing for new parameter values to simply be substituted in.

In order to potentially mitigate some of the identifiability problems, it may be possible to use the observability- and sensitivity analyses. Both the non-linear observability matrix and sensitivity, as presented in Chapters 3 and 4 respectively, are input dependent. Given this fact, it may be possible to find an input signal to maximise the observability or sensitivity of certain parameters. For example, the first order sensitivity against parameter θ_k may be maximised as

$$\boldsymbol{u}(t) = \arg\max_{\boldsymbol{u}(t)} \sum_{k=1}^{N} SU_k(t), \tag{7.1}$$

to get an input signal which excites the system in such a way that the each parameter has as large of an impact on the variance as possible. This could potentially allow

for more optimal experiment design. Using feedback control in an experiment may also allow time variant phenomena such as the wind to have a larger influence on the system, though this would have to be investigated further.

In the approach used, distribution parameters of pre-defined distribution types were identified. When structuring the model to be identified, one has to pick which type of distribution each uncertainty is expected to follow. Doing this was simple in this project, as the baseline system was perfectly known, however a challenge for engineers applying these methods to unknown systems would be to establish how each uncertainty in the system should be modelled, i.e. if the values may be normally or uniformly distributed. It would therefore be interesting to investigate the possibility of not only identifying the distribution parameters, but also the type of distribution. Along with this, considering more types of distributions than the normal and uniform distributions considered in this project would be important.

7.1.2 Estimation and Cost Function

The main focus of this project was to investigate the viability of estimating probability distributions from measured data. To do this, the cost function (5.25) was minimised. To minimise this cost function, the MATLAB function `fminunc` was used with the quasi-Newton method option. This proved to work well when the initial guess deviation was within 25%, however the estimates produced worsened beyond 40% deviation. It is possible that other optimisation approaches may be more suited to situations with poor initial guesses, particularly to avoid problems such as finding local minima. Further investigation is necessary to learn about the potential of different optimisation strategies.

Different weighting schemes were used in this project, with the distance-based weighting scheme (5.28) proving to provide a slight reduction in the estimation error. The distance-based cost weighting scheme (5.28) provided a small advantage in this project, but was only available since the parameter values were all known beforehand, but this information will not be available in a real case. With this fact in mind, finding alternative weighting schemes and/or cost function formulations and gaining insight into their effects on the estimates is important in order to ensure that the proposed identification approach works in more general cases.

7.2 Control with PCE System

From the testing of controllers, there was no difference between the SLQR and LQR when simulated on the linear system. There is also little to no difference when comparing the two controllers on the non-linear system. This comes as no surprise, given that the two control gains are relatively similar, except for the gain on the slip angle, which is the only state variable where there is a noticeable difference when simulating on the non-linear system. Although the influence of such a small difference in slip angle on the other states appears to be minimal.

These results suggest no significant benefit noticed in using the SLQR over the LQR

in terms of stochastic properties, neither does it appear to have provided any benefit to account for the time variant disturbance in the controller synthesis, although this may in part be due to the its zero mean and low influence on the system, as seen in the sensitivity analysis. It is possible that a more severe disturbance may have a different gove different results.

However in parallel to this project, Gallant [45] conducted an investigation with a heavier focus on control using a similar system and test case. In contrary to the findings of this thesis, their findings suggest that stochastic control design using PCE does have the potential to provide a benefit, as it becomes possible to control the variance characteristics in the design stage. Delivering exactly this type of benefit is the goal of the SAFER project, to reduce the need for testing as such considerations can be made in the design stage.

The discrepancy between the results of the two projects may lay in the approaches used, as Gallant [45] used a slightly different model, and a different approach to solving the SLQR optimisation problem (4.64). The exact reasons however remain unknown and would require more investigation into the control case.

Both in this work and that of Gallant [45], the second SLQR proposition (4.66) was used, which is in implementation indistinguishable from a regular LQR. Implementation of the other propositions would be more challenging, as they would all require either some way of estimating the augmented state $\boldsymbol{X}(t)$ or the random variable $\boldsymbol{\xi}$ or both. Work has been done to derive observers to estimate the expanded system's state vector [60], however the current methods requires a measurement of the mean trajectory, which is most likely not measurable from a single instance of the system. However, these challenges can be overcome with relative ease in a simulation environment, and it may be of interest to study whether or not there are any significant benefits to the other SLQR propositions over (4.66).

7.3 PCE and KLE Implementation

As already mentioned, expanding the existing framework for non-linear systems stands to reason. Additionally, implementing methods to calculate higher order moments from the PCE state vector would be a useful addition. Although first and second order moments may be of primary interest during control design, and appear to be sufficient for identification, higher order moments could be of interest for evaluation of the output of open- and closed loop systems.

The KLE implementation in this project creates a model valid only over a limited time horizon. Alternative implementation methods may be able to remove this issue. It was noted during this project that the eigenfunctions of the Gaussian process modelled tended to have a periodic appearance with increasing frequency as can be seen in Figure 7.1. Computing the KLE of the side wind using $N_{\text{GLQ,KLE}} = 350$ and $p_c = 0.95$ over the time span 0 s to 10 s results in five eigenfunctions, which have all been plotted in the figure. Note that the grey areas represent where the KLE is invalid. It may be possible to characterise the pattern of these eigenfunctions to

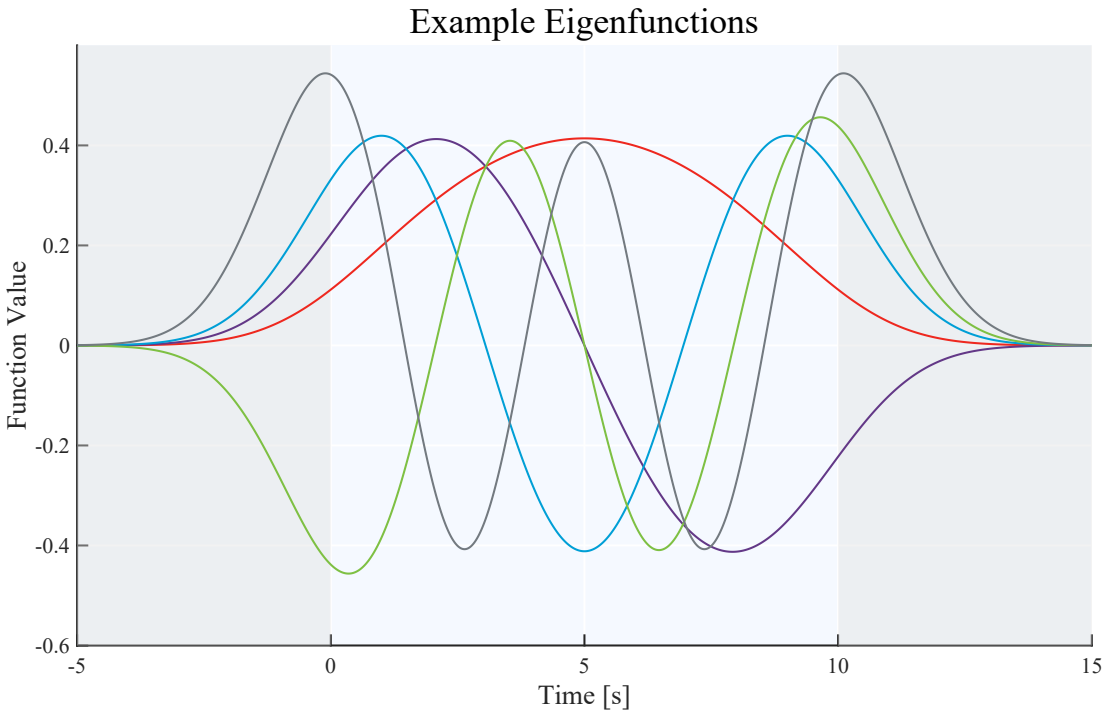

Figure 7.1: Examples of the eigenfunctions computed for the Gaussian process considered in this project using $N_{\mathrm{GLQ,KLE}} = 350$ and $p_c = 0.95$ over the time span 0 s to 10 s.

artificially extend them indefinitely through some approximation. One constraint being that the sum of all eigenfunctions cannot be periodic, as that would result in periodicity in the random process approximation.

8

Conclusion

The objective of this project was to investigate the possibility of estimating the probability distributions of system uncertainties and disturbances, as well as to investigate how model simplification would influence the estimates. Identifying distribution parameters under ideal conditions, with noiseless recorded data and an identification model structure which perfectly models reality, has been shown to be possible to achieve with acceptable accuracy. Introducing noise in the measured data was shown to increase the variance computed from the measured data, which negatively affected the ability to estimate the probability distributions of the uncertainties.

When the identification model structure is a simplified representation of reality, the model error causes the identification of the probability distributions to lose accuracy. From the results of this study, the model error appears to be input-specific. Additionally, the estimation error appears to be consistent, meaning that the estimates could potentially be corrected by some constants. The attempts to mitigate the model error using various cost functions in this project proved to be marginally effective, although the DST cost function was shown to be consistently better than both the STD and INP cost functions. This result provides an indication that it may be possible to further compensate for the model error using a cost function weighting scheme, meaning it would be recommended to investigate such possibilities further.

Regarding control using the SLQR, the results from this project are quite different to those from Gallant [45], in spite of the control cases and methods used being relatively similar. Therefore, the results pertaining to control acquired within this thesis must be deemed to be inconclusive, requiring further research.

Overall, the ability to identify probability distributions from measured data could be valuable, particularly when data can be acquired from large fleets of vehicles, to keep models up to date. The information could be used to perform testing of systems in simulation prior to release, with accurate data. Further research is necessary to adapt the methods developed in this thesis to more complex applications. As the results of this thesis show that the approach of using PCE with system identification to estimate the probability distributions of uncertainties fundamentally works.

Bibliography

[1] Economic Commission for Europe of the United Nations (UN/ECE), *Regulation No 79 on Uniform provisions concerning the approval of vehicles with regard to steering equipment [2018/1947]*, 2018. [Online]. Available: https://eur-lex.europa.eu/legal-content/EN/TXT/PDF/?uri=CELEX:42018X1947&from=EN.

[2] International Organization for Standardization, *Road vehicles — Safety of the intended functionality, ISO 21448:2022*, Tokyo, 2022. [Online]. Available: https://www.iso.org/standard/77490.html.

[3] Economic Commission for Europe of the United Nations (UN/ECE), *Regulation No 157 on Uniform provisions concerning the approval of vehicles with regards to Automated Lane Keeping Systems [2021/389]*, 2021. [Online]. Available: https://eur-lex.europa.eu/legal-content/EN/TXT/PDF/?uri=CELEX:42021X0389&from=EN.

[4] E. Stewart, "Self-driving cars have to be safer than regular cars. The question is how much.," *Vox*, May 17, 2019. [Online]. Available: https://www.vox.com/recode/2019/5/17/18564501/self-driving-car-morals-safety-tesla-waymo (visited on 11/16/2022).

[5] A. Barbu and S.-C. Zhu, *Monte Carlo Methods*. Singapore: Springer Singapore, 2020.

[6] C. Graham and D. Talay, *Stochastic Simulation and Monte Carlo Methods, Mathematical Foundations of Stochastic Simulation*. Heidelberg, Baden-Württemberg, Germany: Springer-Verlag Berlin, 2013.

[7] M. Plançon and T. Prest, "Exact Lattice Sampling from Non-Gaussian Distributions," in *Public-Key Cryptography – PKC 2021*, J. A. Garay, Ed., Cham: Springer International Publishing, 2021, pp. 573–595, ISBN: 978-3-030-75245-3.

[8] R. G. Ghanem and P. D. Spanos, *Stochastic Finite Elements, A Spectral Approach*. New York, USA: Springer-Verlag New York, 1991.

[9] J. R. Fisher, "Stability Analysis and Control of Stochastic Dynamic Systems Using Polynomial Chaos," Ph.D. dissertation, Department of Aerospace Engineering, Texas AM University, College Station, 2008.

[10] J. Bezdek, "Fuzzy models—What are they, and why? [Editorial]," *Fuzzy Systems, IEEE Transactions on*, vol. 1, pp. 1–6, Mar. 1993. DOI: 10.1109/TFUZZ.1993.6027269.

[11] "Fuzzy Estimation," in *Simulating Continuous Fuzzy Systems*. Berlin, Heidelberg: Springer Berlin Heidelberg, 2006, pp. 21–32, ISBN: 978-3-540-31227-7.

DOI: 10.1007/3-540-31227-7_3. [Online]. Available: https://doi.org/10.1007/3-540-31227-7_3.

[12] L. K. Mitropoulos *et al.*, "A Fuzzy and a Monte Carlo simulation approach to assess sustainability and rank vehicles in urban environment," *Transportation Research Procedia*, vol. 24, pp. 296–303, 2017, 3rd Conference on Sustainable Urban Mobility, 3rd CSUM 2016, 26 – 27 May 2016, Volos, Greece, ISSN: 2352-1465. DOI: https://doi.org/10.1016/j.trpro.2017.05.121. [Online]. Available: https://www.sciencedirect.com/science/article/pii/S2352146517304040.

[13] E. Jacquelin *et al.*, "Polynomial chaos expansion with fuzzy and random uncertainties in dynamical systems," in *Proceedings of ISMA2016 including USD2016*, 2016, pp. 4295–4306.

[14] V. Ivanov, "A review of fuzzy methods in automotive engieering applications," *European Transport Research Review*, vol. 7, Aug. 2015. DOI: 10.1007/s12544-015-0179-z.

[15] D. Xiu *et al.*, "Performance Evaluation of Generalized Polynomial Chaos," in *Computational Science — ICCS 2003*, P. M. A. Sloot *et al.*, Eds., Berlin, Heidelberg: Springer Berlin Heidelberg, 2003, pp. 346–354, ISBN: 978-3-540-44864-8.

[16] K. K. Sepahvand, S. Marburg, and H.-j. Hardtke, "Uncertainty Quantification in Stochastic Systems Using Polynomial Chaos Expansion," *International Journal of Applied Mechanics*, vol. 02, Apr. 2012. DOI: 10.1142/S1758825110000524.

[17] G. Kewlani, J. Crawford, and K. Iagnemma, "A polynomial chaos approach to the analysis of vehicle dynamics under uncertainty," *Vehicle System Dynamics*, vol. 50, no. 5, pp. 749–774, 2012. DOI: 10.1080/00423114.2011.639897.

[18] E. Asaad *et al.*, "Development of a Torque Vectoring System for a 4WD Electric Formula Student Car," Bachelor's thesis, Department of Electrical Engineering, Chalmers University of Technology, Göteborg, 2020.

[19] D. Schramm, M. Hiller, and R. Bardini, *Vehicle Dynamics, Modelling and Simulation*. Berlin: Springer-Verlag Berlin, 2014.

[20] K. Georg, "Model Predictive Control of Autonomous Vehicles at the Limits of Vehicle Dynamics," Master's thesis, Institut für Systemtheorie und Regelungstechnik, Universität Stuttgart, Stuttgart, 2019.

[21] H. Richardson, "Modelling the Evolution of Tyre Performance in a Motorsport Application, Analysis of effects on vehicle performance in a real-time simulation environment," Master's thesis, Department of Applied Mechanics, Chalmers University of Technology, Göteborg, 2017.

[22] H. B. Pacejka and I. Besselink, *Tire and Vehicle Dynamics*, Third Edition. Oxford: Butterworth-Heinemann, 2012, ISBN: 978-0-08-097016-5.

[23] Mathworks. (Unknown). "Tire-Road Interaction (Magic Formula)," [Online]. Available: https://de.mathworks.com/help/sdl/ref/tireroadinteractionmagicformula.html (visited on 10/24/2022).

[24] R. Bruder, "Model-Based Trajectory Planning for Autonomous Vehicles Subject to Uncertainty," Master's thesis, Institut für Systemtheorie und Regelungstechnik, Universität Stuttgart, Stuttgart, 2019.

[25] E. Bakker, L. Nyborg, and H. B. Pacejka, "Tyre Modelling for Use in Vehicle Dynamics Studies," *SAE Transactions*, vol. 96, pp. 190–204, 1987, ISSN: 0096736X.

[26] M. Veneri and M. Massaro, "The effect of Ackermann steering on the performance of race cars," *Vehicle System Dynamics*, vol. 59, no. 6, pp. 907–927, 2021. DOI: 10.1080/00423114.2020.1730917. eprint: https://doi.org/10.1080/00423114.2020.1730917. [Online]. Available: https://doi.org/10.1080/00423114.2020.1730917.

[27] O. Nelles, *Nonlinear System Identification*. Berlin, Heidelberg: Springer-Verlag Berlin Heidelberg, 2001.

[28] K. J. Keesman, *System Identification*. London: Springer London, 2011.

[29] S. Gros and B. Egardt, *Modelling and Simulation, Lecture notes for the chalmers course ess101*, Göteborg, 2020.

[30] R. Singh, "Identification of a Dynamic Model for a Superconductor Based Magnetic Levitation Module," Student's thesis, Institute for System Dynamics, University of Stuttgart, Stuttgart, Baden-Württemberg, Germany, 2022.

[31] A. P. Browning *et al.*, "Identifiability analysis for stochastic differential equation models in systems biology," *The Royal Society*, 2020. DOI: 10.1098/rsif.2020.0652.

[32] E. Walter, *Identifiability of State Space Models, with applications to transformation systems*. Berlin: Springer Berlin, 1982.

[33] Y. Lecourtier, E. Walter, and P. Bertrand, "Identifiability Testing for State-Space Models," *IFAC Proceedings Volumes*, vol. 15, no. 4, 887–892, 1982, 6th IFAC Symposium on Identification and System Parameter Estimation, Washington USA, 7-11 June, ISSN: 1474-6670. DOI: https://doi.org/10.1016/S1474-6670(17)63106-9. [Online]. Available: https://www.sciencedirect.com/science/article/pii/S1474667017631069.

[34] E. Walter and L. Pronzato, "On the Identifiability and Distinguishability of Nonlinear Parametric Models," *Mathematics and Computers in Simulation*, vol. 42, no. 2, pp. 125–134, 1996, Mathematical Modelling and Simulation in Agriculture and Bio-Industries Proceedings of the 1st IMACS-IFAC Symposium Msu2SABI, ISSN: 0378-4754. DOI: https://doi.org/10.1016/0378-4754(95)00123-9. [Online]. Available: https://www.sciencedirect.com/science/article/pii/0378475495001239.

[35] S. Audoly *et al.*, "Global Identifiability of Nonlinear Models of Biological Systems," *IEEE Transactions on Biomedical Engineering*, vol. 48, no. 1, pp. 55–65, 2001. DOI: 10.1109/10.900248.

[36] A. F. Villaverde, "Observability and Structural Identifiability of Nonlinear Biological Systems," *Complexity*, vol. 2019, 2019, ISSN: 1076-2787. DOI: 10.1155/2019/8497093.

[37] T. Glad and L. Ljung, *Control Theory, Multivariable and Nonlinear Methods*. London: Taylor & Francis, 2000.

[38] N. Wiener, "The Homogeneous Chaos," *American Journal of Mathematics*, vol. 60, no. 4, pp. 897–936, 1938. [Online]. Available: https://doi.org/10.2307/2371268.

[39] D. Xiu and G. E. Karniadakis, "The Wiener–Askey Polynomial Chaos for Stochastic Differential Equations," *SIAM Journal on Scientific Computing*, vol. 24, no. 2, pp. 619–644, 2002. DOI: 10.1137/S1064827501387826. eprint: https://doi.org/10.1137/S1064827501387826. [Online]. Available: https://doi.org/10.1137/S1064827501387826.

[40] F. E. Harris, "Chapter 11 - General Vector Spaces," in *Mathematics for Physical Science and Engineering*, F. E. Harris, Ed., Boston: Academic Press, 2014, pp. 397–425, ISBN: 978-0-12-801000-6. DOI: https://doi.org/10.1016/B978-0-12-801000-6.00011-0. [Online]. Available: https://www.sciencedirect.com/science/article/pii/B9780128010006000110.

[41] T. Albrecht, "Polynomial Chaos Expansion mit räumlich adaptiven Sparse Grids," Bachelor's thesis, Institut für Parallelle und Verteilte Systeme, Universität Stuttgart, Stuttgart, 2020.

[42] Wikipedia. (2022). "Hermite Polynomials," [Online]. Available: https://en.wikipedia.org/wiki/Hermite_polynomials (visited on 12/08/2022).

[43] ——, (2022). "Legendre Polynomials," [Online]. Available: https://en.wikipedia.org/wiki/Legendre_polynomials (visited on 12/08/2022).

[44] B. Sudret. (2016). "Uncertainty propagation using polynomial chaos expansions," [Online]. Available: https://www.uni-weimar.de/fileadmin/user/fak/bauing/professuren_institute/grk1462/SummerSchool2016/Sudret-WeimarPCE.pdf.

[45] M. Gallant, *Stochastic Optimal Control for the Lateral Motion Control: Design and Analysis of Generalizability*, Unpublished, Internship Report, Oct. 31, 2022.

[46] T. Lefebvre, "On Moment Estimation From Polynomial Chaos Expansion Models," *IEEE Control Systems Letters*, vol. 5, no. 5, pp. 1519–1524, 2021. DOI: 10.1109/LCSYS.2020.3040851.

[47] P. Holmes *et al.*, "Galerkin projection," in *Turbulence, Coherent Structures, Dynamical Systems and Symmetry*, 2nd ed., ser. Cambridge Monographs on Mechanics. Cambridge: Cambridge University Press, 2012, pp. 106–129. DOI: 10.1017/CBO9780511919701.006.

[48] Wikipedia. (2022). "Hadamard product (matrices)," [Online]. Available: https://en.wikipedia.org/wiki/Hadamard_product_(matrices) (visited on 12/01/2022).

[49] J. Fisher and R. Bhattacharya, "Linear Quadratic Regulation of Systems with Stochastic Parameter Uncertainties," *Automatica*, vol. 45, no. 12, pp. 2831–2841, 2009, ISSN: 0005-1098. DOI: https://doi.org/10.1016/j.automatica.2009.10.001. [Online]. Available: https://www.sciencedirect.com/science/article/pii/S0005109809004622.

[50] B. Sudret, "Global Sensitivity Analysis Using Polynomial Chaos Expansions," *Reliability Engineering System Safety*, vol. 93, no. 7, 964–979, 2008, Bayesian Networks in Dependability, ISSN: 0951-8320. DOI: https://doi.org/10.1016/j.ress.2007.04.002. [Online]. Available: https://www.sciencedirect.com/science/article/pii/S0951832007001329.

[51] Mathworks. (Unknown). "ode45," [Online]. Available: https://de.mathworks.com/help/matlab/ref/ode45.html (visited on 11/04/2022).

[52] K. Schmidt, "Störgrößenkompensation und Strahlformung in adaptiven Hochleistungslasern durch deformierbare Spiegel," Ph.D. dissertation, Institut für Systemdynamik, Universität Stuttgart, Stuttgart, 2020.

[53] F. Bornemann, "On the Numerical Evaluation of Fredholm Determinants," *Mathematics of Computation*, vol. 79, pp. 871–915, 2010. DOI: 10.1090/S0025-5718-09-02280-7.

[54] Wikipedia. (2021). "Kullback-Leibler-Divergenz," [Online]. Available: https://de.wikipedia.org/wiki/Kullback-Leibler-Divergenz (visited on 11/11/2022).

[55] ——, (2022). "Wasserstein-metric," [Online]. Available: https://en.wikipedia.org/wiki/Wasserstein_metric (visited on 11/11/2022).

[56] L. Rüschendorf, *Wasserstein-metric*, Freiburg.

[57] Mathworks. (Unknown). "fminunc," [Online]. Available: https://de.mathworks.com/help/optim/ug/fminunc.html (visited on 01/10/2022).

[58] Trafikverket, *Råd för vägars och gators utformning*, 2012.

[59] Forschungsgesellschaft für Straßen- und Verkehrswesen, *Richtlinien für die Anlage von Autobahnen*, 2008.

[60] A. H. C. Smith, A. Monti, and F. Ponci, "Indirect Measurements via a Polynomial Chaos Observer," *IEEE Transactions on Instrumentation and Measurement*, vol. 56, no. 3, pp. 743–752, 2007. DOI: 10.1109/TIM.2007.894914.

A

Measured Data

The measured data from the simulations are presented in this Appendix. Data generated using the LST model are presented in Section A.1 and the data generated using the NLST model are presented in Section A.2.

A.1 LST Model Data

Figures A.1, A.2, A.3, A.4, A.5, A.6, A.7, A.8, A.9, A.10, and A.11 all display the mean of each measured signals as well as the area containing all outputs up to three standard deviations away from the mean from the simulations using the LST model. The noise intensity is increasing in each figure.

A.2 NLST Model Data

Figures A.12, A.13, A.14, A.15, A.16, A.17, A.18, A.19, A.20, A.21, and A.22 all display the mean of each measured signals as well as the area containing all outputs up to three standard deviations away from the mean from the simulations using the NLST model. The noise intensity is increasing in each figure.

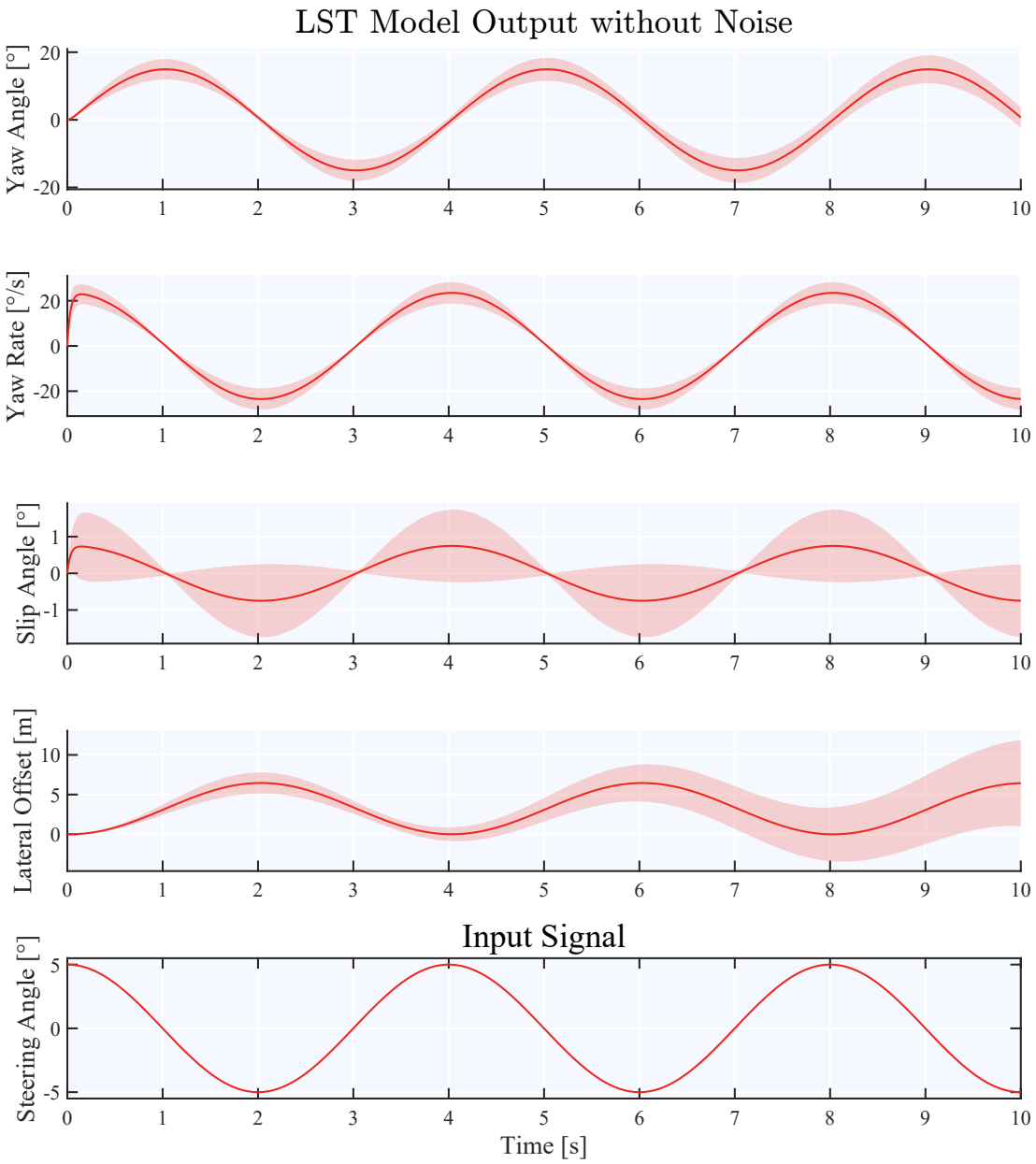

Figure A.1: Data From the LST model with $A = 0$.

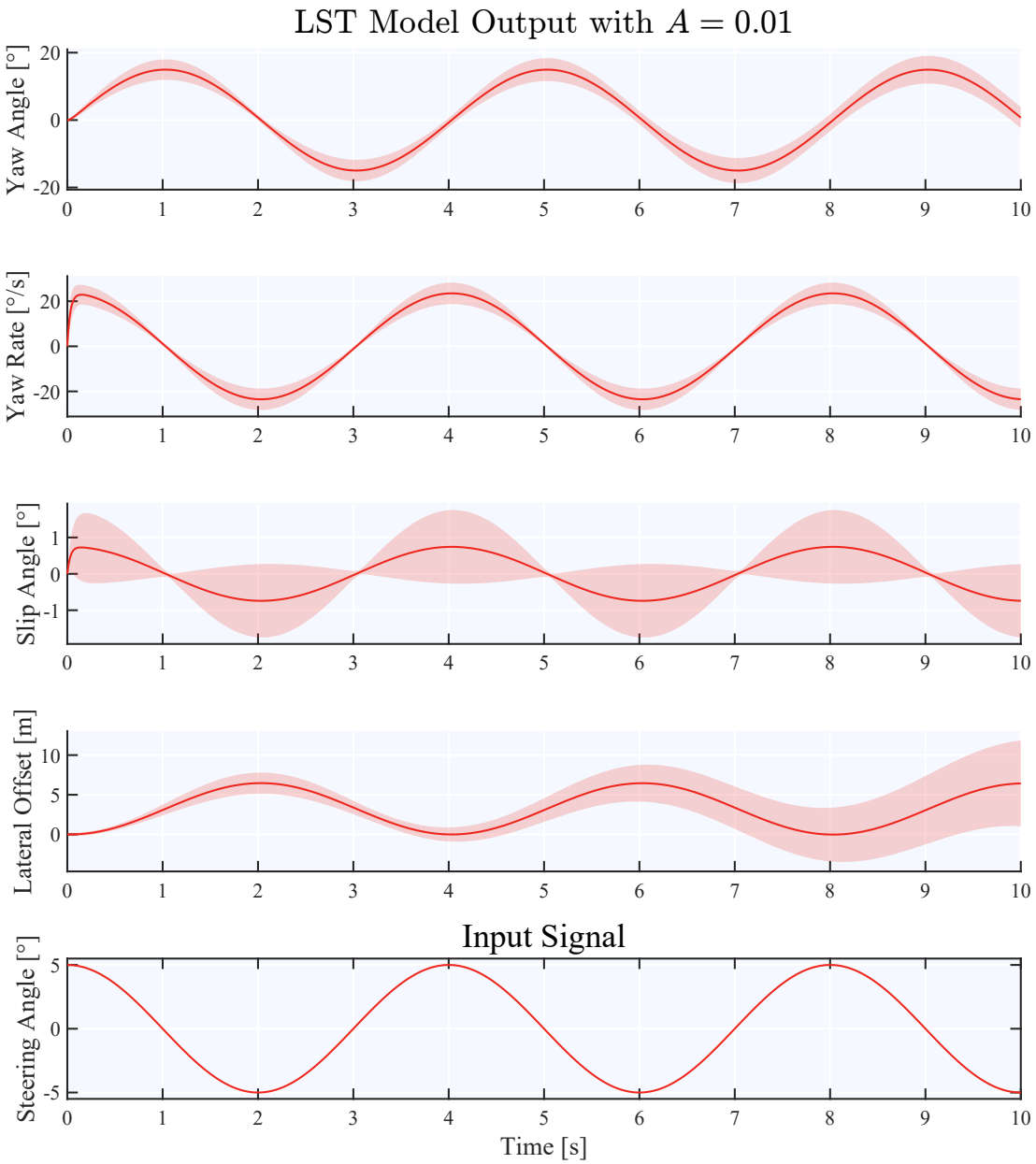

Figure A.2: Data From the LST model with $A = 0.01$.

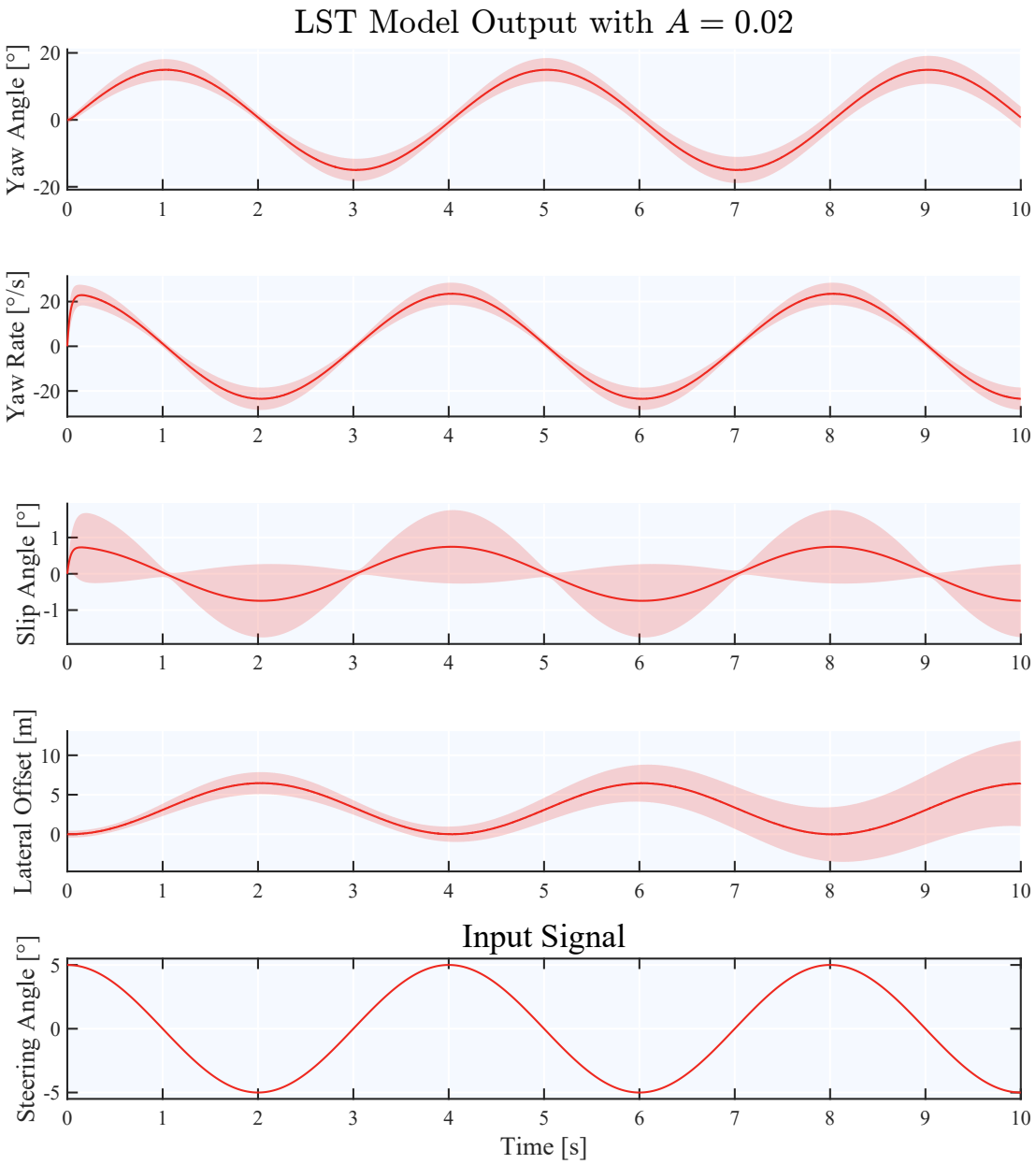

Figure A.3: Data From the LST model with $A = 0.02$.

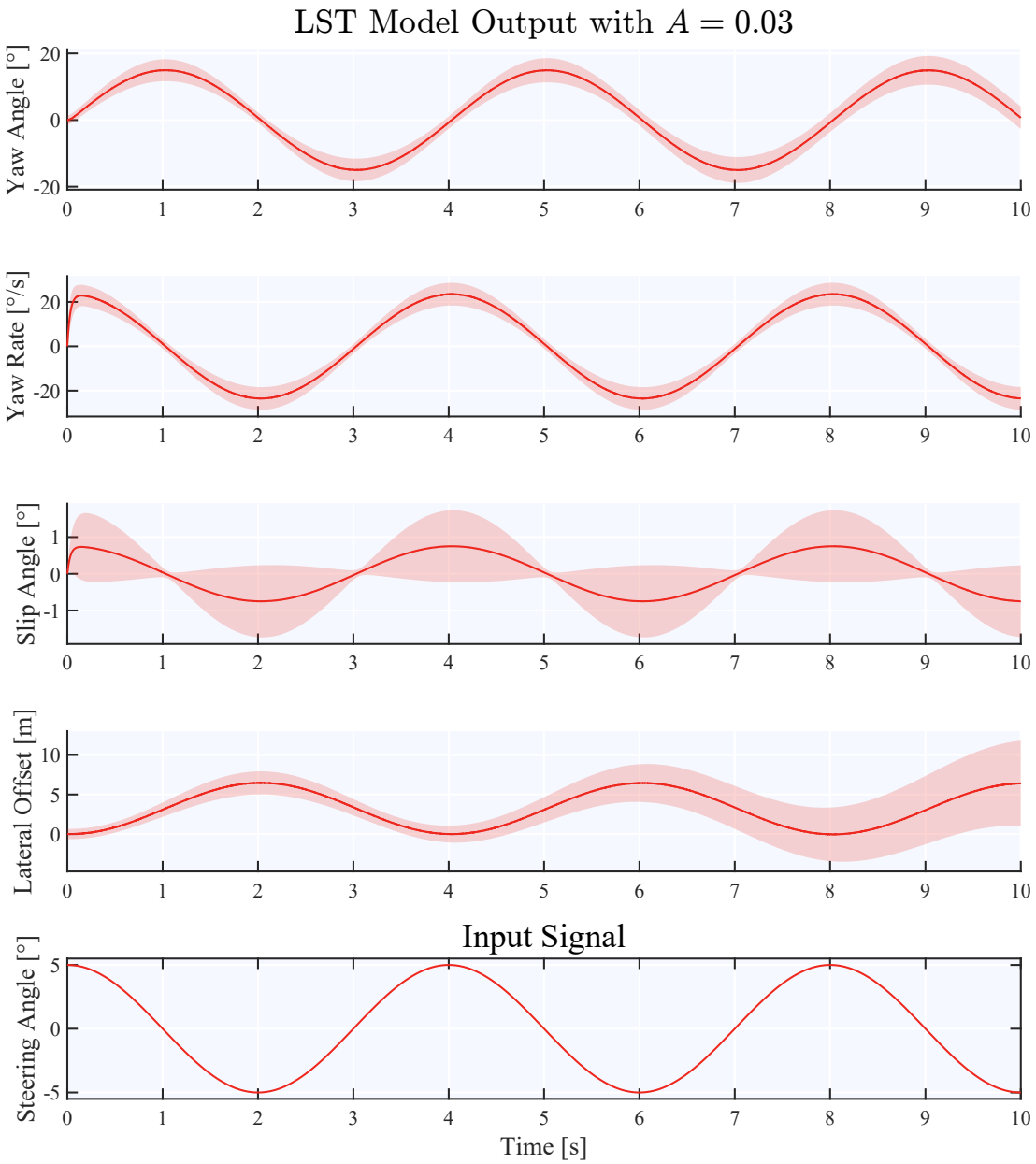

Figure A.4: Data From the LST model with $A = 0.03$.

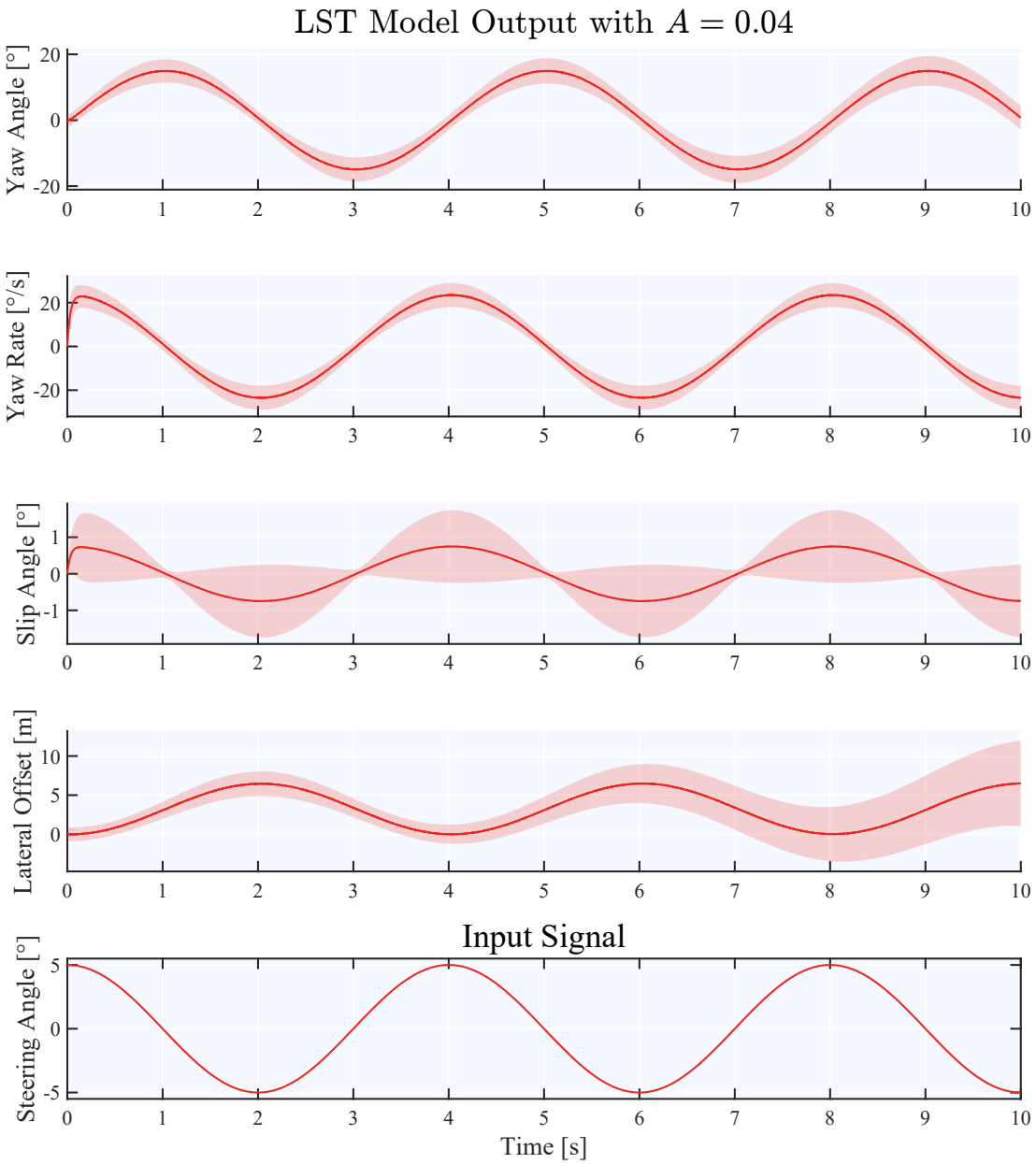

Figure A.5: Data From the LST model with $A = 0.04$.

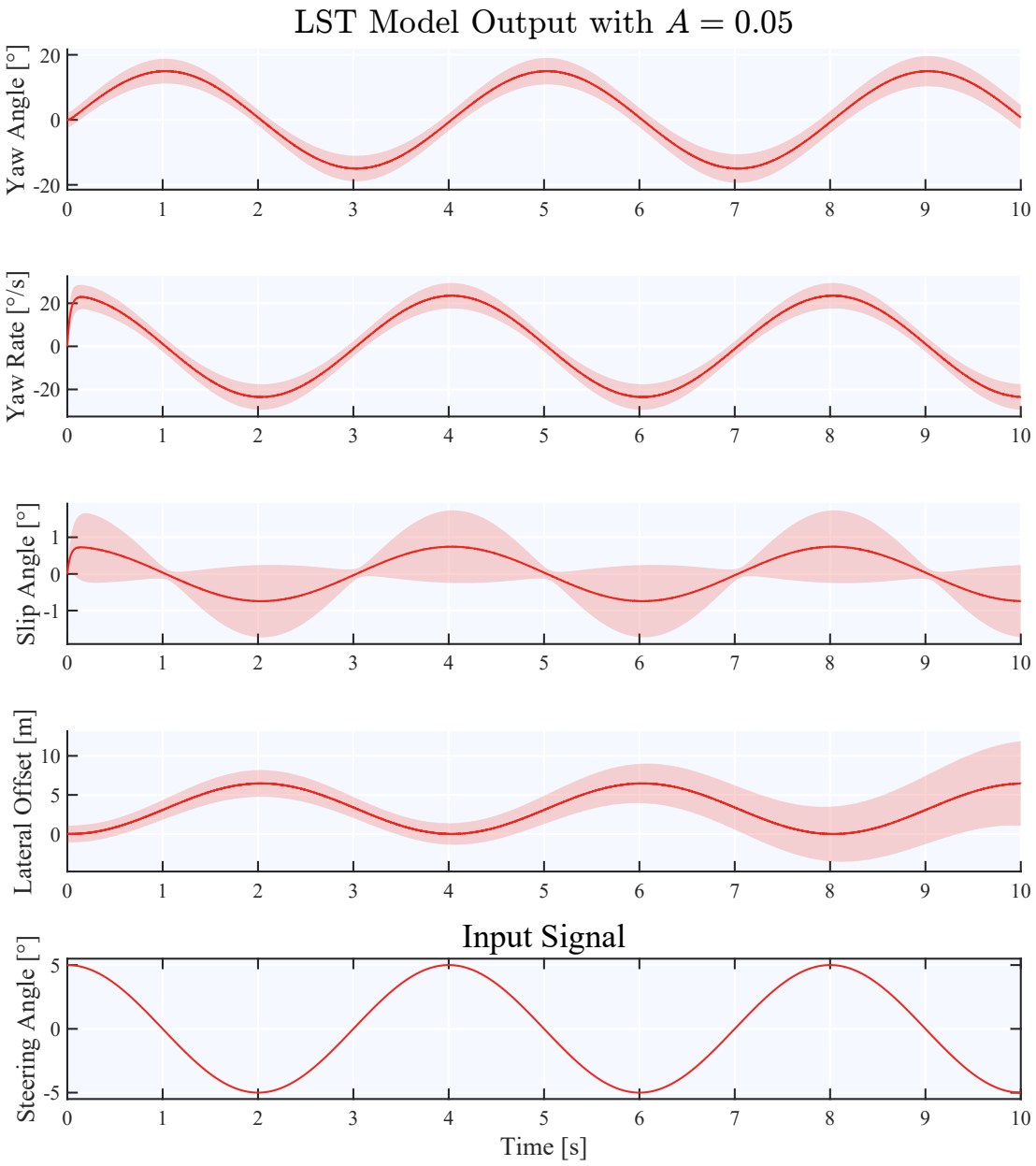

Figure A.6: Data From the LST model with $A = 0.05$.

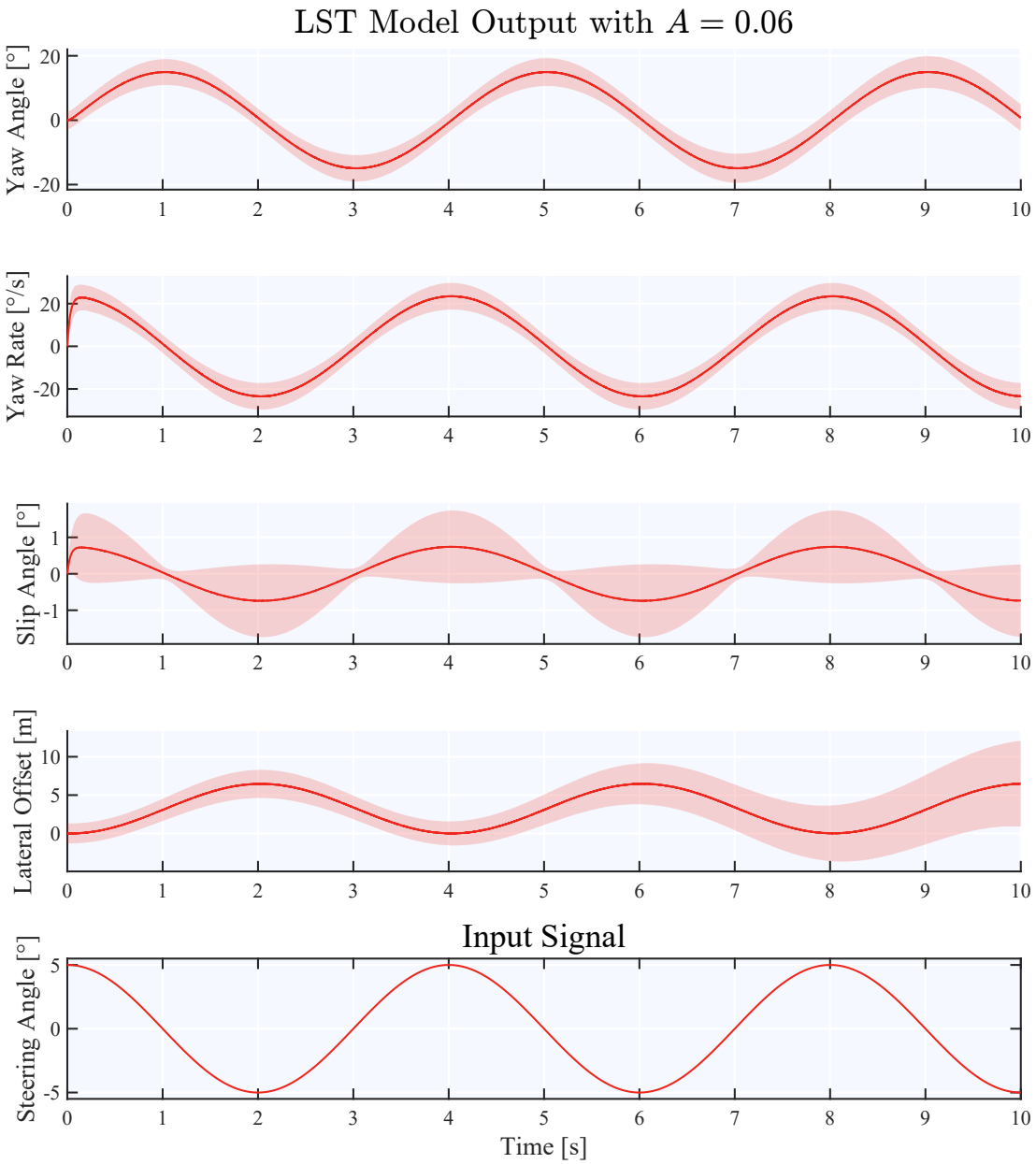

Figure A.7: Data From the LST model with $A = 0.06$.

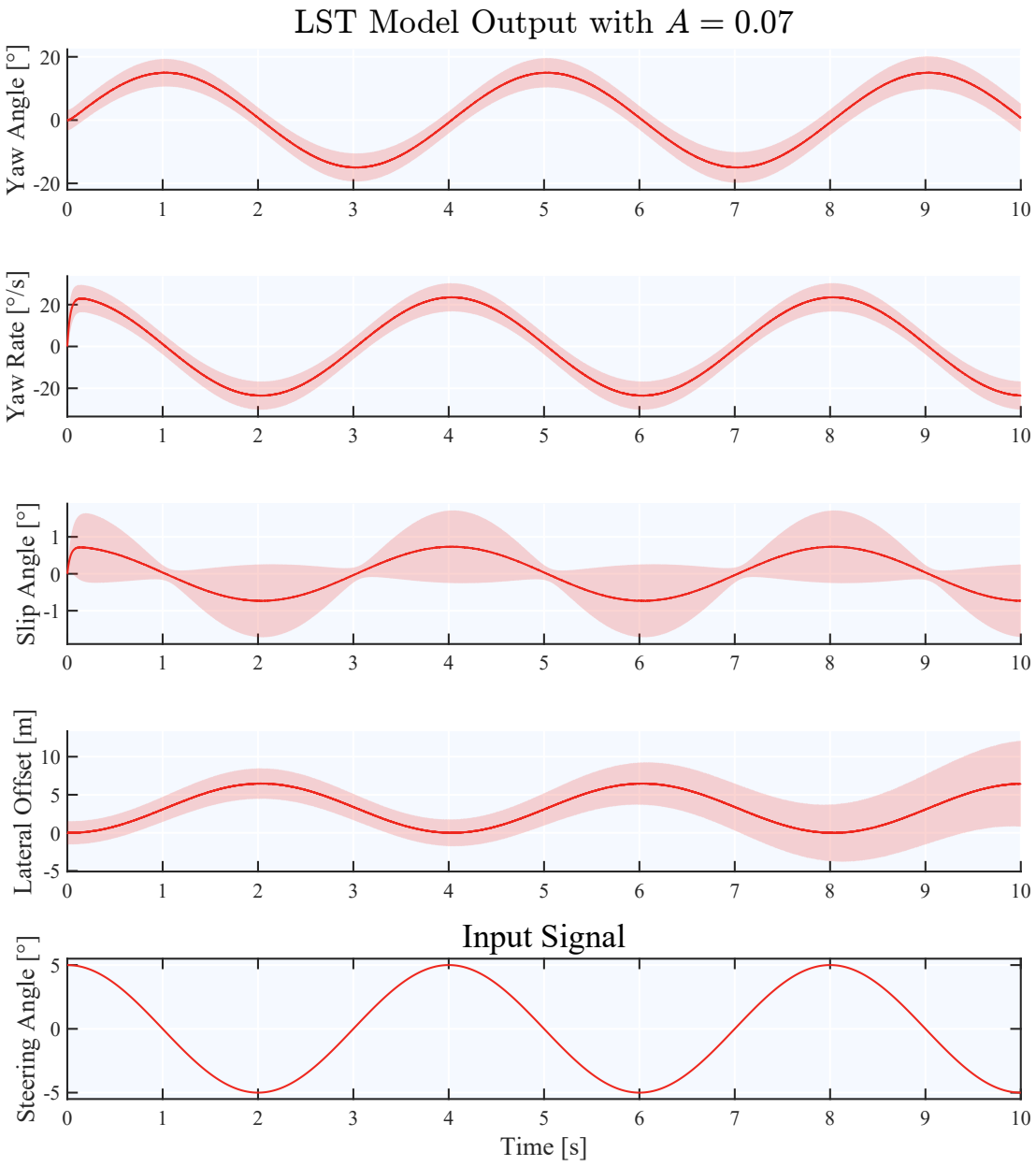

Figure A.8: Data From the LST model with $A = 0.07$.

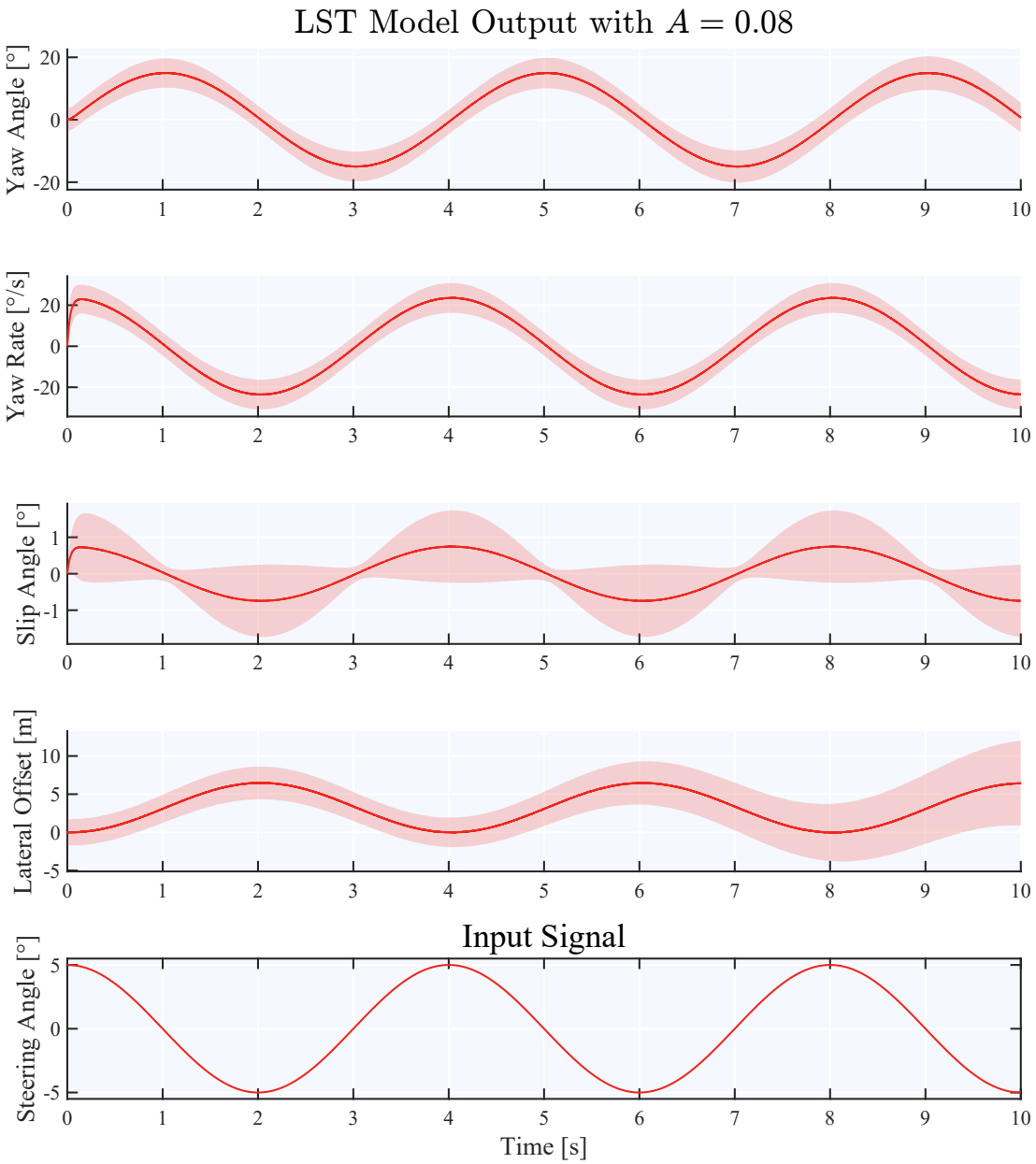

Figure A.9: Data From the LST model with $A = 0.08$.

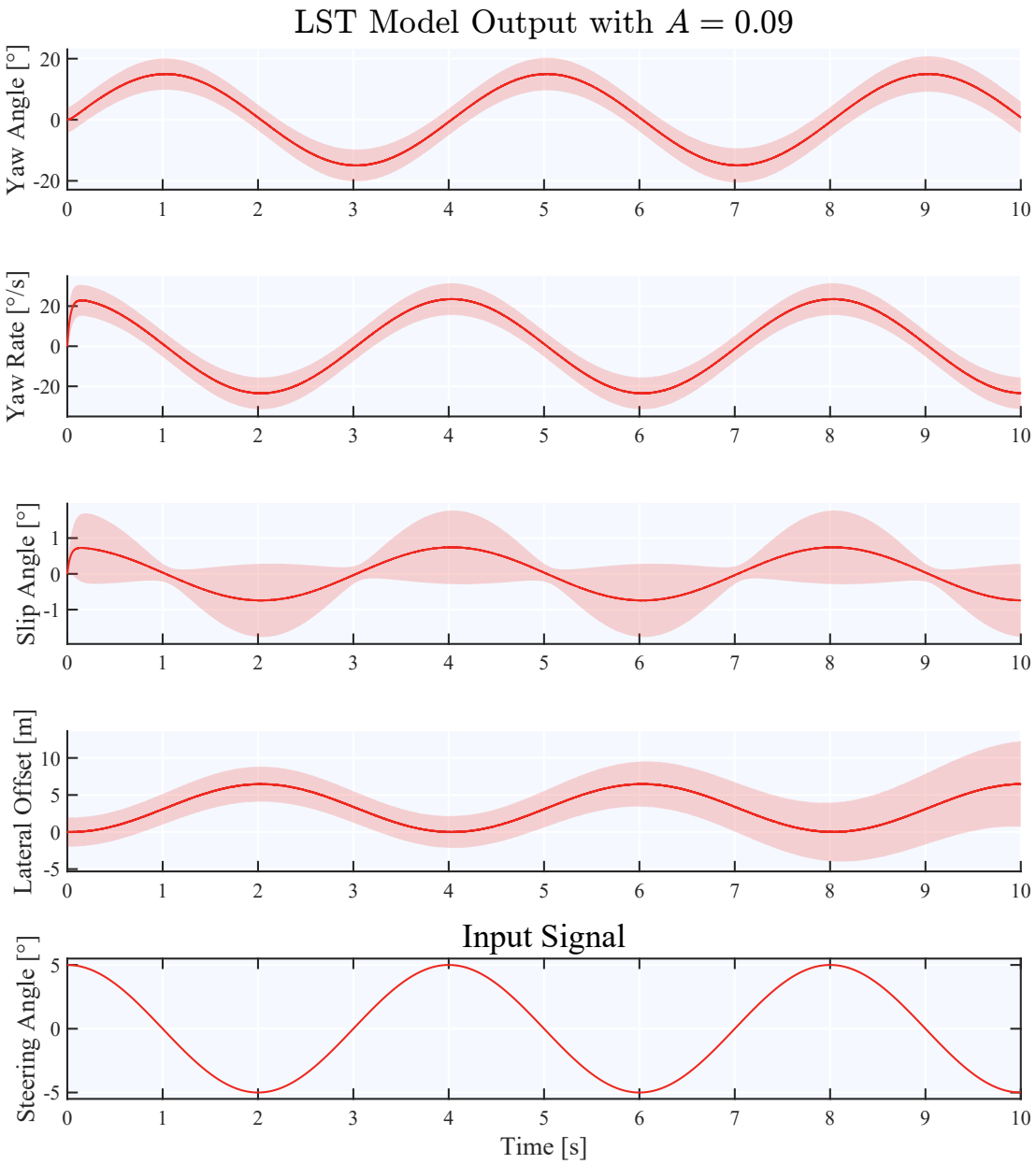

Figure A.10: Data From the LST model with $A = 0.09$.

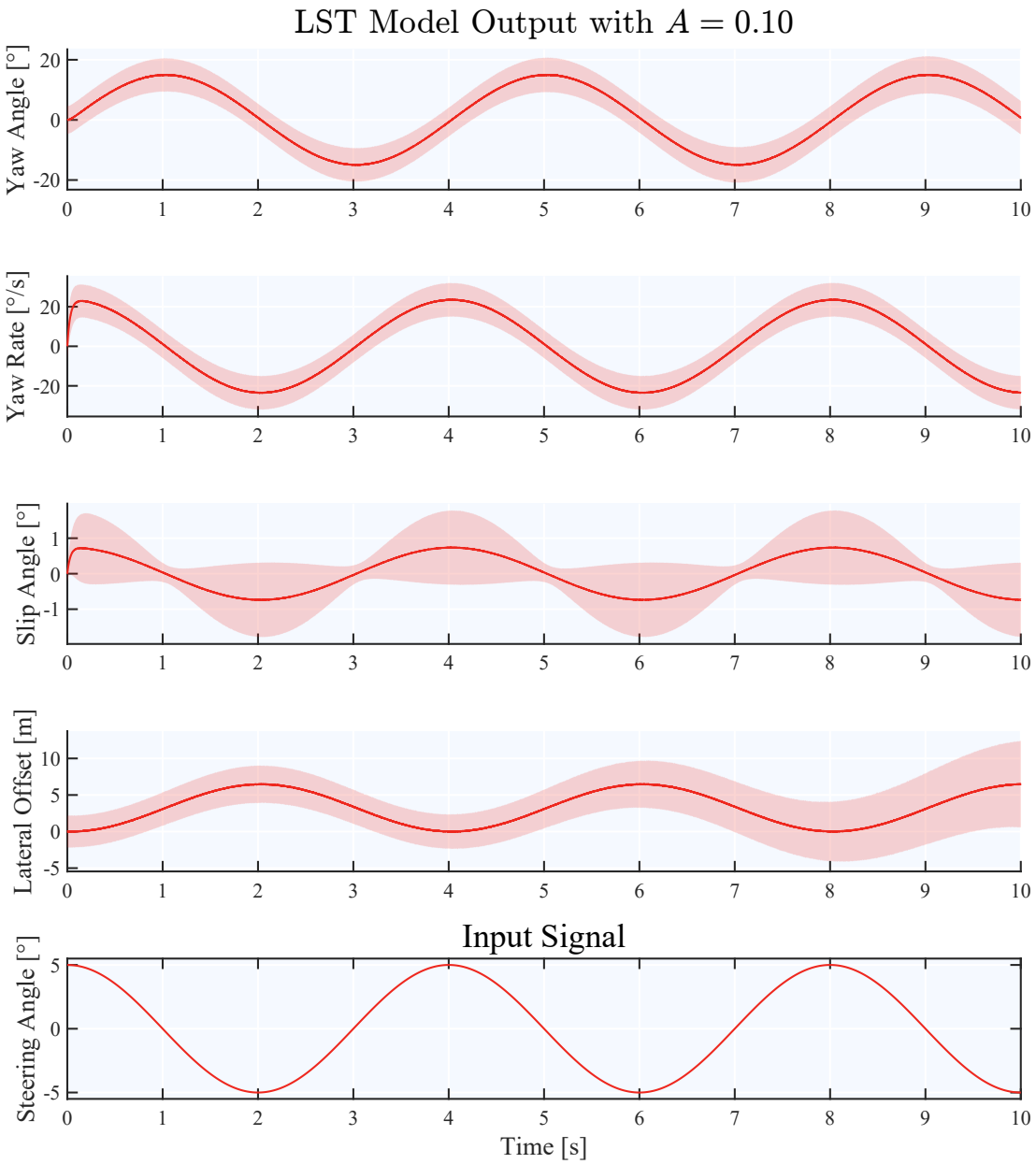

Figure A.11: Data From the LST model with $A = 0.10$.

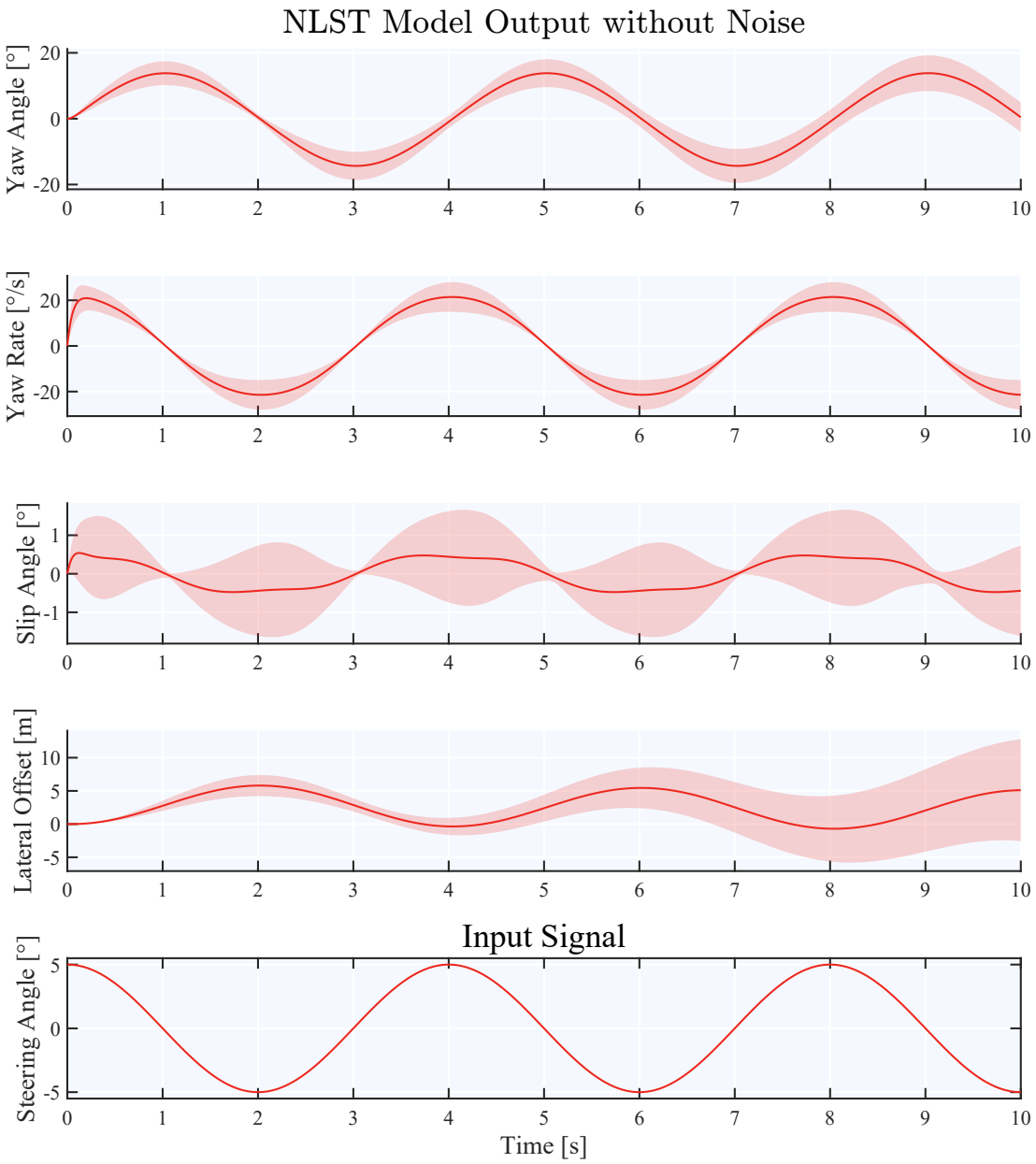

Figure A.12: Data From the NLST model with $A = 0$.

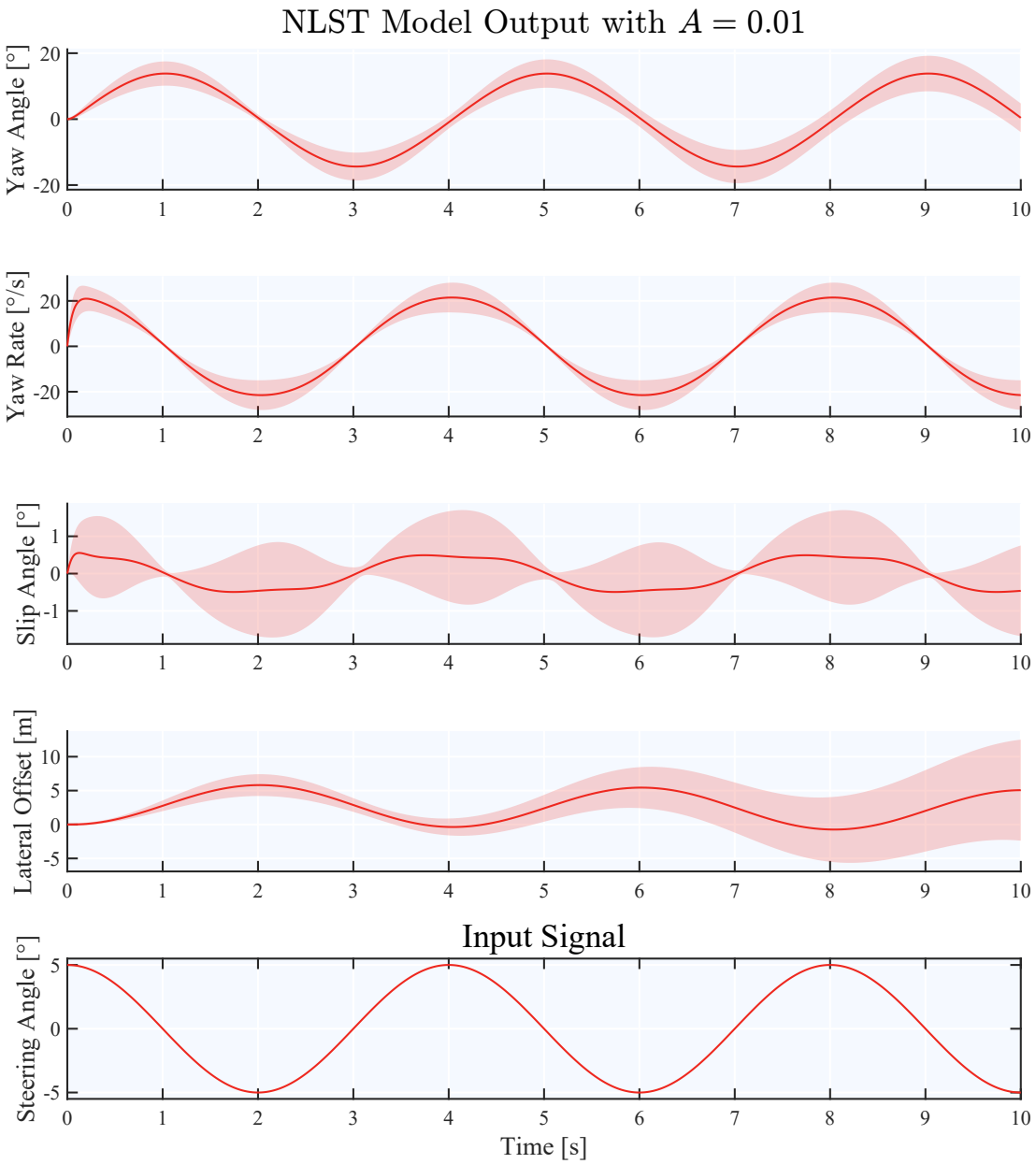

Figure A.13: Data From the NLST model with $A = 0.01$.

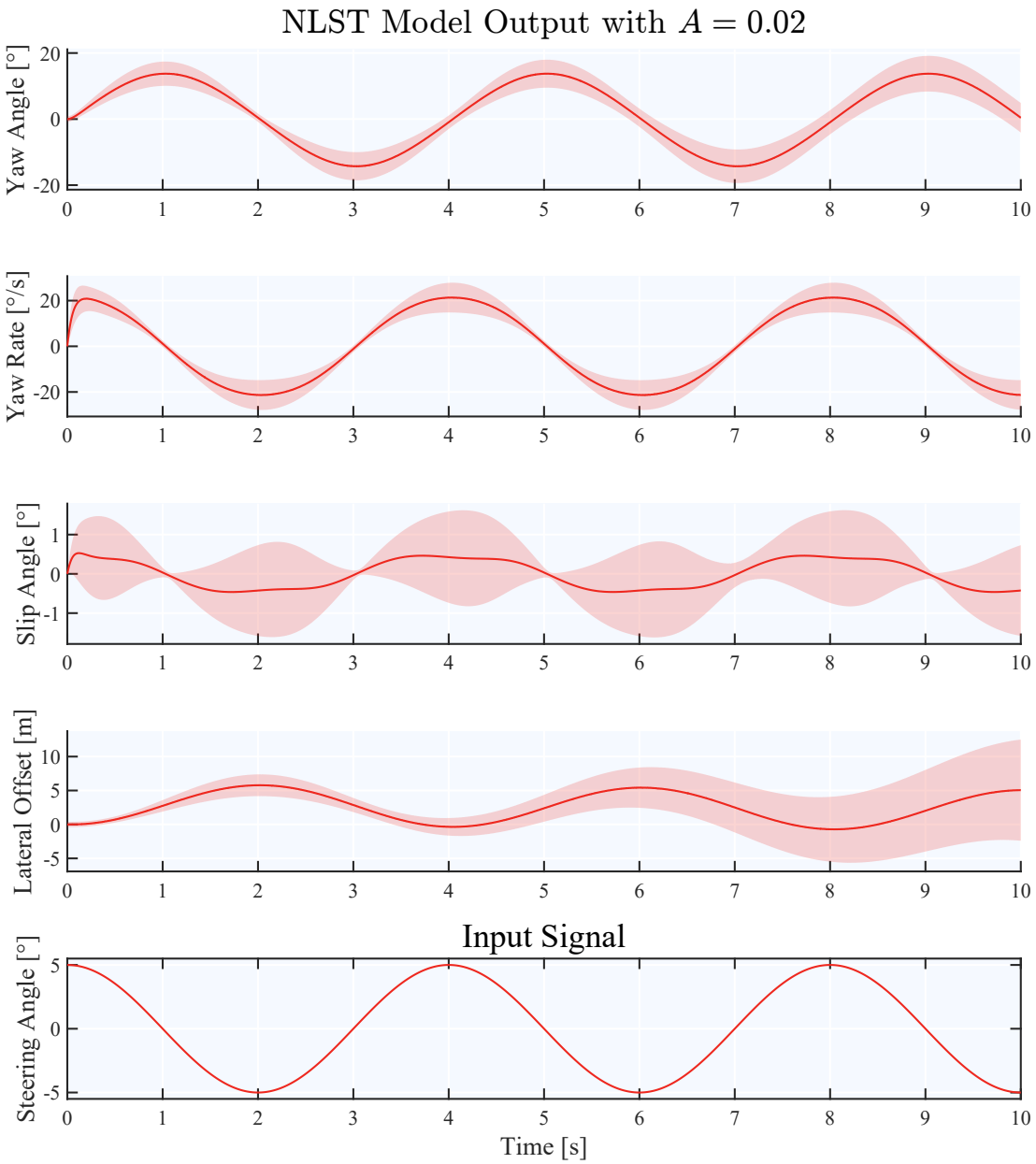

Figure A.14: Data From the NLST model with $A = 0.02$.

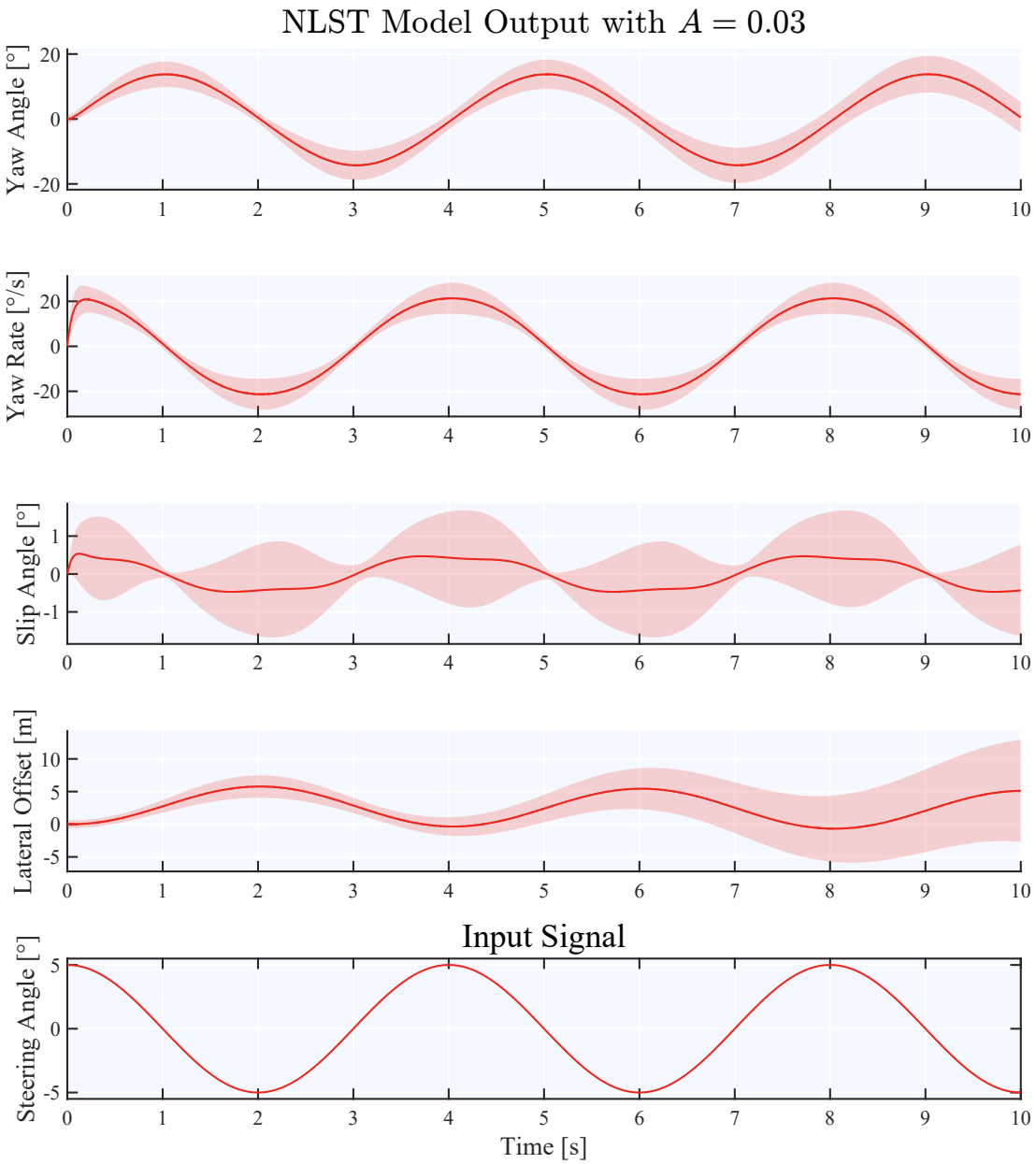

Figure A.15: Data From the NLST model with $A = 0.03$.

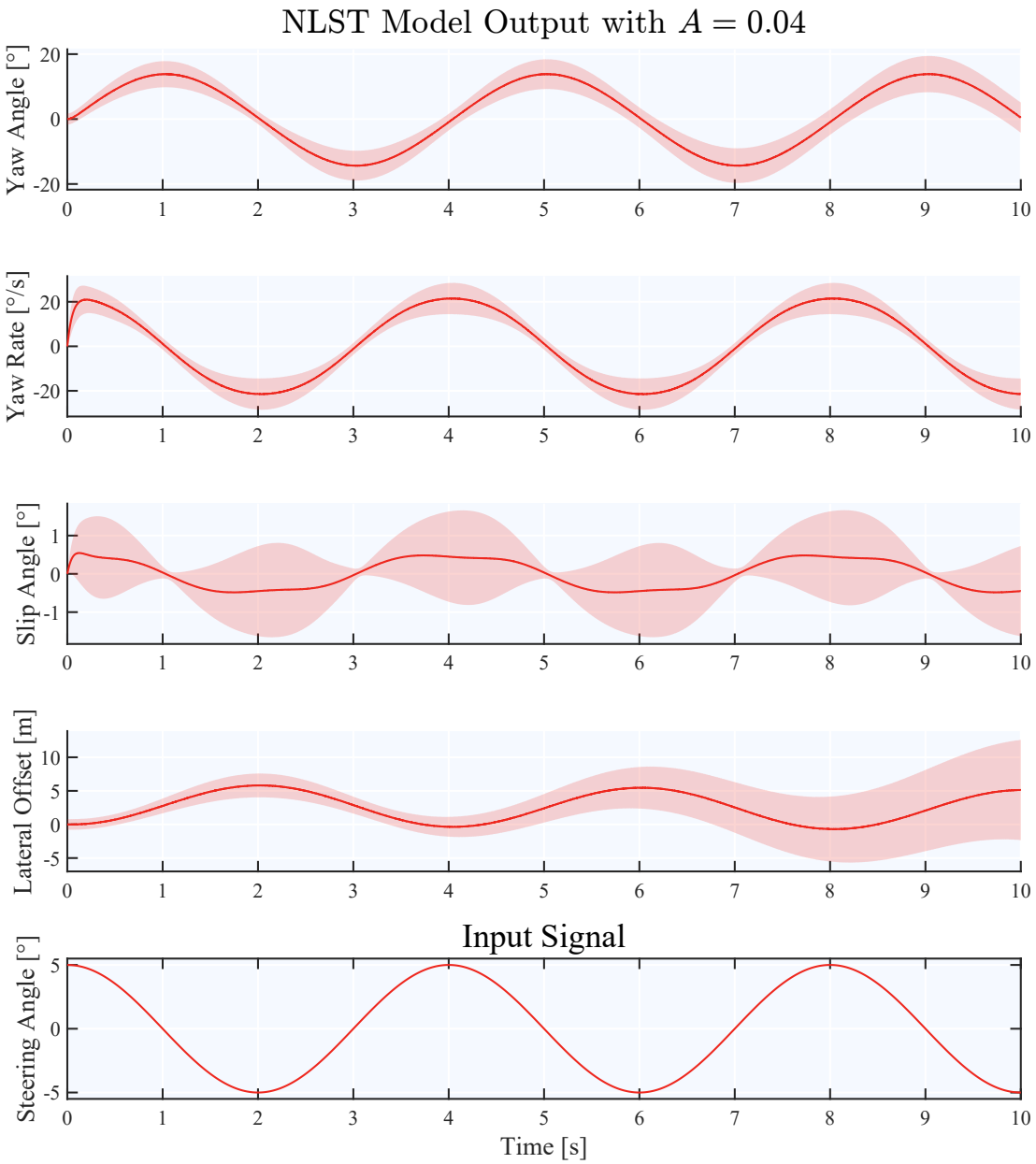

Figure A.16: Data From the NLST model with $A = 0.04$.

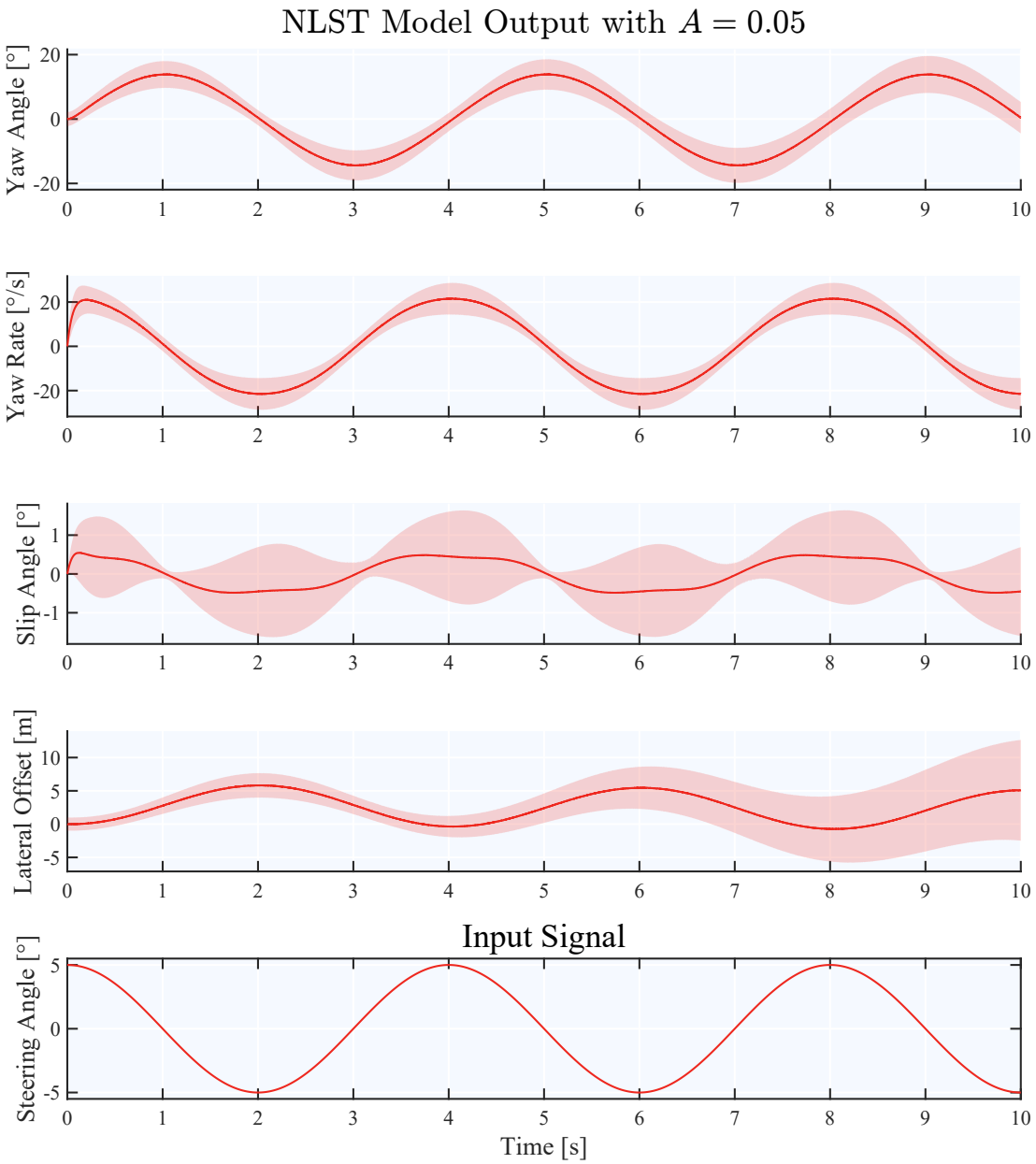

Figure A.17: Data From the NLST model with $A = 0.05$.

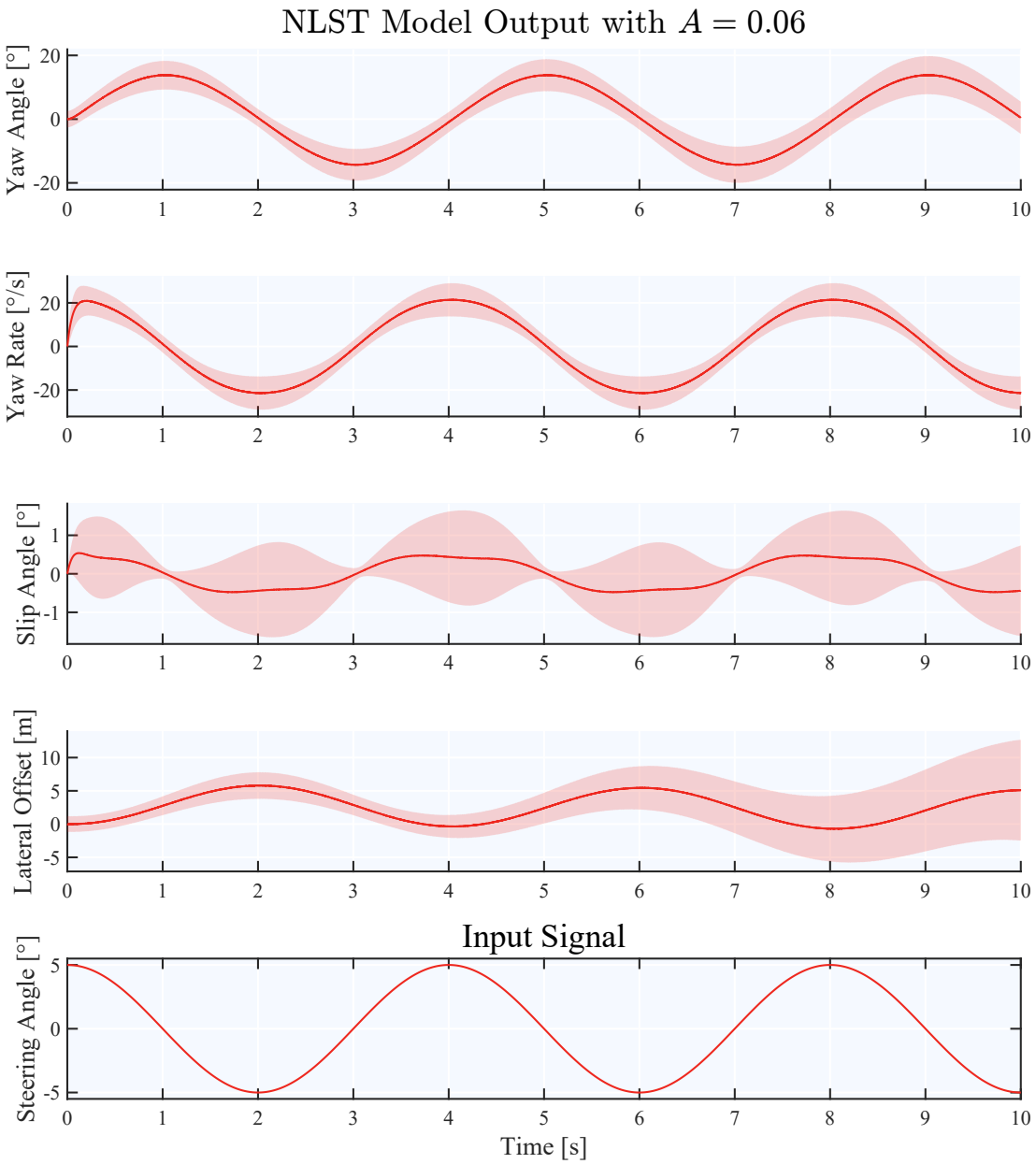

Figure A.18: Data From the NLST model with $A = 0.06$.

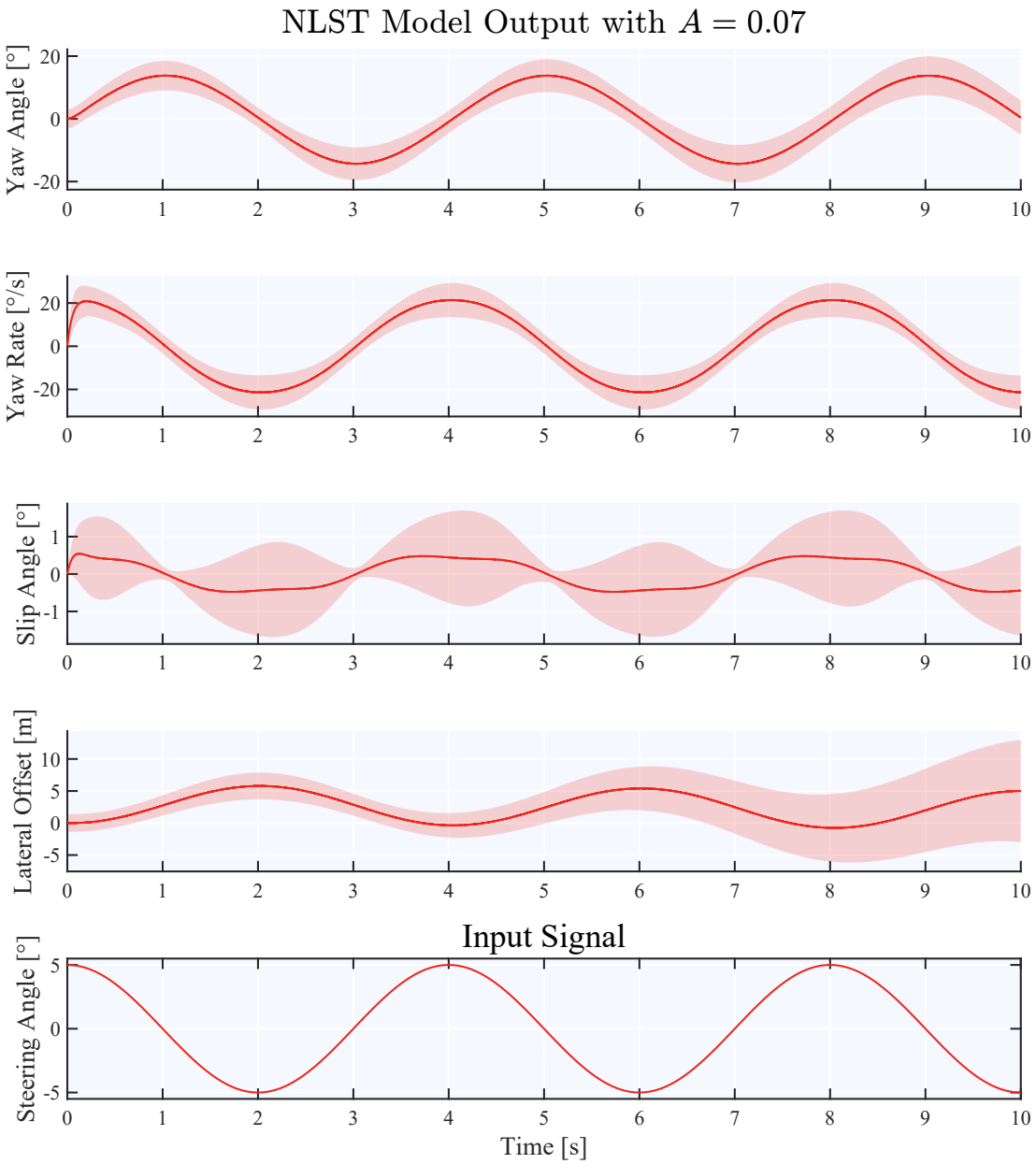

Figure A.19: Data From the NLST model with $A = 0.07$.

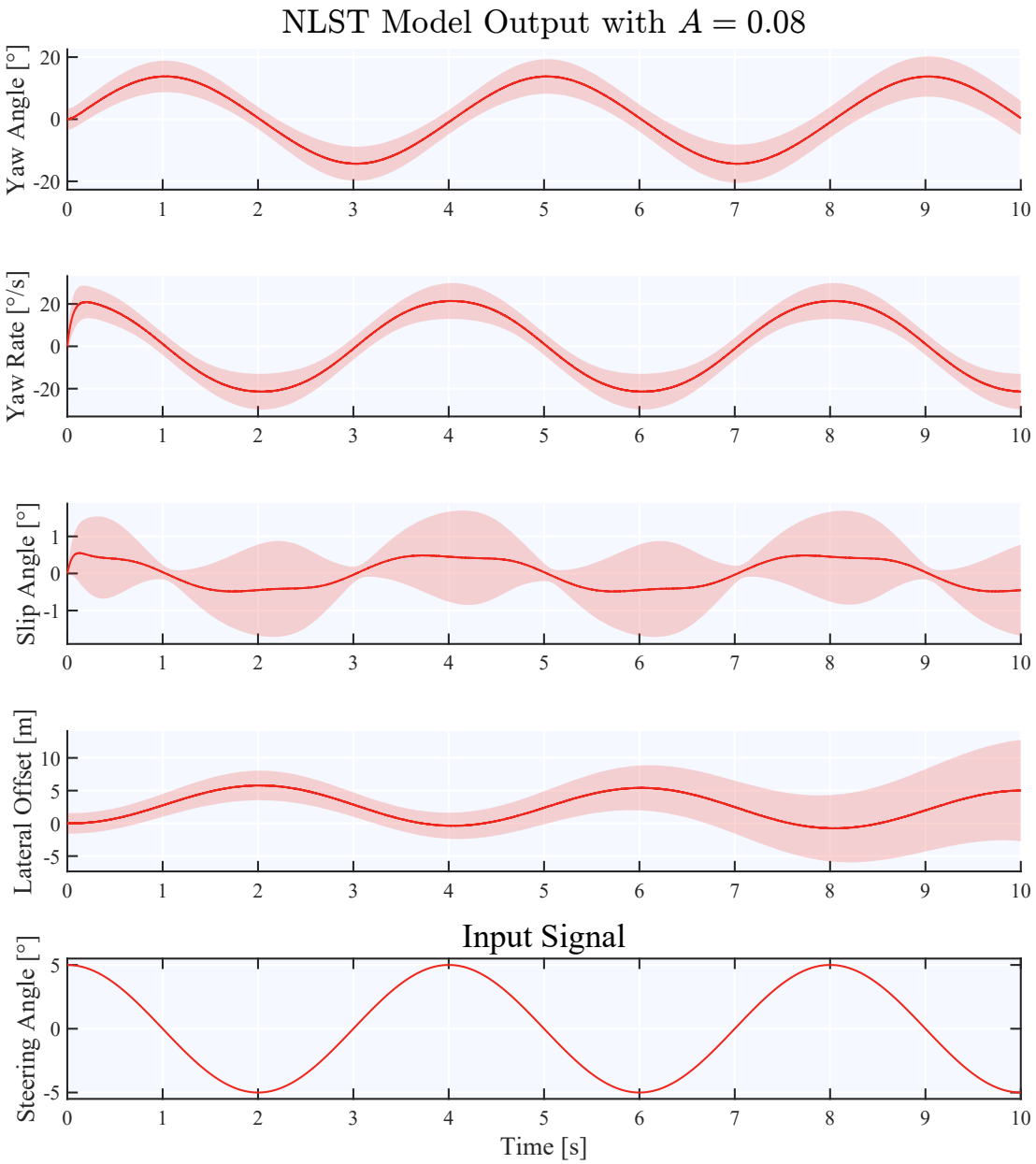

Figure A.20: Data From the NLST model with $A = 0.08$.

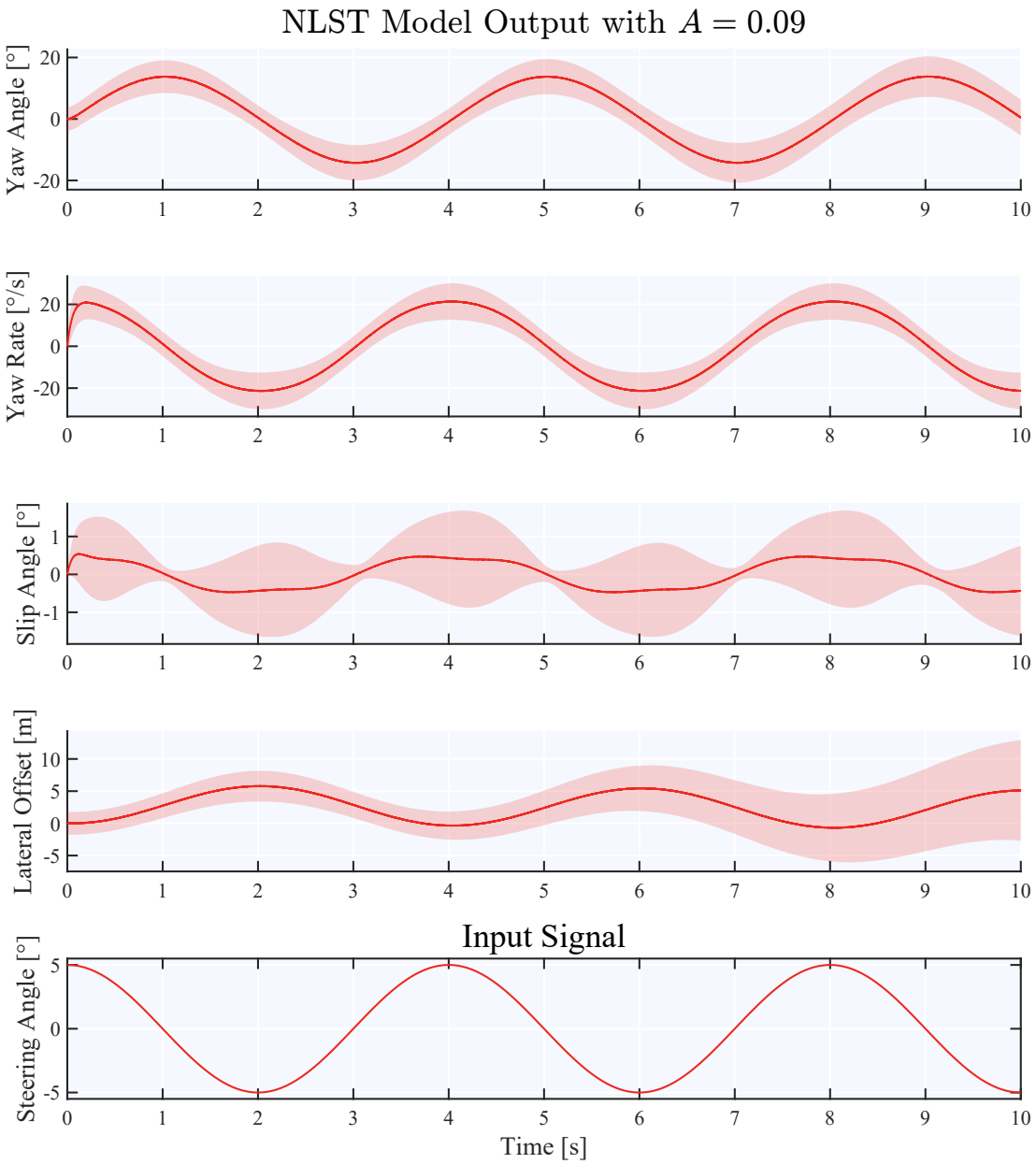

Figure A.21: Data From the NLST model with $A = 0.09$.

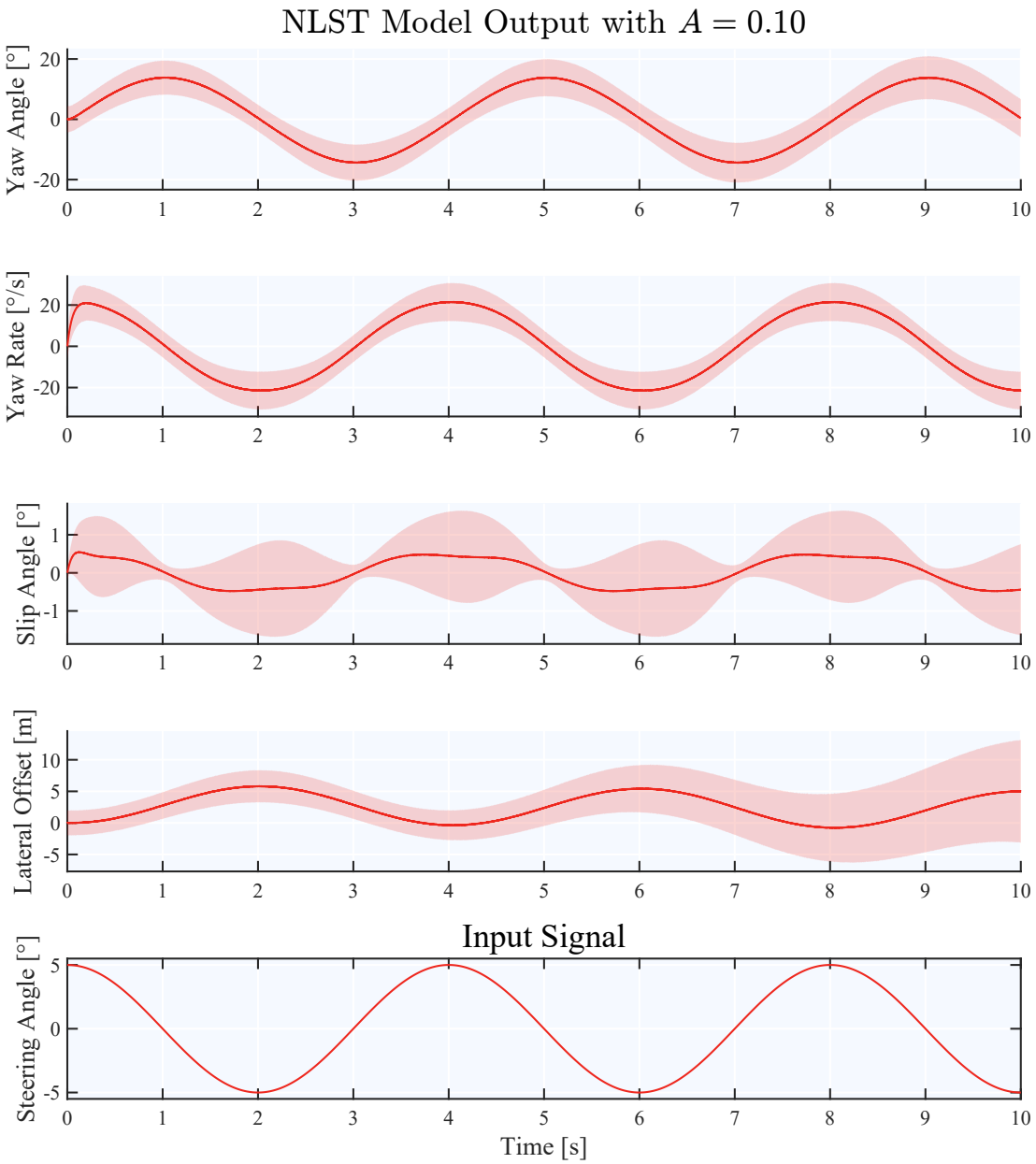

Figure A.22: Data From the NLST model with $A = 0.10$.

B

Estimated Distributions

Each figure in this appendix shows the identified distributions in the same plot as the corresponding real distribution to give a visual representation of how they differ. These visualisations are presented in this Appendix, unless already presented elsewhere, with the results form the first test in Section B.1, the estimates from the test with varied initial guesses presented in Section B.1.1, and lastly the identified distributions with varied noise intensities are presented in Section B.1.2.

B.1 Basic Identification Test

Figure B.1 shows the distributions identified using the LST model data. Figures B.2, B.3, and B.4 show the distributions estimated when using the NLST model data, where each figure shows the estimates produced using the STD, INP, or DST cost functions respectively.

B.1.1 Initial Guess Sensitivity

Figure B.5 shows the distributions identified using the LST model data with increasing deviation between the initial guess and actual value. Figures B.6, B.7, and B.8 show the distributions estimated when using the NLST model data, where each figure shows the estimates produced using the STD, INP, or DST cost functions respectively.

B.1.2 Noise Sensitivity

Figure 6.15 shows the distributions identified using the LST model data with increasing noise value. Figures B.9, B.10, and B.11 show the distributions estimated when using the NLST model data, where each figure shows the estimates produced using the STD, INP, or DST cost functions respectively.

B.1.3 Inverted Steering

Figure B.12 shows the estimated probability distributions using the INP cost function and Figure B.13 shows the estimates produced when using the DST cost function.

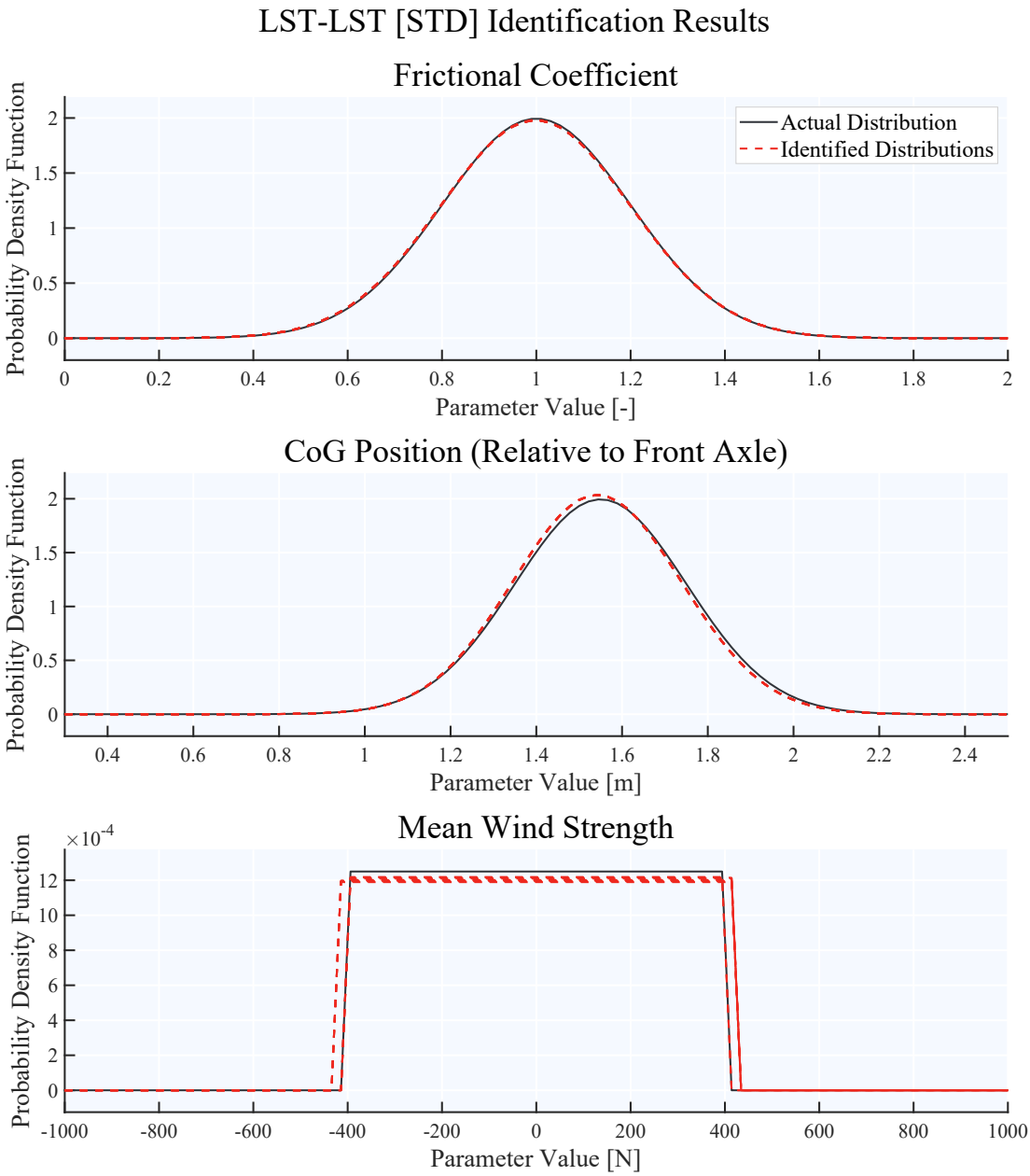

Figure B.1: Estimates produced based on the LST model data using the STD cost function.

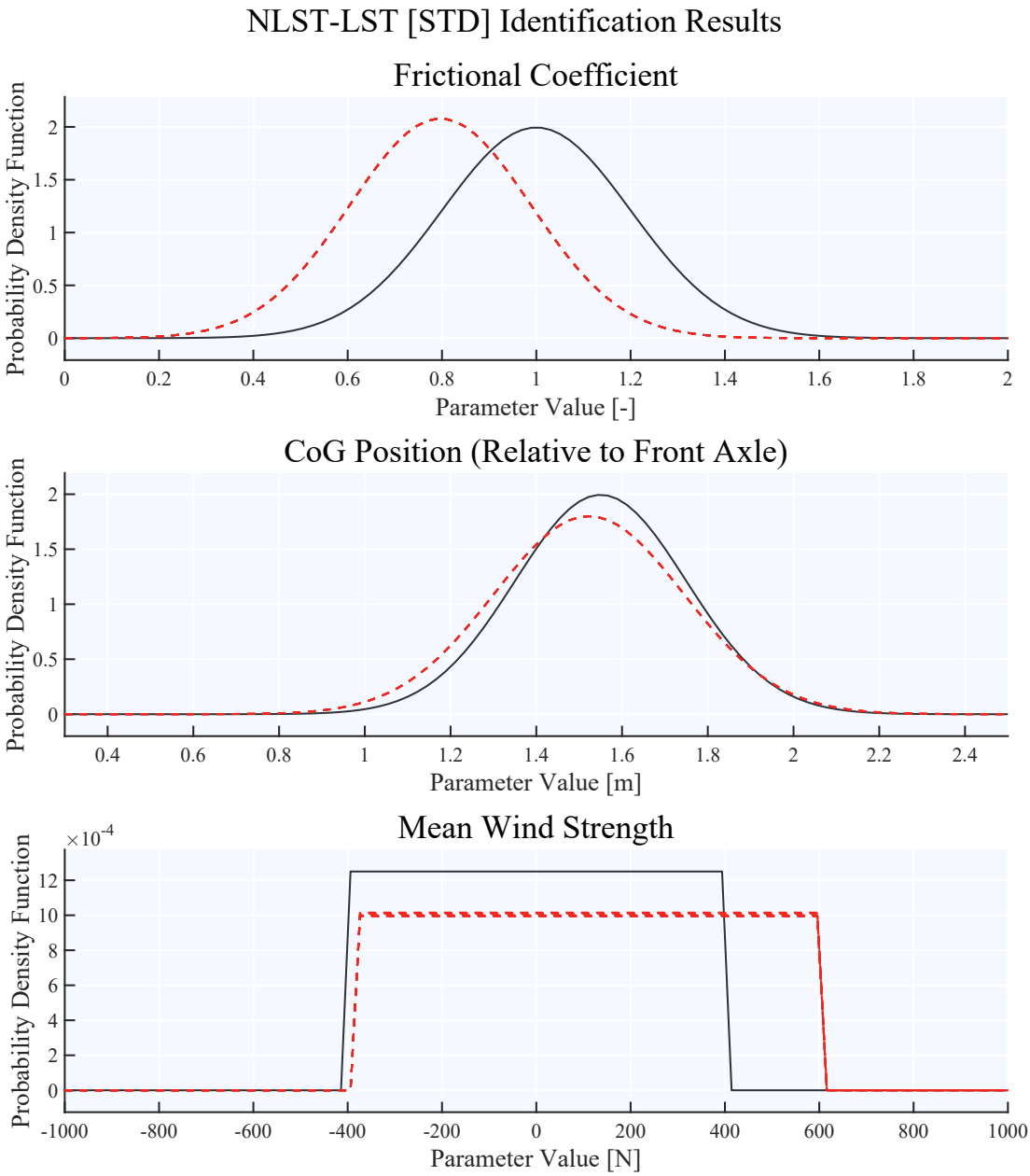

Figure B.2: Estimates produced based on the NLST model data using the STD cost function.

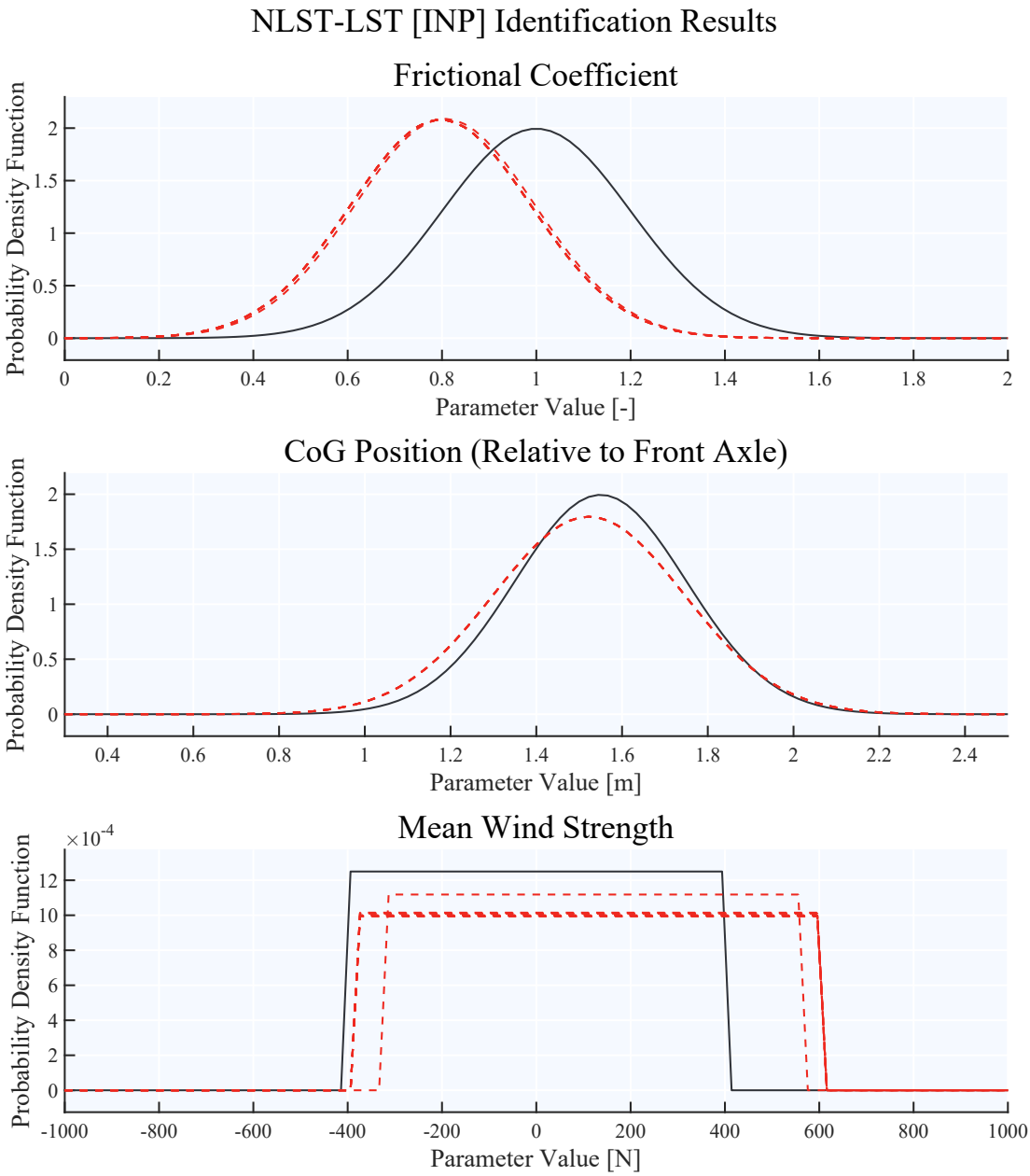

Figure B.3: Estimates produced based on the NLST model data using the INP cost function.

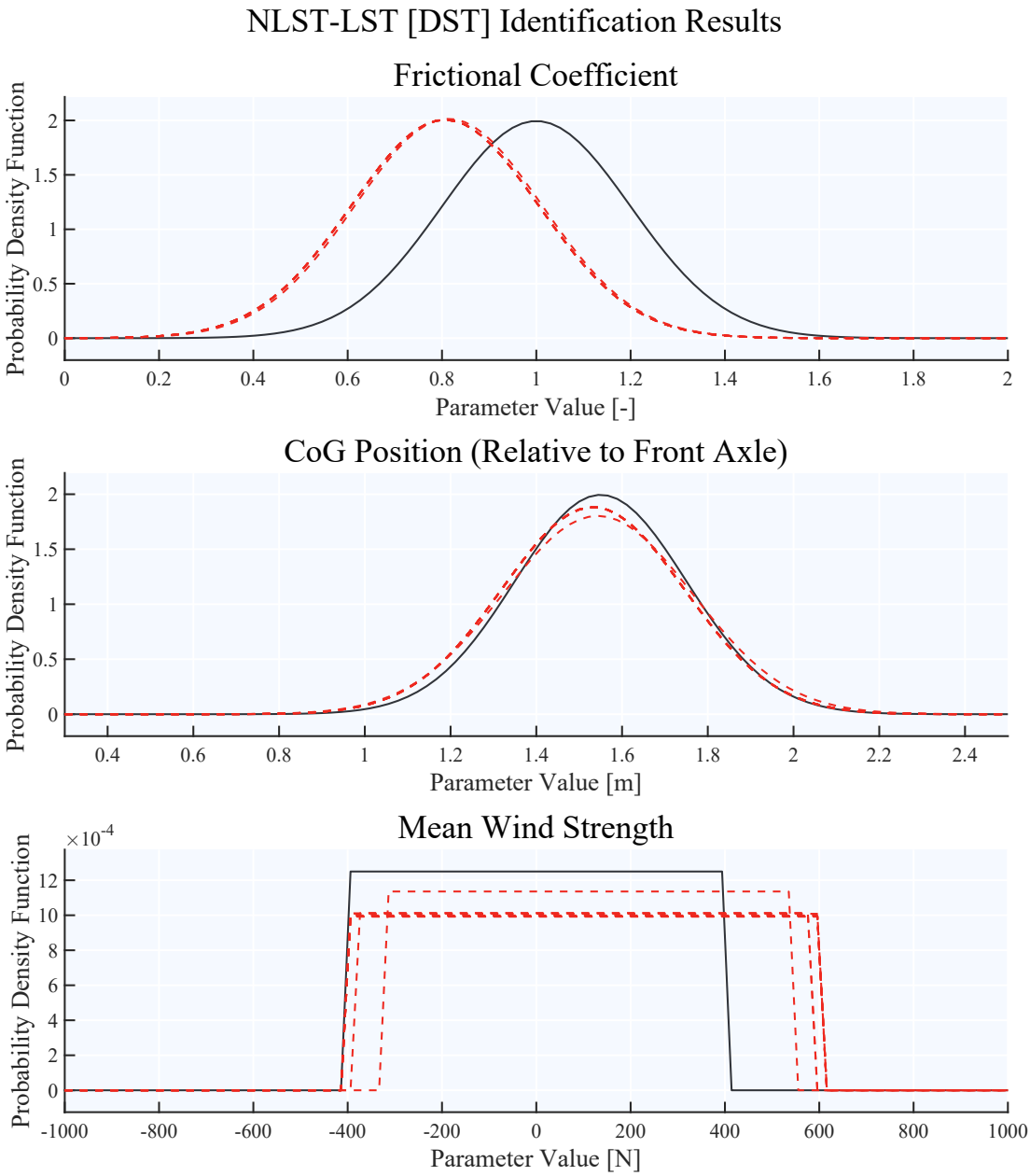

Figure B.4: Estimates produced based on the NLST model data using the DST cost function.

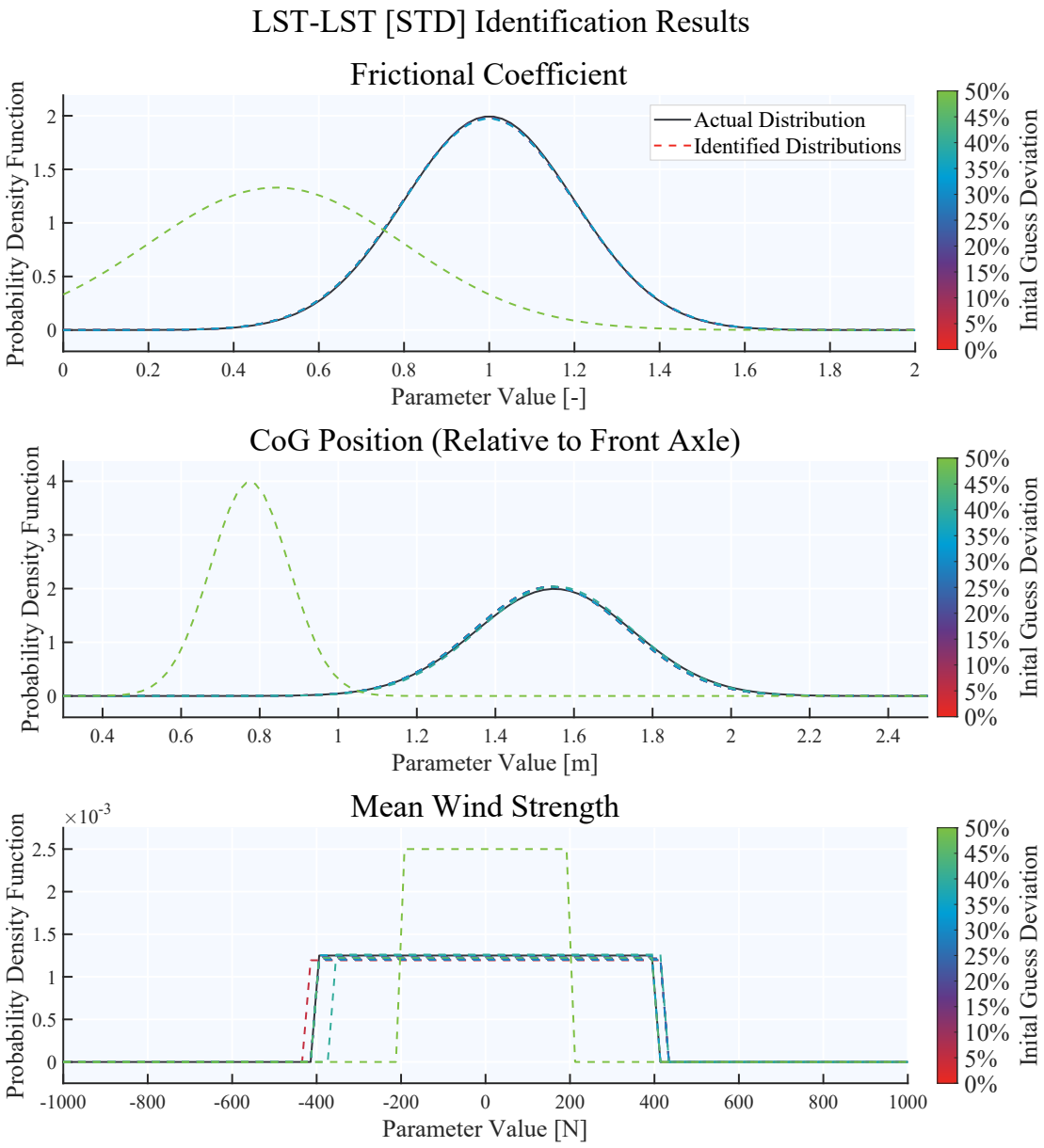

Figure B.5: Estimates produced based on the LST model data using the STD cost function.

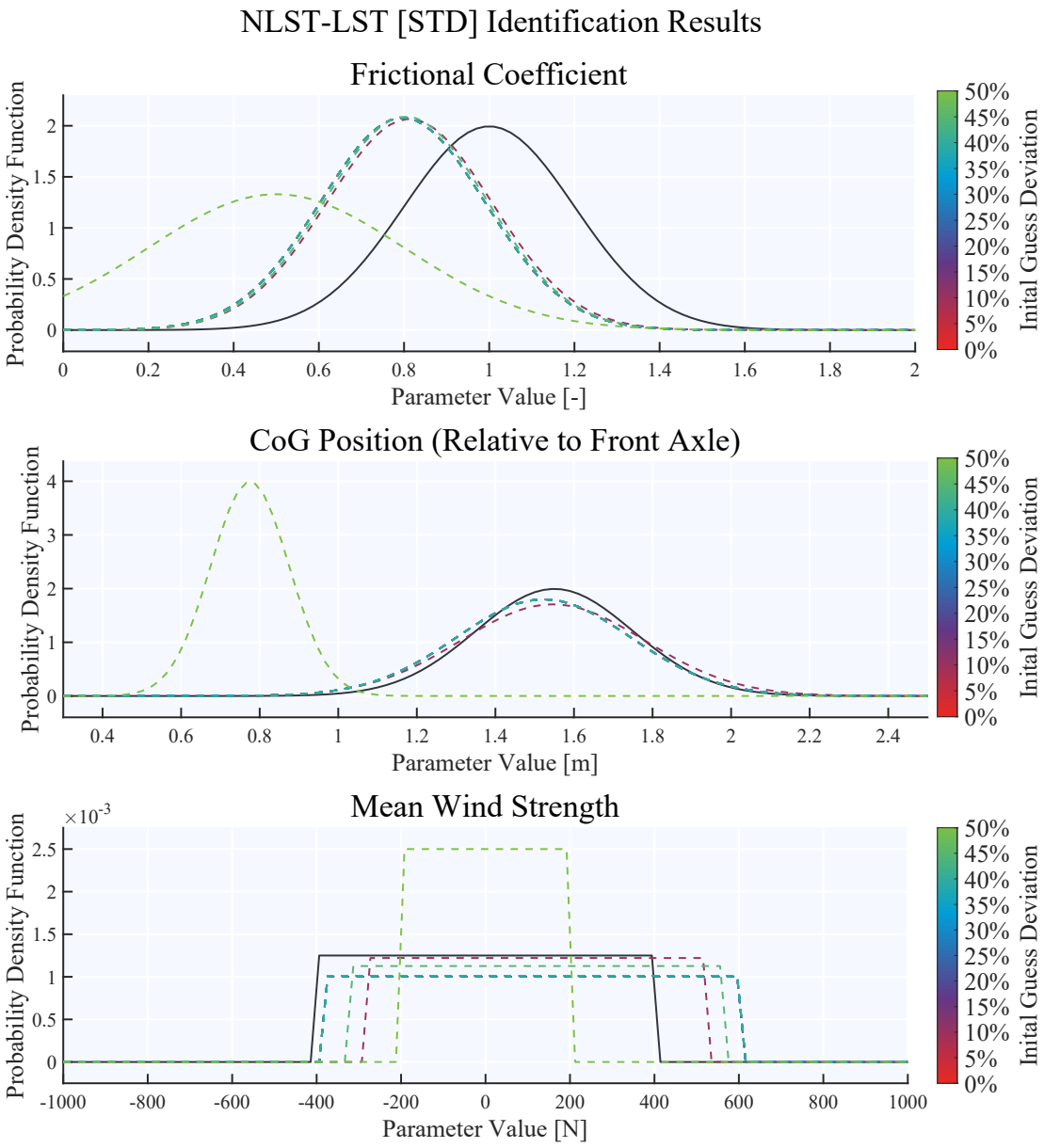

Figure B.6: Estimates produced based on the NLST model data using the STD cost function.

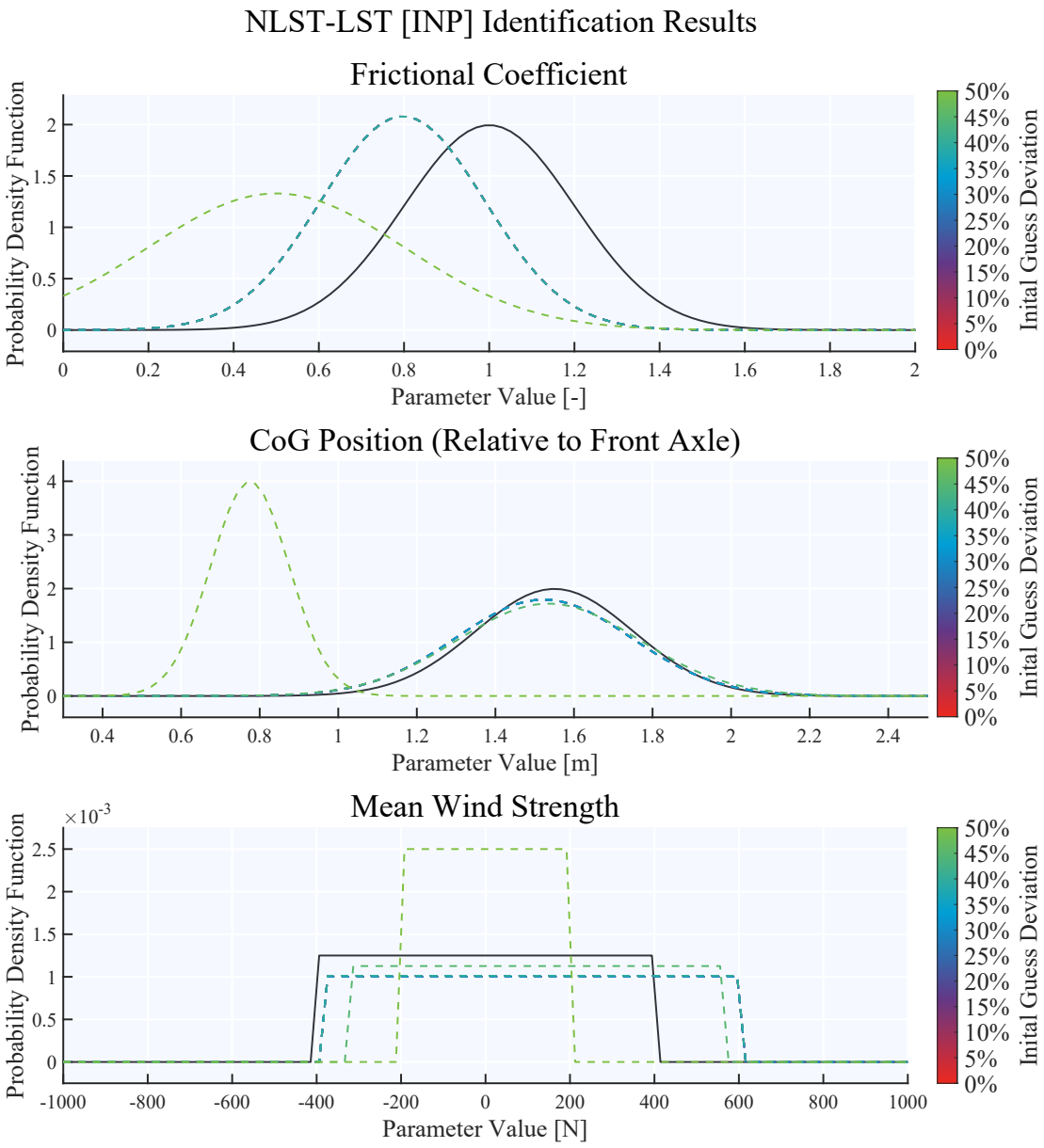

Figure B.7: Estimates produced based on the NLST model data using the INP cost function.

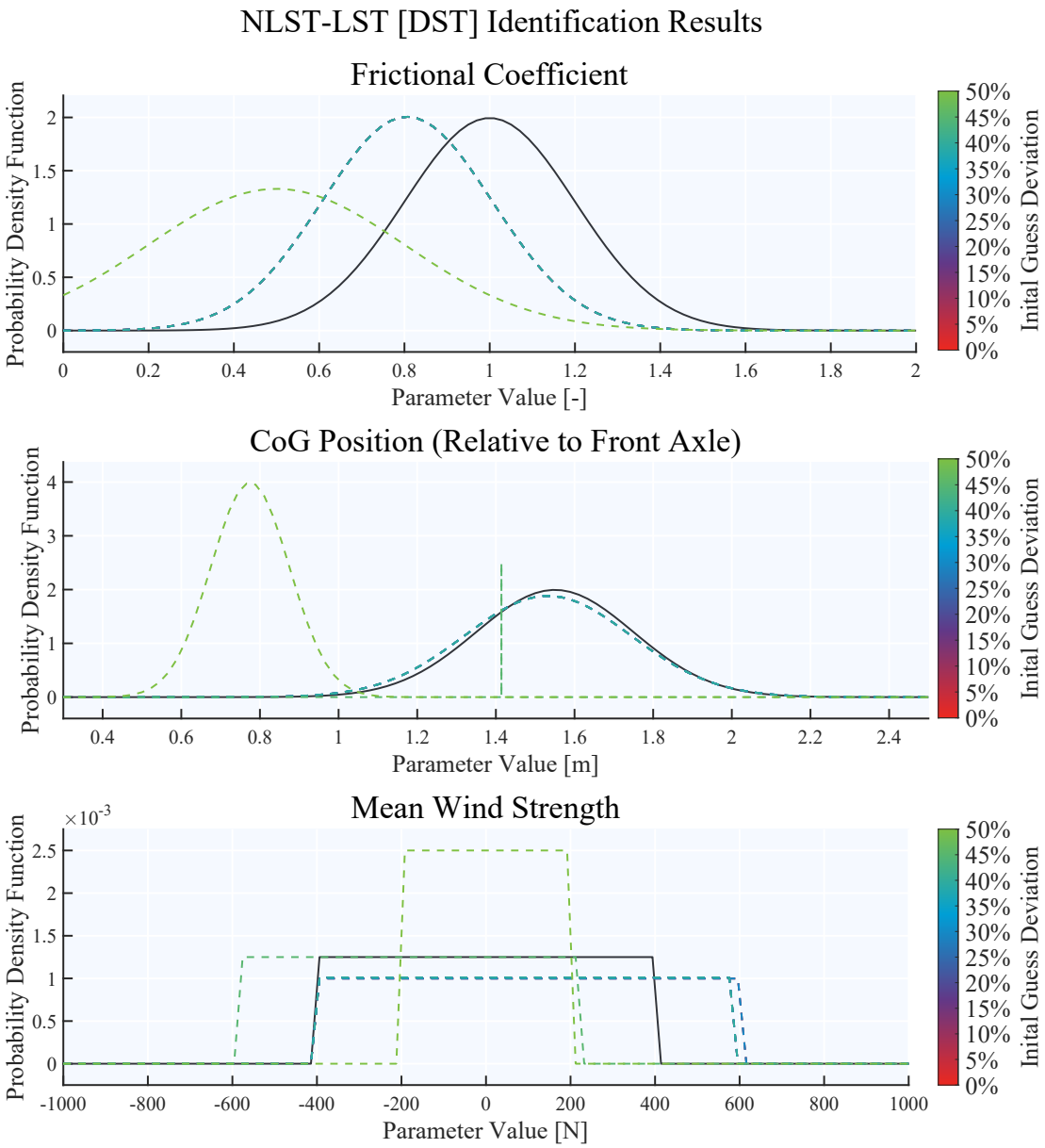

Figure B.8: Estimates produced based on the NLST model data using the DST cost function.

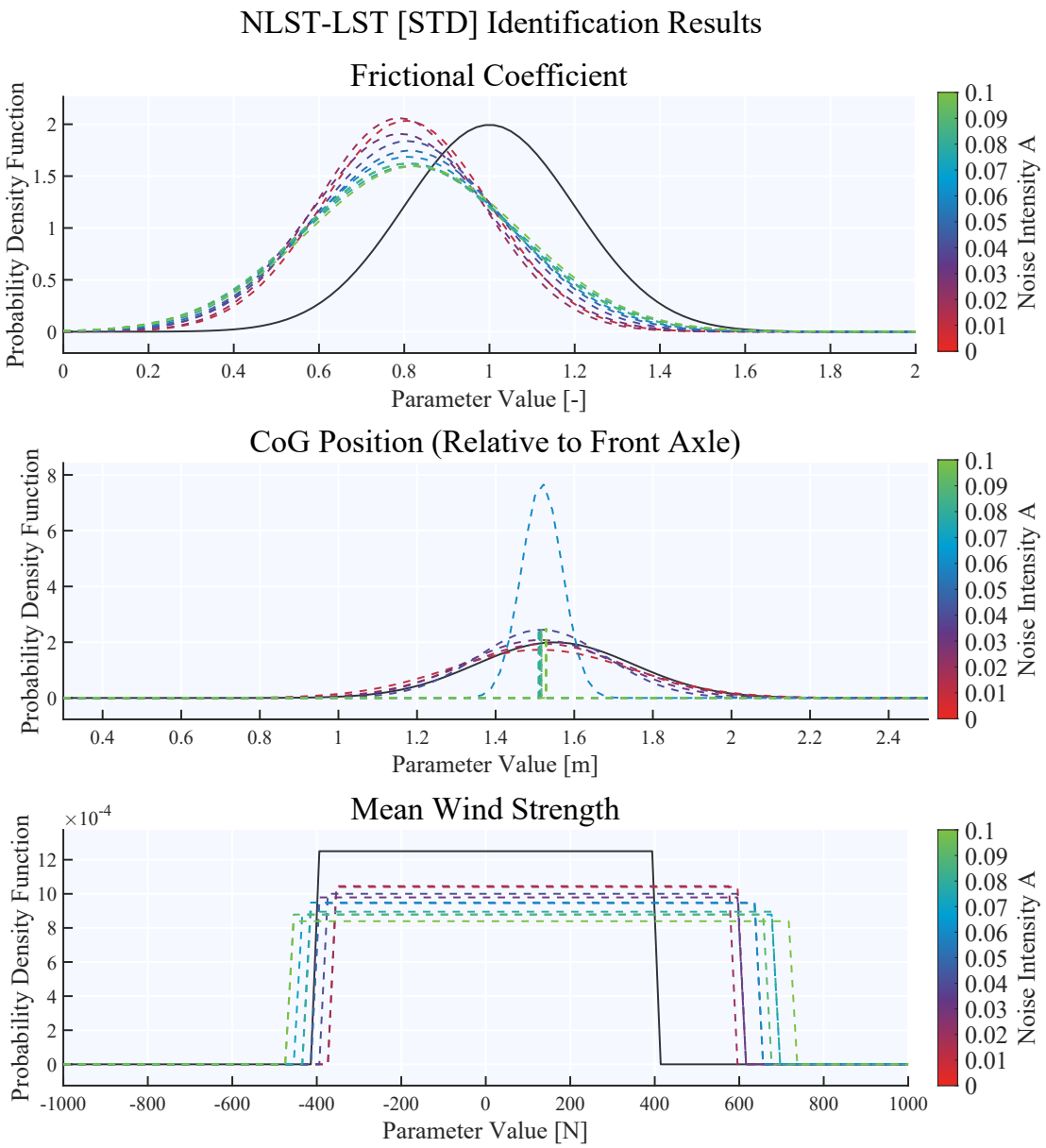

Figure B.9: Estimates produced based on the NLST model data using the STD cost function.

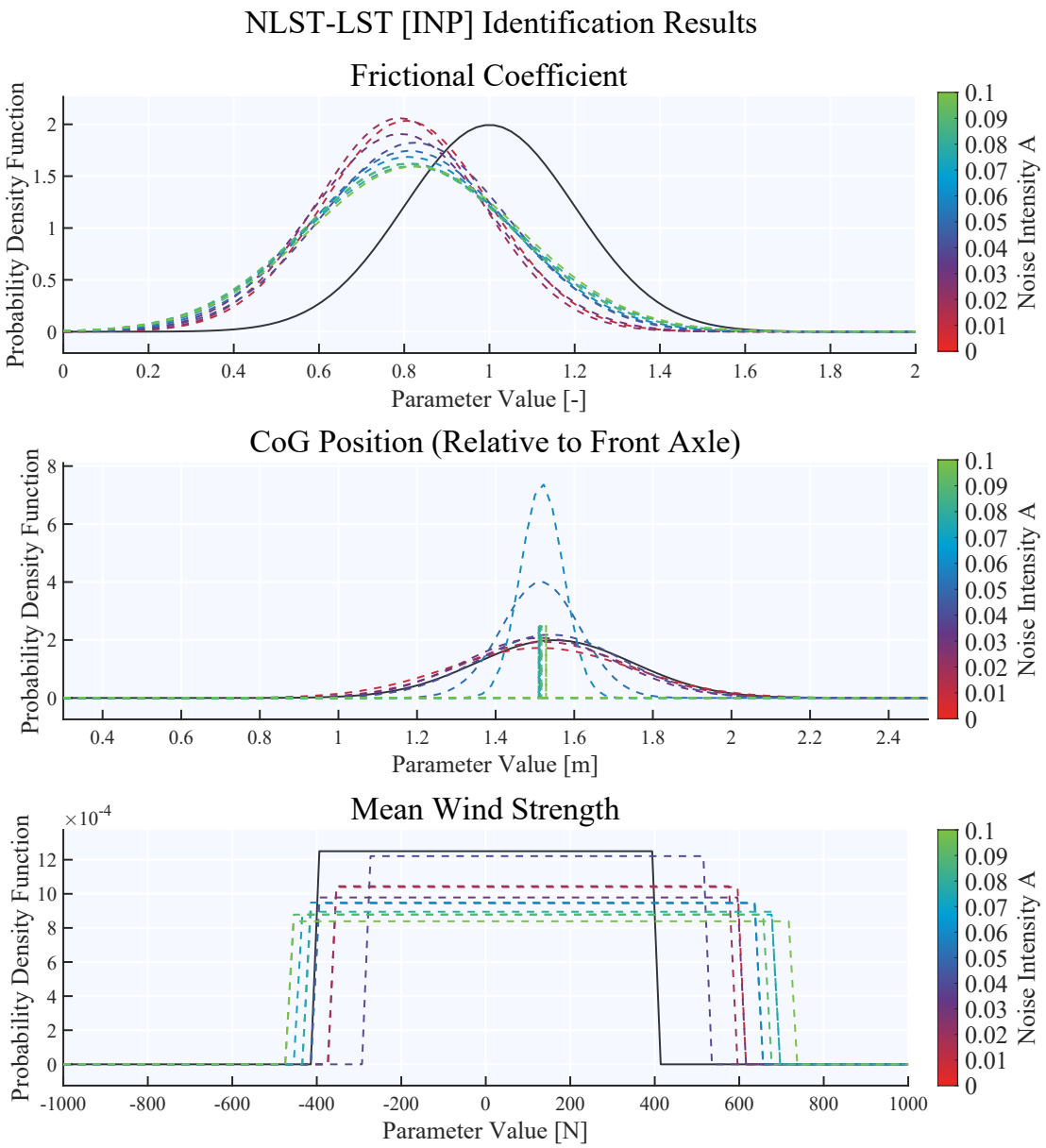

Figure B.10: Estimates produced based on the NLST model data using the INP cost function.

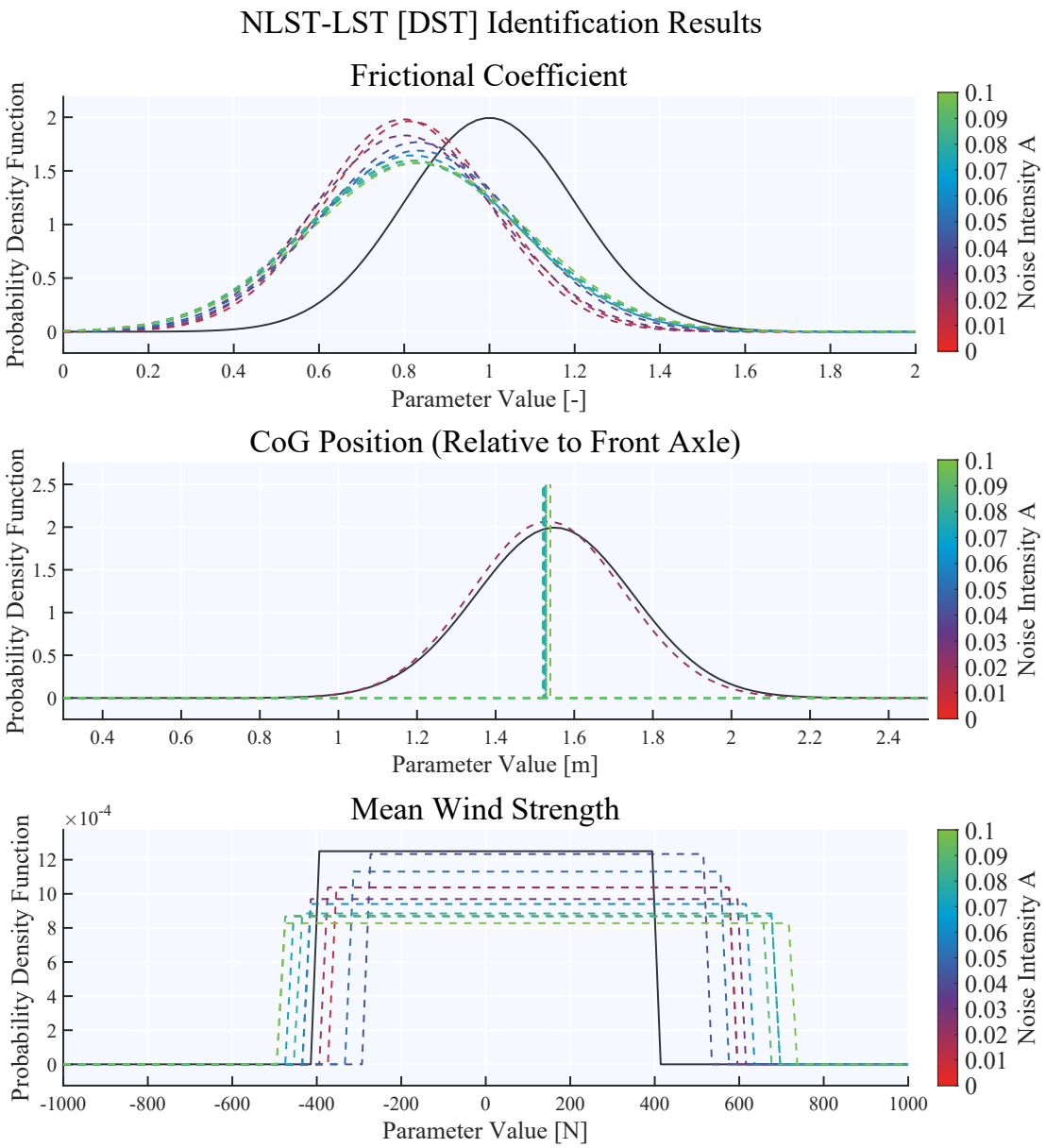

Figure B.11: Estimates produced based on the NLST model data using the DST cost function.

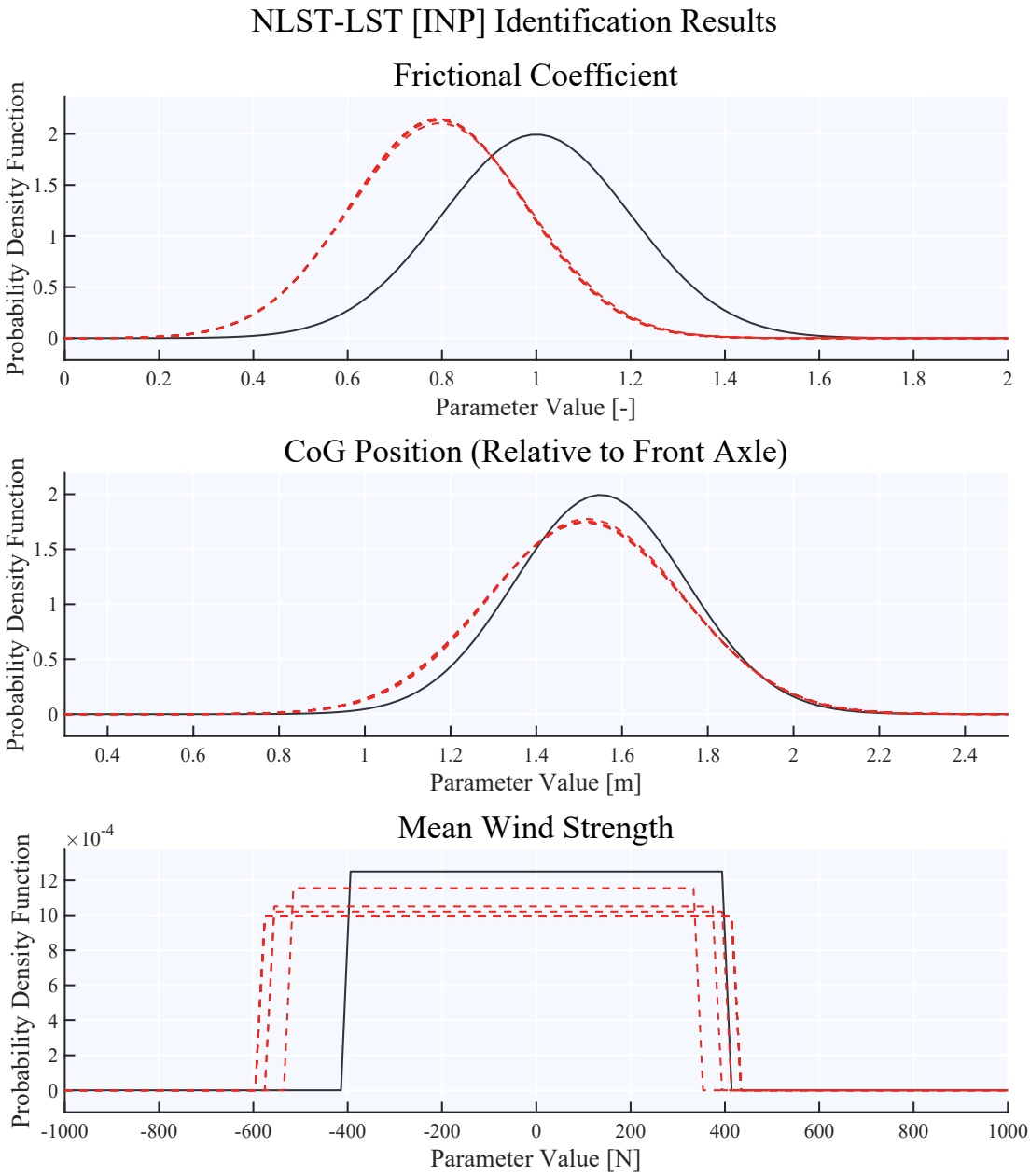

Figure B.12: Estimates produced based on the NLST model data using the INP cost function and inverted steering angle.

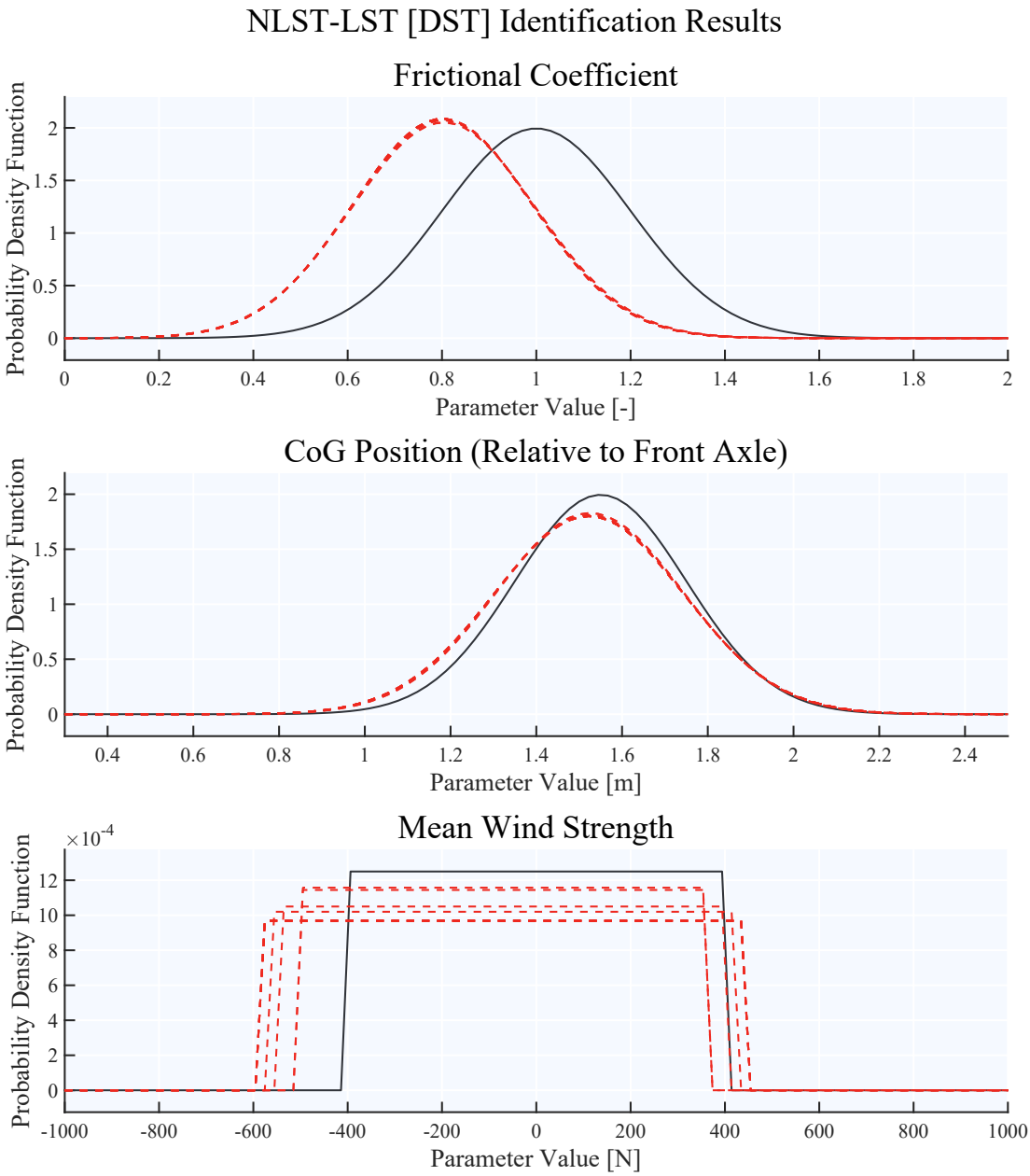

Figure B.13: Estimates produced based on the NLST model data using the DST cost function inverted steering angle.

DEPARTMENT OF ELECTRICAL ENGINEERING
CHALMERS UNIVERSITY OF TECHNOLOGY
Gothenburg, Sweden
www.chalmers.se

CHALMERS
UNIVERSITY OF TECHNOLOGY